NORTHWESTERN UNIVERSITY

A STUDY OF ION TRAPPING AND INSTABILITY IN THE FERMILAB ANTIPROTON ACCUMULATOR

A DISSERTATION

SUBMITTED TO THE GRADUATE SCHOOL
IN PARTIAL FULFILMENT OF THE REQUIREMENTS

for the degree

DOCTOR OF PHILOSOPHY

Field of Physics

By
Ping Zhou

December 1993

Abstract

In particle accelerators, electron-ion pairs are constantly created by beam particle collision with residual gas molecules. The beam may trap opposite charged ions. If uncorrected, trapped ions may cause beam instability and beam loss, and limit accelerator performance. The ion trapping problem especially related to the Fermilab antiproton accumulator, where the beam is unbunched and negatively charged, is studied here. The old clearing electrode system is found to be insufficient for complete ion clearing. The proposed upgrade to the clearing electrode system greatly improved the performance of the machine. Incomplete ion clearing is found to directly contribute to beam coherent oscillation and therefore beam coherent instability. A model has been developed which includes the effect of trapped ions in the normal beam coherent instability treatment with conventional machine impedance. It is found that the effect of trapped ions on the beam coherent instability can be described as a form of impedance. Together with physical arguments, it can be used to explain some of the behavior of the beam coherent instability observed in the accumulator. An Ion Detector and Energy Analyzer system was developed which provides the ability to directly monitor the ions coming out of the beam and measure their energy spectrum. Ions are observed to interact with explosive coherent oscillations that lead to emittance blowups. The ion energy distribution extends to much higher energy than expected. The flux of ions escaping with cool, stable beam is also higher than previously thought. The main subject of the study is related only to ion trapping in a DC beam, although a few issues are illustrated with a case study on the Tevatron with separated orbits of proton and antiproton beams.

Contents

List of Tables

List of Figures

Chapter 1

Introduction

1.1 Fermilab Accelerator Complex

The Fermilab accelerator complex[1], see Fig. 1.1 consists of a series of accelerators which can accelerate either proton and/or antiproton beams to a maximum energy of $900GeV$. At the beginning of the accelerator chain there is a linear accelerator which accelerates H^- beam to $200MeV$. A fast-cycling synchrotron called the Booster then strips the electrons which turns the beam into a proton beam for further acceleration to $8GeV$. The Main Ring, a synchrotron, receives the beam extracted from the booster and can accelerate it to $150GeV$. The beam from the Main Ring can be either injected into the highest energy synchrotron, the Tevatron, for the final acceleration, or used for antiproton production. The antiprotons are stacked and stored in the Antiproton Source at $8GeV$. When needed, antiprotons are injected back into the Main Ring and then into the Tevatron collider. Counter rotating beams of protons and antiprotons, each with a maximum energy of 900GeV, can then be made to collide in several interaction regions.

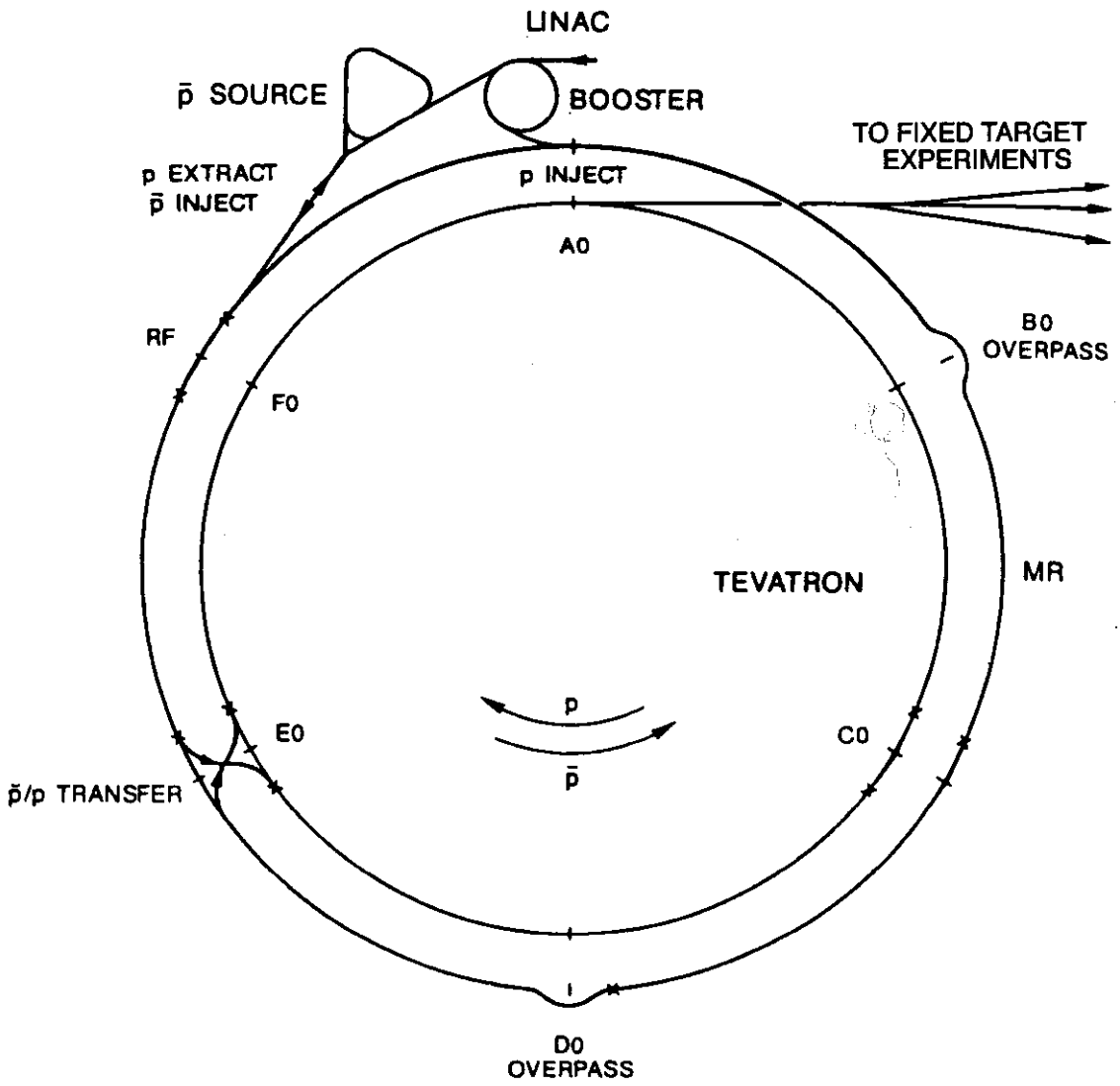

Figure 1.1: Fermilab accelerator complex. This figure is roughly to scale but takes some artistic liberty. The Main Ring (MR) is actually on top of the Tevatron ring.

1.2 Brief Introduction to Accelerators

The purpose of this section is to introduce the basics of accelerators and the terminology necessary for the rest of the thesis. Further details can be found in [2].

1.2.1 The Basics

Particle accelerators in general refer to machines that can store and/or accelerate charged particles. Machines in which the particle beams remain a long period of time, hours to days, are called storage rings. There are many kinds of accelerators. Here we will only talk about synchrotrons where the particle beam circulates in the beam pipe under vacuum. The beam is kept on a fixed orbit by dipole bending magnets and is transversely focused by quadrupole magnets. In modern accelerators the alternating gradient (AG) approach is used for transverse focusing. The arrangement of the magnets is called the lattice of the machine. The beam energy is changed through the application of a synchronized RF voltage and the synchronized change of guiding field, thus the name synchrotron.

1.2.2 Longitudinal Motion

Here longitudinal refers to the direction along the beam orbit. Beam particles inevitably have some spread in their longitudinal momentum. Particles with different momentum travel in slightly different orbits and speeds. For particles with a momentum difference Δp, the orbit length difference is described by

$$\frac{dL}{L} = \frac{1}{\gamma_t^2}\frac{\Delta p}{p} \tag{1.1}$$

where γ_t is a constant determined by the machine lattice. The corresponding difference in their speeds is

$$\frac{dv}{v} = \frac{1}{\gamma^2}\frac{\Delta p}{p} \tag{1.2}$$

The resulting difference in their revolution frequency is

$$\frac{df}{f} = \frac{dv}{v} - \frac{dL}{L} = -\eta\frac{dp}{p} \tag{1.3}$$

where

$$\eta = \frac{1}{\gamma_t^2} - \frac{1}{\gamma^2} \tag{1.4}$$

is called the "slip factor". Because of this frequency deviation, the RF phase of off momentum particles, i.e. the RF phase when they pass RF cavities, will slip a little every turn, thus the name "slip factor". Notice that at $\gamma = \gamma_t$ the slip factor changes sign. The beam energy at which this occurs is called the transition energy. Normally an off momentum particle oscillates around a stable RF phase and all particles form bunches. The stable RF phase, however, is different below and above this transition energy, so the RF phase has to be changed when the beam crosses the transition.

1.2.3 Transverse dynamics

Particles whose position differ from the ideal closed orbit undergo transverse oscillations which are known as betatron oscillations. The coordinate system used is illustrated in Fig. 1.2. The longitudinal coordinate s is defined along the design orbit

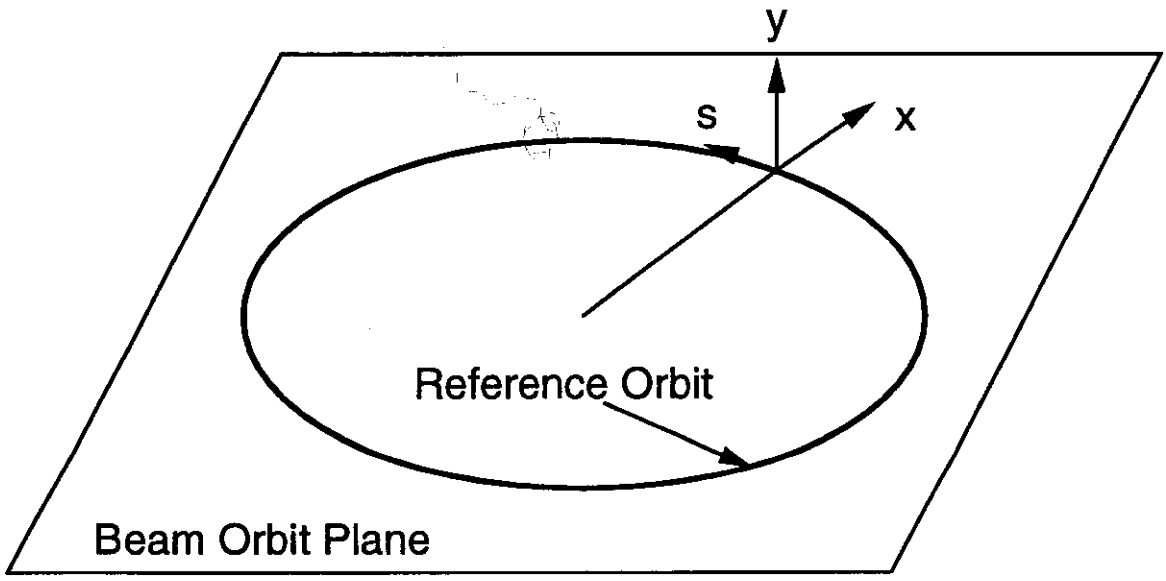

Figure 1.2: Local coordinate system

and it is used as the independent variable. The equation of transverse motion in the

local coordinate system is the following

$$x'' + [K(s) + \frac{1}{\rho^2}]x = 0 \quad (1.5)$$

$$y'' - K(s)y = 0 \quad (1.6)$$

where $x' = \frac{dx}{ds}$ and $K(s)$ is piecewise constant in an AG machine. $K = 0$ in drift sections and dipole magnetic fields. ρ is the local radius of curvature. It is zero except in dipole magnets. A horizontally focusing quadrupole magnet is necessarily defocusing in the vertical direction. This leads to the difference in the sign of $K(s)$ in their corresponding equations.

$K(s)$ is a periodic function in s and the period is at most the machine circumference, so equations 1.5 and 1.6 are a form of Hill's equation. The solution of them can be written as

$$x, y = A_{x,y}\sqrt{\beta_{x,y}(s)}\cos[\psi_{x,y}(s) + \phi_0] \quad (1.7)$$

where $\beta_{x,y}$ are called beta functions. Together with two other derived quantities, i.e.

$$\alpha \equiv -\frac{1}{2}\frac{d\beta}{ds} \quad (1.8)$$

$$\gamma \equiv \frac{1+\alpha^2}{\beta} \quad (1.9)$$

these are called Twiss parameters.

$$\psi_{x,y}(s) = \int_0^s \frac{ds}{\beta_{x,y}(s)} \quad (1.10)$$

is the betatron phase. The total betatron phase advance in one turn divided by 2π is called the tune,

$$Q_{x,y} = \frac{1}{2\pi}\int_0^{2\pi R} \frac{ds}{\beta_{x,y}(s)} \quad (1.11)$$

It can be shown that $A_{x,y}$ is an invariant of the motion and it is related to the phase space area enclosed by the particle orbit by

$$\pi A_{x,y}^2 = \textit{phase space area in } x, y \quad (1.12)$$

The largest phase space area that a machine can accommodate is called the acceptance and the total phase space area of a beam is called its emittance. Since a beam usually

has a halo, the total phase space area is hard to define and usually an rms emittance or the emittance for certain percentage of the beam is used. Unspecified emittance will be for 95% of the beam from now on in this work.

The difference in longitudinal momentum will affect the transverse displacement of a beam particle because of the dipole magnetic field. Usually this field is in the vertical plane and it introduces horizontal dispersion D,

$$\Delta x = D(s) \times \frac{\Delta p}{p} \tag{1.13}$$

Since the magnetic focusing strength depends on the particle's momentum, momentum deviation also affects the particle's vertical and horizontal tune,

$$\Delta Q_{x,y} = \xi_{x,y} \frac{\Delta p}{p} \tag{1.14}$$

ξ is called the chromaticity of the machine. The natural chromaticity can be altered using sextupole magnets.

1.2.4 Nonlinear Resonances

Magnets in real machines have imperfections which will cause field errors expressed as higher-order multipole field components. These imperfections do not just perturb the normal beam motion, they may also drive non-linear betatron resonances. Particles on resonance will experience an increase in their betatron oscillation amplitudes and to the point where beam loss may occur. The general resonance condition can be written as[2]

$$mQ_x + nQ_y = p \tag{1.15}$$

where m, n and p are all integers. Each set of m, n and p forms a resonance line on the tune plane. The sum of the absolute values of m and n is the order of the resonance. In general lower order resonances are more dangerous and need to be avoided. An example of tune diagram is shown in Fig. 1.3 where resonance lines up to third order are plotted. Usually, machine tunes have to be chosen in the (low order) resonance free region.

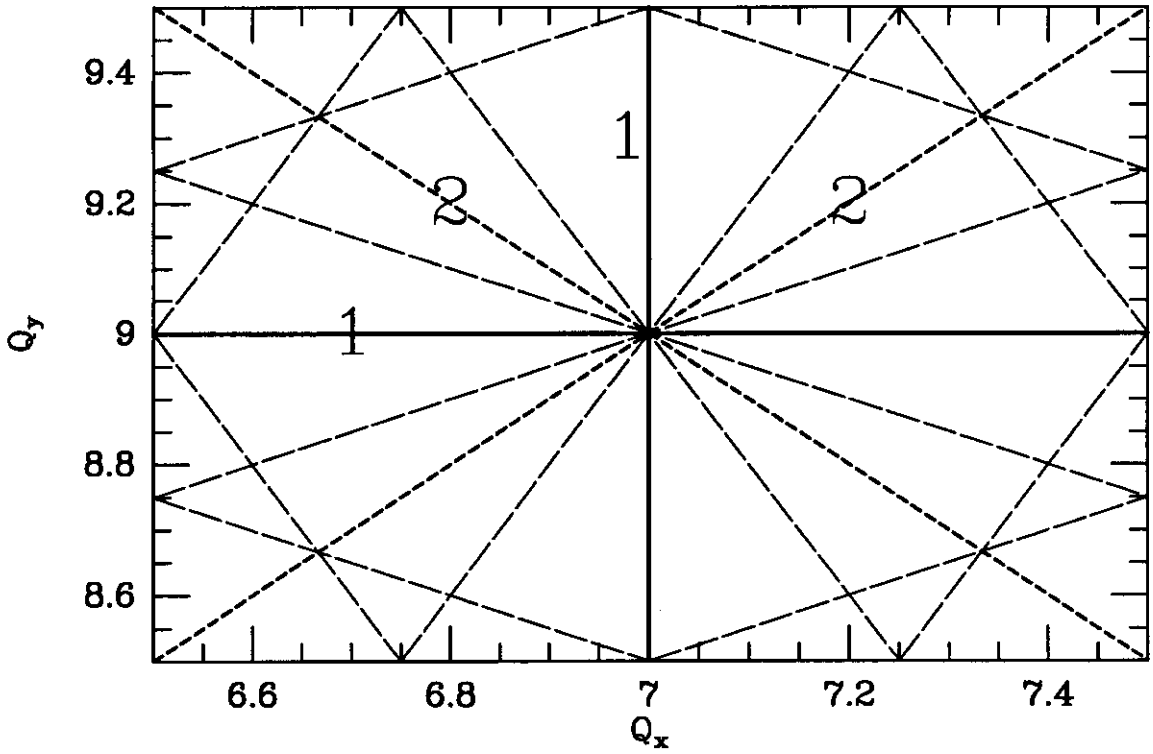

Figure 1.3: A tune diagram with resonance lines up to the third order. Unmarked lines are the third order resonance lines.

1.3 Antiproton Source

The antiproton source collects and stores antiprotons generated from the Main Ring proton beam striking a tungsten target. There are two machines in the source that complete the storing task of antiprotons. The debuncher debunches the short pulses of antiprotons and the accumulator stores and cools the antiproton beam until extracted to the Main Ring. While in all other accelerators the beam exists in the form of bunches, the antiproton beam in the accumulator is unbunched. The layout of the two machines is shown in Fig. 1.4. The antiproton accumulator lattice consists of six nearly identical sectors with each two of them grouped together with mirror symmetry. Sector no. 1–6 of the Accumulator are named as A10–60.

One of the most important parameters in Collider operation is its luminosity which is inversely proportional to the colliding beam's transverse size. In order to maximize the luminosity of the Collider, both proton and antiproton beam must have as small a cross-section as possible. Since $\sigma = \sqrt{\epsilon\beta}$, where σ is the rms size of the beam, ϵ is its rms emittance and β is the Twiss parameter of the machine, keeping luminosity high means keeping beam emittance small if everything else stays the same. Since the rate of antiproton production is a few per million protons per Main Ring proton pulse, the antiproton beam must remain in the accumulator for hours to days in order to accumulate antiprotons to sufficient intensity. The role of the accumulator thus is to accumulate and maintain a large stack of antiprotons for a long time, and cool down and prepare the stack to be extracted to the Main Ring.

1.3.1 Ionization and Ion Trapping

Because of the presence of residual gas in accelerator vacuum chambers, electron-ion pairs are constantly produced through collisions between fast moving beam particles and gas molecules. However, the consequences of their generation can be very different depending upon the charge and species of the beam. Several factors come into play. One is the electric field generated by beam particles. With a positively charged beam, positive ions will be repelled away by the electrostatic field of the beam. With a negatively charged beam the electrons are repelled and the ions can

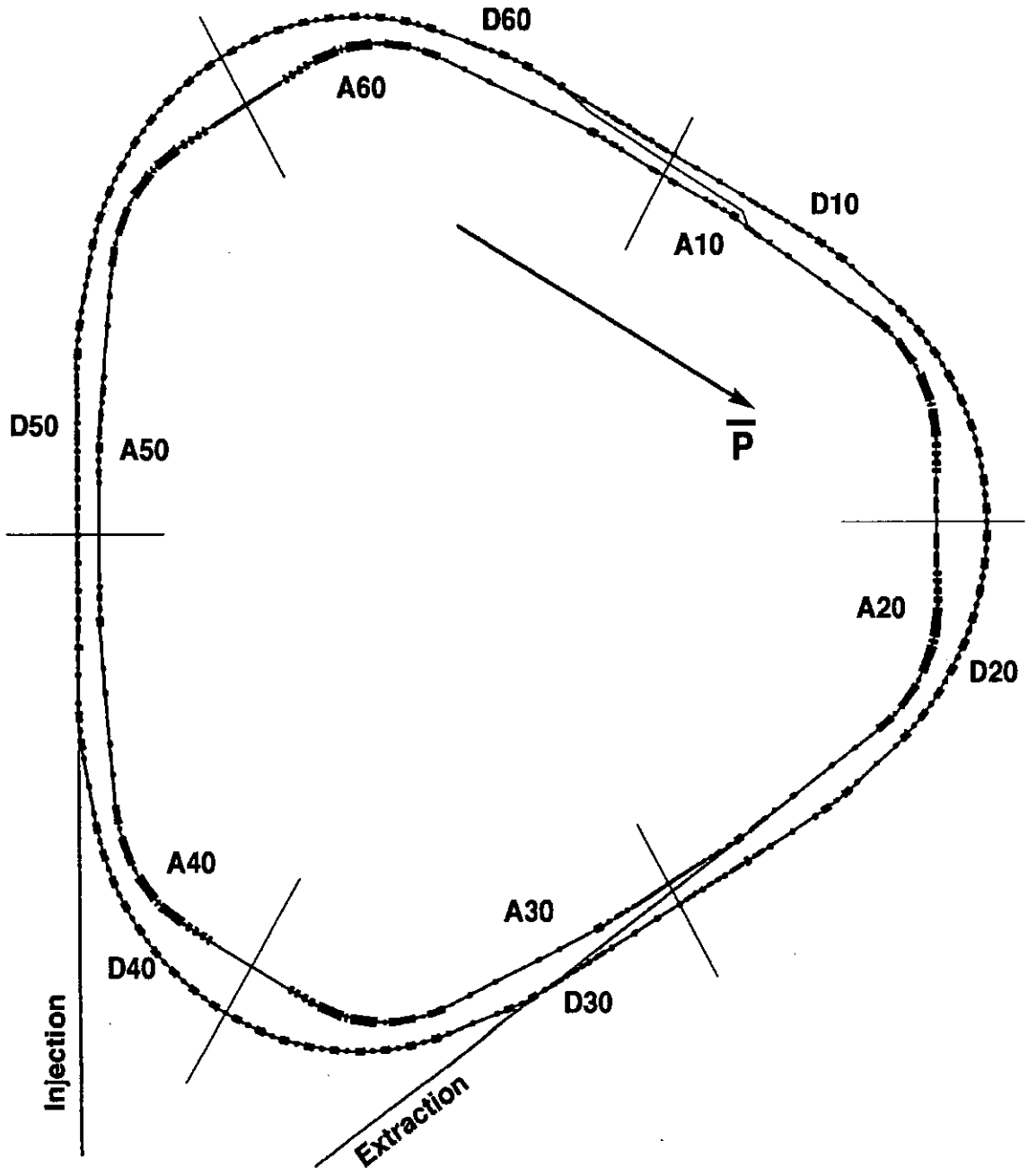

Figure 1.4: Layout of the antiproton debuncher and accumulator. The outside ring is the debuncher and the inside one is the accumulator. Sector no. 1–6 of the Accumulator are named as A10–60.

become trapped. Another factor is the mass difference of electrons and ions. The primary source of ionization is through the collision between beam particles, with velocities close to the speed of light, and either the nucleus or the electrons in residual gas atoms, which are at very low energy. For this kind of collision, the momentum transfer is virtually all transverse and its magnitude per collision is[3]

$$\Delta P = \frac{|eq|}{\beta c}\frac{2}{b} \tag{1.16}$$

where b is the impact parameter, e, q are the charges of the beam particle and either the electron or the nucleus of the gas atom, and βc here is the speed of the beam particle. The average energy transfer in the process is thus

$$\Delta E = \frac{e^2q^2}{mc^2}\frac{2}{\beta^2 b^2} \tag{1.17}$$

or for singly charged particles

$$\Delta E = 2\left(\frac{r_0}{b}\right)^2 \frac{mc^2}{\beta^2} \tag{1.18}$$

where

$$r_0 = \frac{e^2}{mc^2} \tag{1.19}$$

is the classical radius of the particle.

Since ions are at least 1836 times more massive than electrons, they are born with much less kinetic energy. Electrons are born with a much higher kinetic energy and can escape the electric field of the beam much more easily. If a particle that is attracted by the beam field is born with insufficient kinetic energy to overcome the electrostatic potential of the beam it will become trapped. Once a charged particle is trapped, the continued Coulomb interaction with beam particles acts as a heating mechanism, and again this process favors electrons to ions by a factor of their mass ratio.

To quantify these effects, let us take some typical parameters from the Fermilab accumulator and estimate the magnitudes of various quantities. For a two dimensional distribution of points with a density of n, the probability that the nearest neighbor

to a particle occurs between r and $r + dr$ is[4]

$$p(r) = 2\pi r n\, e^{-\pi r^2 n} \tag{1.20}$$

This function has a maximum at $r = 1/\sqrt{2\pi n}$ which is the most probable distance to the nearest neighbor. In the case of ionization or heating through Coulomb collision, r corresponds to the impact parameter b in Eq. 1.18. A beam particle which passes an ion with the smallest impact parameter would have the most energy transfer to the ion by a single particle. For a beam with Gaussian transverse distribution the density of the hit points of beam particles in the cross-section which contains the ion would be

$$n = \frac{N}{2\pi\sigma^2} e^{-\frac{r^2}{2\sigma^2}} \tag{1.21}$$

where N is the total number of points and r is the distance from the beam center. The most probable impact parameter at the beam center will then be

$$b_m = \frac{\sigma}{\sqrt{N}} \tag{1.22}$$

Let us use a typical set of parameters for the accumulator: 10^{12} total number of particles, $\sigma \sim 1.5mm$, revolution frequency $f_0 = 628955Hz$. In one second, the total number of beam particles passing by an ion is $N = 10^{12} f_0$. The most probable shortest impact parameter and the most probable largest single particle energy transfer to a proton are respectively

$$\begin{aligned} b_m &= 2 \times 10^{-12} m \\ \Delta E_m &= 0.001 eV \end{aligned}$$

This is even much less than the thermal energy at room temperature. The energy transfer to an electron would be about $2eV$. The beam potential well depth is on the order of tens of volts for the accumulator, as will be seen in Chapter 2, so it is practically impossible for ions to be created energetic enough to leave the beam. After the ions are created, any single collision with beam particles is unlikely to achieve this goal either, as can be seen from the above example. The effect of numerous collisions with small energy transfer, however, may still heat the ions and drive some of them out.

The result of the difference between ion and electron energy makes "ion" trapping a much more serious problem in negatively charged beam accelerators than those with positively charged beams, and in some cases they pose serious limitations on the machine performance[5][6].

The degree of neutralization is usually represented by the neutralization level

$$\eta = \frac{\text{total charge of ions}}{\text{total beam charge}}$$

It can be easily extended to be a local property, in which case is called the local neutralization level.

The most common positively charged beams are proton and positron beams, and the most common negatively charged beams are electron and antiproton beams. In unbunched, negatively charged beam machines, the neutralization level can reach very close to 100%[7].

In addition to the charge of the beam, the stability of trapped particles is also affected by the whether the beam is bunched or DC. The gaps between bunches leave room for trapped particles to escape, and in general makes ion trapping in bunched beams less of a problem. This will be discussed in greater detail in Chapter 4.

1.3.2 Effects of Ion Trapping

The effect of ion trapping can be categorized as either coherent or incoherent based on the beam response. The incoherent effect can be viewed as a reverse space charge effect. Because the beam is usually at nearly the speed of light, its own space charge force is canceled by its magnetic force to $1/\gamma$ of that of a beam at rest. There is nothing to cancel the space charge force from the trapped ions since they are at very low energies. The space charge of the ions causes shifts in the betatron frequency of individual beam particles. Because this shift is different depending on the position of the particle, as the charge distribution is usually not uniform, it also causes a spread of betatron frequencies. While the average shift can be compensated by adjusting the external focusing strength, the spread cannot be corrected. As the incoherent tune spread of beam particles becomes too large, some of the beam particles will run into high order resonances which may then cause beam heating and even beam loss.

To show one example, in Fig. 1.5 we plot the footprint of a 100mA beam, with 5% and 100% neutralization level, on the tune plane. Non-linear resonances up to 18-th order are also plotted. It is clear from the plot that the tune spread may cause some beam particles to be on non-linear resonances. They provide a heating source and will cause beam emittance growth.

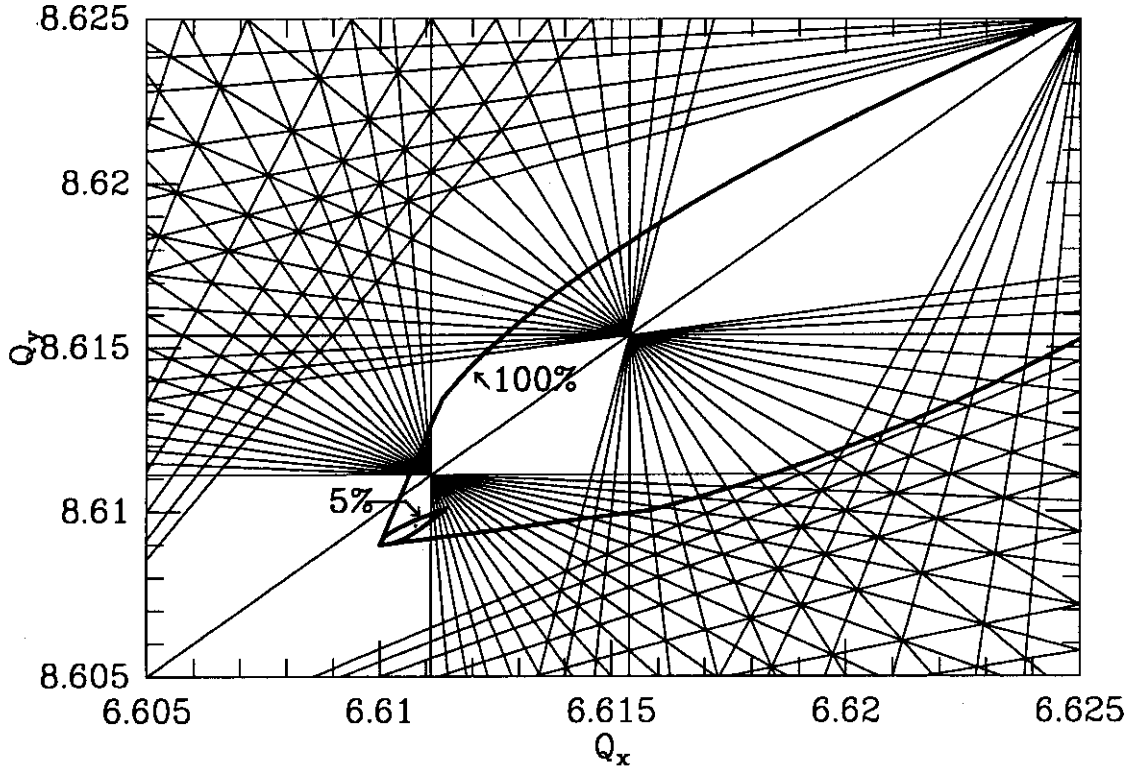

Figure 1.5: Footprint on the tune plane for a 100mA beam. The small "necktie" is for the beam with 5% neutralization level and big one with 100% neutralization. Resonance lines up to 18th order are shown.

The beam and ions as a whole can develop coherent oscillations as well. The oscillation can be expanded into dipole modes where the beam center oscillates, and quadrupole modes where beam size breathes, and so on. The actual coherent motion may be a combination of several modes. While incoherent effects usually evolve slowly with time and incrementally with beam current, coherent effects usually develop much faster and can be disastrous. When any of these coherent oscillations become unstable, they can blow up the beam emittance and may even cause sudden beam loss.

Both the coherent and incoherent effects depend heavily on the neutralization level of the machine.

1.3.3 Preventative Cures

To prevent ion trapping from doing serious damage to beam quality in negatively charged beam machines, several approaches can be taken. The first and most obvious one is to improve the vacuum. The better the vacuum, the longer it takes to neutralize the beam. It is, however, very difficult and costly to improve the vacuum to arbitrarily high levels. The average vacuum pressure in the Fermilab accumulator is already down to a few 10^{-10} Torr. Besides, this approach can only be effective by itself when the vacuum pressure is down to the level such that the neutralization time is comparable to the clearing time due to natural beam heating, which is usually very long. It is usually used in conjunction with other active ion extraction methods.

Clearing electrodes are widely used to directly remove ions. They are usually stripline electrodes to which a certain DC voltage is applied. The clearing voltage should be at least such that the clearing field can overcome the maximum local beam trapping field. However, care should be taken as too high a voltage will produce secondary ions. The electric field generated by these electrodes will either drive local ions towards the electrode or the vacuum chamber wall. The clearing of ions globally can then be achieved via the ions' longitudinal motion. However, as we will see later on, because the beam size and vacuum pipe size change around the ring, the depth of electric potential of the beam changes as well. This will prevent ions from traveling globally, and as a result many clearing electrodes have to be distributed around the machine to avoid high levels of neutralization both globally and locally. Beam Position Monitors (BPM) with an applied DC voltage are commonly used as clearing electrodes.

In bunched-beam machines, an abort gap (removing some bunches from the periodic pattern) is a very effective means to destabilize ions[8], especially light ones. This method and a related alternative way of preventing coherent ion-beam instability, i.e. resonant beam shaking[9][10] will be described in later chapters.

As for any other instabilities, active damping is also a common way to stabilize the beam. A detector senses the coherent oscillation of the beam. The signal, after amplification and phase shifting, is then applied back to the beam through a kicker at another place. Because the kicker can only change the direction rather than the position of the beam, the total phase difference resulting from position difference of the detector and the kicker and from electronic phase shift should have an 90 degrees in addition to the normal phase shift required for negative feedback. As beam-ion instabilities usually occur at low frequencies, the damper system frequency spectrum needs to cover this frequency range.

The effect of the damper system can be measured by its damping time, i.e. an oscillation with an initial amplitude A will have its amplitude damped by the damper system as $Ae^{-t/\tau}$ where τ is the damping time. As long as the growth time of the instability is more than the damping time of the system, the beam will be stable.

1.4 Motivation for the Thesis

Efforts at Fermilab have been directed toward improving the performance of the Tevatron collider. To increase the luminosity the collider needs both high density proton and antiproton beams. The collider upgrade program includes the building of the Main Injector to replace the Main Ring. The Main Injector, together with other improvements, will result in a faster antiproton production rate and the maximum beam current in the accumulator will see a factor of two increase.

As has been noted ion trapping in machines with negatively charged beam, including the accumulator, can severely impair machine performance[5][6] [11]. There is a widely-held belief that even at present the accumulator is limited by trapped-ion-caused instability. With the increased beam current accompanying the upgrade, the ion trapping problem is expected to become worse. Even though there has been some study of ion trapping phenomena and ways to minimize their effects, at CERN, Fermilab and other facilities[7][12] [13][14] [15][16][17] [6][18], the subject is far from being understood. The motivation for this thesis is to investigate the specific ion trapping problems associated with current and future accumulator operation, suggest

preventive measures to minimize any impact that ion trapping might have on beam instability, and at the same time use this unique opportunity to study the ion trapping process in general and its interaction with the beam. The goal is to make direct observations of various interactions of trapped ions with the beam which have not been done previously, and understand them, as well as to attempt to improve those aspects of accumulator performance which are limited by ion trapping.

1.5 Scope of the Project

The remaining sections of this thesis is divided into 5 parts. Chapter 2 concentrates on the accumulator and its various diagnostic systems which are used or related to this study. Some aspects of ion trapping are illustrated with specific applications to the accumulator.

In chapter 3, the general Vlasov approach in the description of beam coherent instabilities is described along with the basic concepts related to it. The treatment is extended to include the effects of trapped ions. The theory is then applied qualitatively to the accumulator and compared to the observations made.

Chapter 4 briefly introduces the ion dynamics issues involved mainly in machines with bunched beams and applies them to the upgraded Tevatron case.

Chapter 5 describes the setup and installation of the Ion Detector and Energy Analyzer. In Chapter 6, the experimental results of the IDEA system are presented, together with analysis and modeling.

Chapter 7 concludes the study and presents directions and possibilities for future ion trapping related studies in the Fermilab accumulator.

Chapter 2

The Fermilab Antiproton Accumulator

The main parameters for the accumulator are listed in Table 2.1.

Kinetic Energy (GeV)		7.9
Circumference (m)		474
Revelution Frequency (kHz)		629
Betatron Tunes	Q_H	6.610
	Q_V	8.809
$\eta = -\frac{df}{f}/\frac{dp}{p}$		0.023
Average Pressure (Torr)		5×10^{-10}

Table 2.1: Fermilab Antiproton Accumulator parameters

Fig. 2.1 shows the Twiss parameters for the Accumulator. The lattice is also shown in Fig. 2.1, with a two-sided box representing a dipole magnet, up-sided box for a horizontally focusing quadrupole magnet and down-sided box for a vertically focusing quadrupole magnet. Since the Accumulator lattice consists of six nearly identical sectors, see section 1.3, only one-sixth of the circumference is shown in Fig. 2.1.

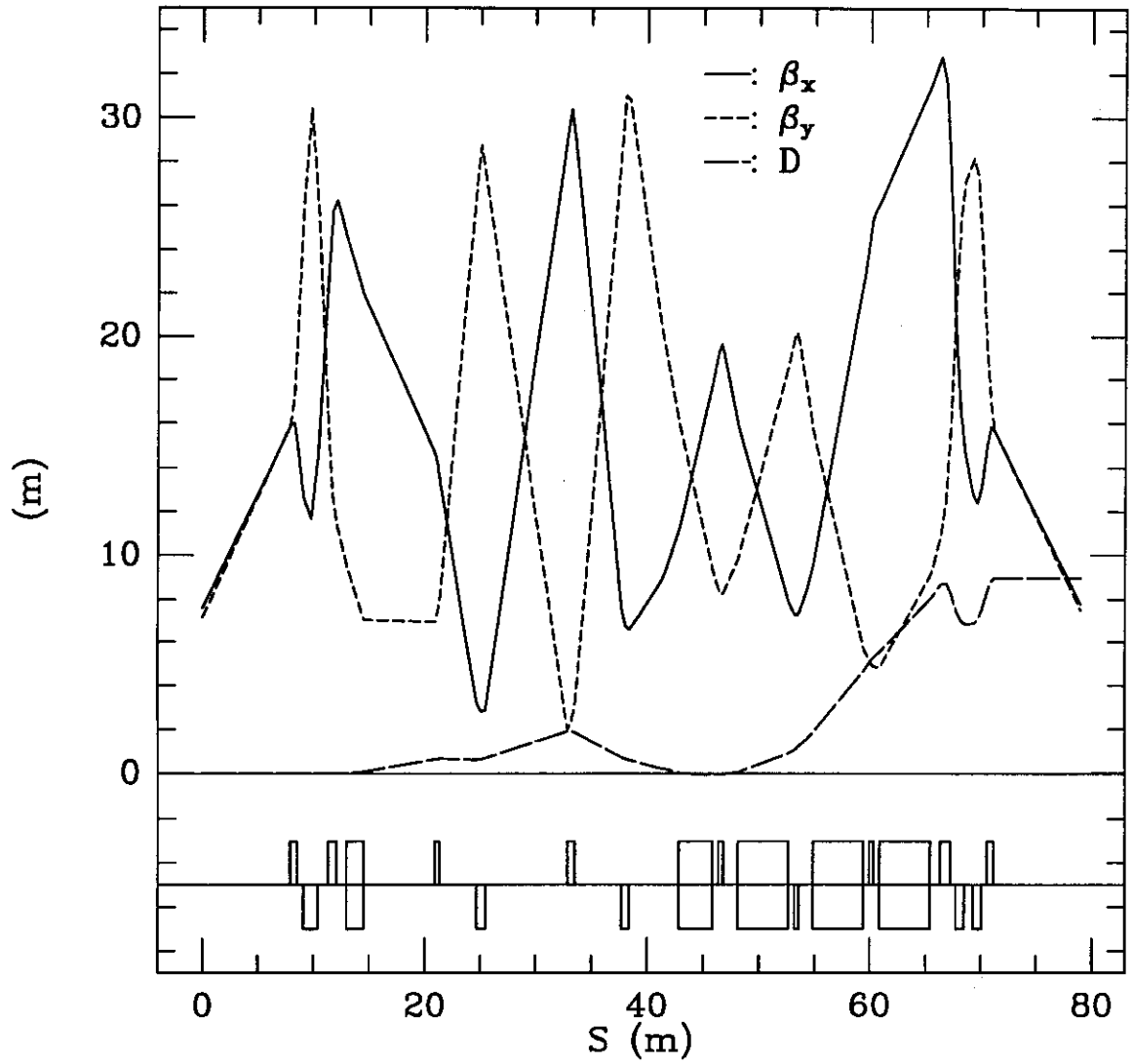

Figure 2.1: Accumulator lattice and Twiss parameters. Up-side boxes represent horizontally focusing quadrupole magnets, down-sided boxes for vertically focusing quadrupole magnets, and two-sided boxes for bending magnets.

Stochastic cooling[19] is used in the accumulator to reduce both the longitudinal and transverse emittance of the antiproton beam. Phase space density and beam lifetime are very important in the accumulator because collider luminosity is proportional to the density.

2.1 Extraction of antiprotons

The requirements on the antiproton beam are closely related to the antiproton extraction process. We will briefly summarize the process and its connection to the ion trapping problem here before the details of the ion trapping problem in the Accumulator are studied in the following sections.

The antiprotons are extracted to the Main Ring in batches. In the present operation they are extracted in 6 batches. The beam is bunched and moved to the extraction orbit. The beam on the extraction orbit has a different momentum from the normal circulating beam which is on the core orbit. In the high dispersion region of the machine the two beams are separated horizontally. The antiprotons on the extraction orbit are then kicked out and transported to the Main Ring without disturbing the particles on the core orbit. The Main Ring has a transverse acceptance of about $1\pi mm \cdot mrad$. The smaller the Accumulator beam transverse emittance, the better is the transmission efficiency. Therefore the beam in the Accumulator has to be cooled as much as possible to increase the antiproton transmission to the Main Ring. A similar situation occurs in the longitudinal dimension, i.e. the higher the longitudinal density of the beam, the more antiprotons can be moved to the extraction orbit and the better transmission to the Main Ring.

As we will see in Chapter 3, beam instability, which ion trapping is known to contribute to, may develop when the beam is cooled. This will cause the beam emittance to experience sudden blowups and sometimes even beam loss which will disrupt the extraction process. In order to avoid the disruptions, beam density and therefore the transmission efficiency has to be sacrificed. If the stability of the beam can be improved by reducing the contribution from trapped ions, the antiproton extraction efficiency and ultimately the collider luminosity can be improved as well.

2.2 Ionization and beam neutralization

When the ionizing collisions between the ionizing particles and the neutral particles are "fast", relative to the mean orbital velocity of atomic or molecular electrons in consideration, the ionization cross-section depends on the kind of the neutral particle and on the speed of the ionizing particle, but not on the charge or on the mass of the ionizing particle[20][21]. The ionization cross-section can be extracted from the Bethe theory and written as

$$\sigma_i = 4\pi \left(\frac{\hbar}{mc}\right)^2 \left(M^2\chi_1 + C\chi_2\right) \tag{2.1}$$

where M^2 and C are constants characteristic of the gas, and

$$\chi_1 = \frac{1}{\beta^2} \ln \frac{\beta^2}{1-\beta^2} - 1 \tag{2.2}$$

$$\chi_2 = \frac{1}{\beta^2} \tag{2.3}$$

with $\beta = v/c$. Antiprotons in the accumulator are ultra-relativistic with $v = 0.99c$, so we can use the values of constants presented in [20]. The residual gas composition of the accumulator has been measured with RGA's (Residual Gas Analyzer)[22] and the results are tabulated in Table 2.2.

Mass (atu)	Possible Gas Type	Percentage (%)
2	H_2	83
15–16	CH_4	2
17–18	H_2O	5
26–28	CO, N_2, C_2H_2, C_2H_4	5
40–44	CO_2	2
Other		3

Table 2.2: Accumulator residual gas composition

For the accumulator $\chi_1 = 3.54$ and $\chi_2 = 1.01$. The constants M^2 and C extracted from [20] are listed below for the relevant gas molecules. The average ionization cross-

Gas Type	M^2	C	$\sigma(cm^2)$
H_2	0.695	8.115	2.00×10^{-19}
CH_4	4.23	41.85	1.07×10^{-18}
H_2O	3.24	32.26	8.26×10^{-19}
CO	3.70	35.14	9.11×10^{-19}
N_2	3.74	34.84	9.08×10^{-19}
C_2H_2	5.21	53.76	1.36×10^{-18}
C_2H_4	6.75	68.82	1.75×10^{-18}
CO_2	5.75	55.92	1.44×10^{-18}

Table 2.3: Constants and ionization cross-sections for the molecules

section, given the proportions of each possible type of gas in Table 2.2, is thus about $\sigma_i = 3.4 \times 10^{-19} cm^2$. The neutralization time T_n, defined as the average time it takes for one circulating particle to create one ion, is

$$T_n = \frac{1}{n_g \sigma_i \beta c} \tag{2.4}$$

where n_g is the number density of the residual gas molecules. At standard room temperature the accumulator residual gas molecule density is

$$n_g = 7.1 \times 10^6 / cm^3$$

and the neutralization time for a vacuum pressure of 5×10^{-10} Torr is

$$T_n = 5.6 \ sec$$

2.3 Beam Potential and Clearing Electrodes

2.3.1 Electrostatic Potential of the Beam

As we have stated before, the use of clearing electrodes is the most basic and efficient way to get rid of most of the ions. It can also provide a lot of information to help diagnose other problems. Before the clearing electrode system upgrade was made, ion trapping was believed to be limiting the machine performance, and it is

expected to continue to be one of the most important factors affecting the accumulator performance in the collider upgrade program. As the maximum stack increases, the clearing voltage should also increase, and we believe improving the clearing electrode system will greatly benefit the operation of the accumulator.

In all of the following calculations, we have taken the nominal beam parameters for the upgrade, i.e. $200mA$ of beam current with $2\pi mm \cdot mrad$ transverse emittance and 2.0×10^{-4} for $\delta p/p$.

As we have seen from section 1.3.1, ions are generated with very little kinetic energy, so the magnetic field generated by the beam particles has little effect on the ions. The electric field of the beam, however, is the cause of ion trapping. The beam pipe is, of course, at ground. Variations in vacuum pipe size and shape, as well as the change in beam size, cause the electrostatic potential at the beam center to vary around the ring. Ions are trapped transversely by the beam field, but because of this longitudinal potential variation, ions may drift longitudinally depending on where they are born. This requires the clearing electrodes to be properly placed at the right positions to avoid local ion pockets. In addition, the electric field generated by the electrodes must at least overcome the local maximum electric field due to the charge of the beam particles. Therefore, a detailed knowledge of the beam potential and electric field distribution around the machine is needed to determine the optimum positions and voltages for the clearing electrodes.

Since the beam size usually changes longitudinally on a scale much larger than the beam and vacuum pipe transverse size, we can treat this as a two dimensional problem, i.e. an infinitely long beam inside an infinitely long conducting boundary with the local transverse geometry. We will use a model of the beam that has a bi-Gaussian transverse density distribution. Details of the calculation for such a beam are in Appendix A.

The Fermilab accumulator vacuum pipe is composed mainly of sections with circular, rectangular, oval and star shaped cross-sections. Typical sizes of those cross sections are shown in Fig. 2.2. In order to avoid having to use a sophisticated Maxwell equations solver, in the calculation oval sections are approximated with elliptical ones and the star shaped cross section is approximated by a square. A computer program

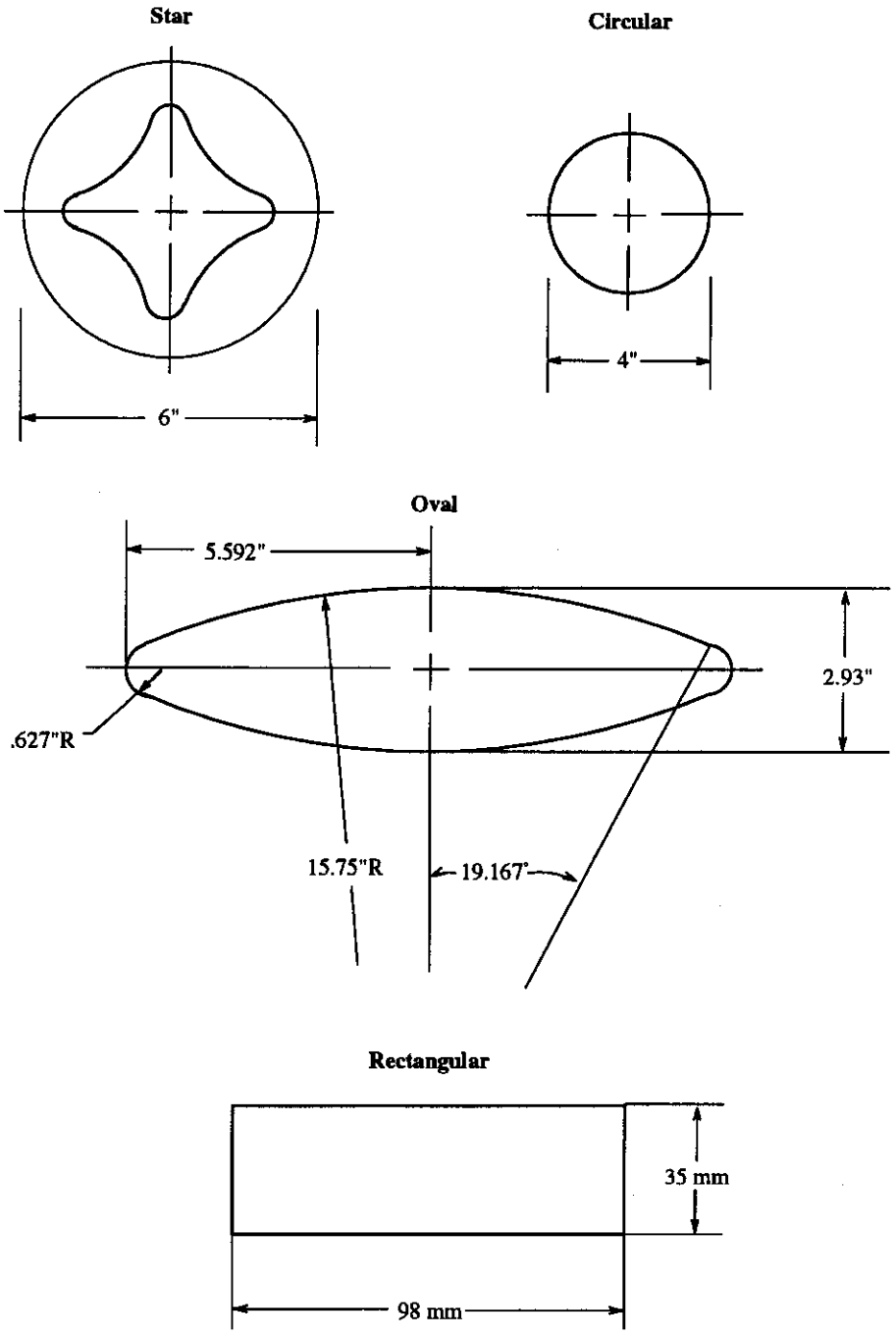

Figure 2.2: Typical vacuum pipe geometries and sizes

originally developed at CERN[23] was extended and used. With 2×10^{12} circulating antiprotons, the electrostatic potential at the beam center is shown in Fig. 2.3 as a function of longitudinal position. The locations of dipole and quadrupole magnets are also indicated in Fig. 2.3. Because the ring has a superperiodicity of 3 with mirror symmetry in each super-period, only one sixth of the total circumference is shown.

2.3.2 Clearing Electrode System

Because the beam potential has many local minima, both the position and the clearing field strength of clearing electrodes are important. Improper placement of clearing electrodes will allow local ion pockets to be formed. To avoid any ion pockets, there should be at least one electrode in every potential minimum. In the accumulator all the BPMs also act as clearing electrodes. The DC clearing voltage on the BPM electrodes is isolated from the BPM electronics. The use of BPM electrodes as clearing electrodes is not only convenient, since there are a large number of BPMs distributed around the whole machine, but is also beneficial to beam stability concern. Every electrode is also a source of impedance and a large machine impedance will cause coherent beam instability, see Chapter 3. The BPMs are distributed nearly identically for all six sectors. There are also dedicated clearing electrodes and they are also distributed roughly the same for the six sectors. For historical reasons, the current on each electrode was not measured individually, instead, all electrodes in one sector were tied together. They shared the same power supply and only the total current was measured. The positions and kinds of clearing electrodes in sector 6 are shown in Fig. 2.3 together with the beam's electrostatic potential which we calculated previously. The beam parameters used in the calculation of potential are $I = 200mA, \epsilon_{x,y} = 2\pi mm \cdot mrad, \sigma_p/p = 2 \times 10^{-4}$. It can be seen from Fig. 2.3 that there are still a small number of potential minima that do not have clearing electrodes present. More dedicated clearing electrodes are being constructed at the writing of this thesis, and are planned to be installed soon.

Clearing electrodes not only clear ions and greatly reduce the neutralization level of the machine, they can also provide valuable information. The total clearing current

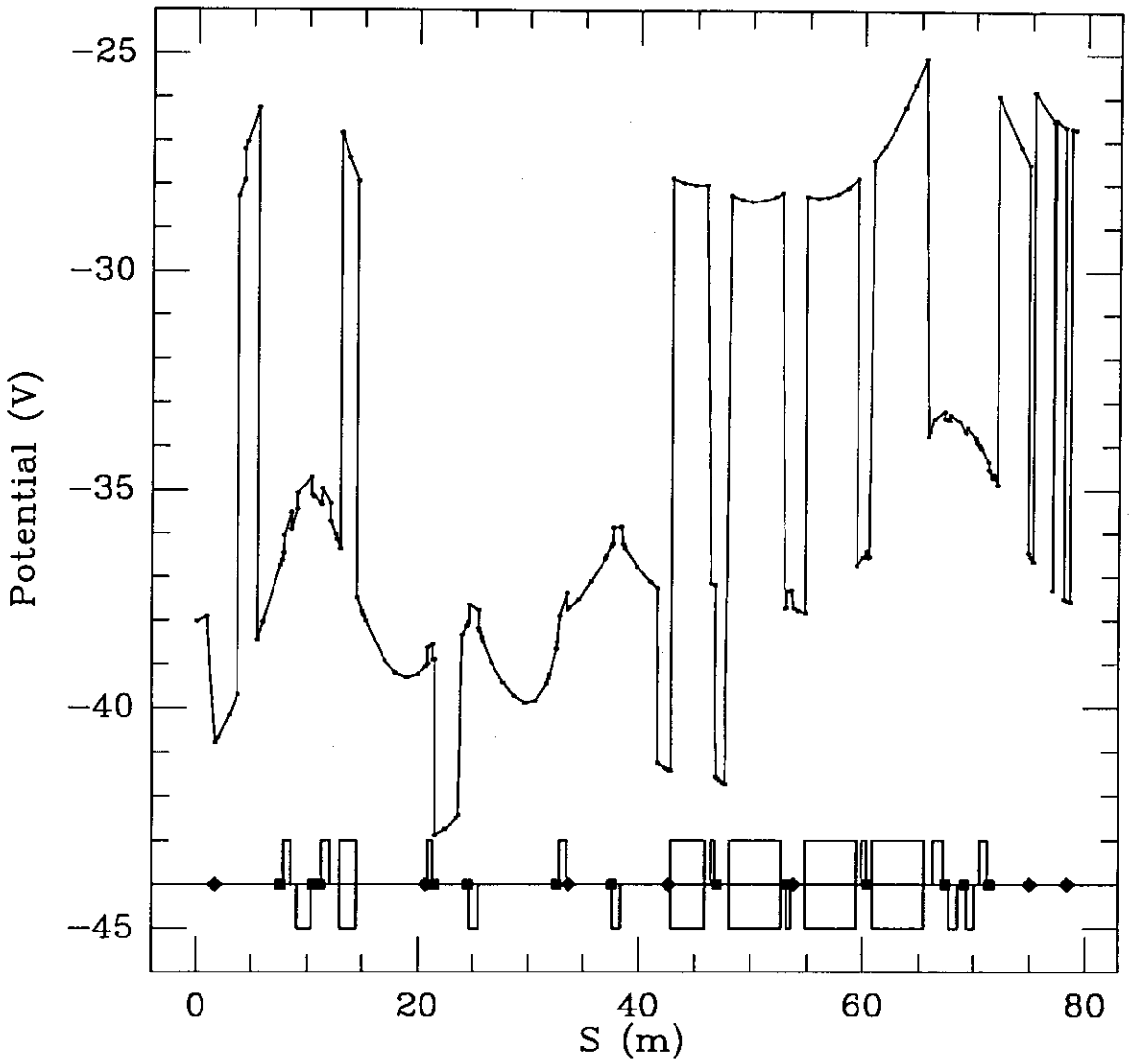

Figure 2.3: Longitudinal beam potential Variation. Black squares represent BPM electrode used as clearing electrodes and diamonds represent dedicated clearing electrodes.

gives the rate with which ions are created, to first order at least. This rate should be proportional to the beam current in the machine. However, because a considerable leakage and/or other electronic offsets exist in the clearing current measuring system, direct determination of the neutralization time from the absolute measurement of clearing currents is not reliable. A better approach is to measure the rate of change of clearing current vs. beam current, i.e. the slope of clearing current vs. beam current.

Several other factors, however, still affect this measurement. An obvious one is a change in the vacuum pressure. Because ion gauges are spread far apart, this information cannot be accurately measured. In the slope measurement mentioned above, which spans a wide time period from many hours to days, the effect of vacuum pressure fluctuations can be ignored if no long term drift in vacuum pressure exits.

The ions reaching the clearing electrodes may create secondary emission of electrons and thus gives rise to a false increase in the measured currents. The increase would be proportional to the total clearing current, so it will increase the slope of clearing current vs. beam current. This effect would decrease with decreased clearing voltage, but then it has to be separated from the decrease due to incomplete clearing.

The tail of the beam may directly hit electrodes also causing secondary emission. If the beam scrapes a given device it may also cause outgassing from the local device or from the vacuum pipe which will increase the rate of ion generation and therefore the measured clearing current. These two effects relate to beam loss and beam position and size. If the beam orbit alignment is done carefully, they should not affect the measurement too much, especially with small beam currents.

Finally, there will inevitably be ions that go to and are collected by the vacuum pipe wall, thus escaping their inclusion in the measured clearing current. As we will see in chapter 6, this contribution is a very small proportion of the total ion production and can be ignored.

Despite all these perturbations, the clearing system can nevertheless provide a relatively good measurement of the neutralization time. In Fig. 2.4 a set of plots of beam and clearing currents vs. time and their linear fits for all six sectors are shown. The neutralization time is related to the slopes of the plots by

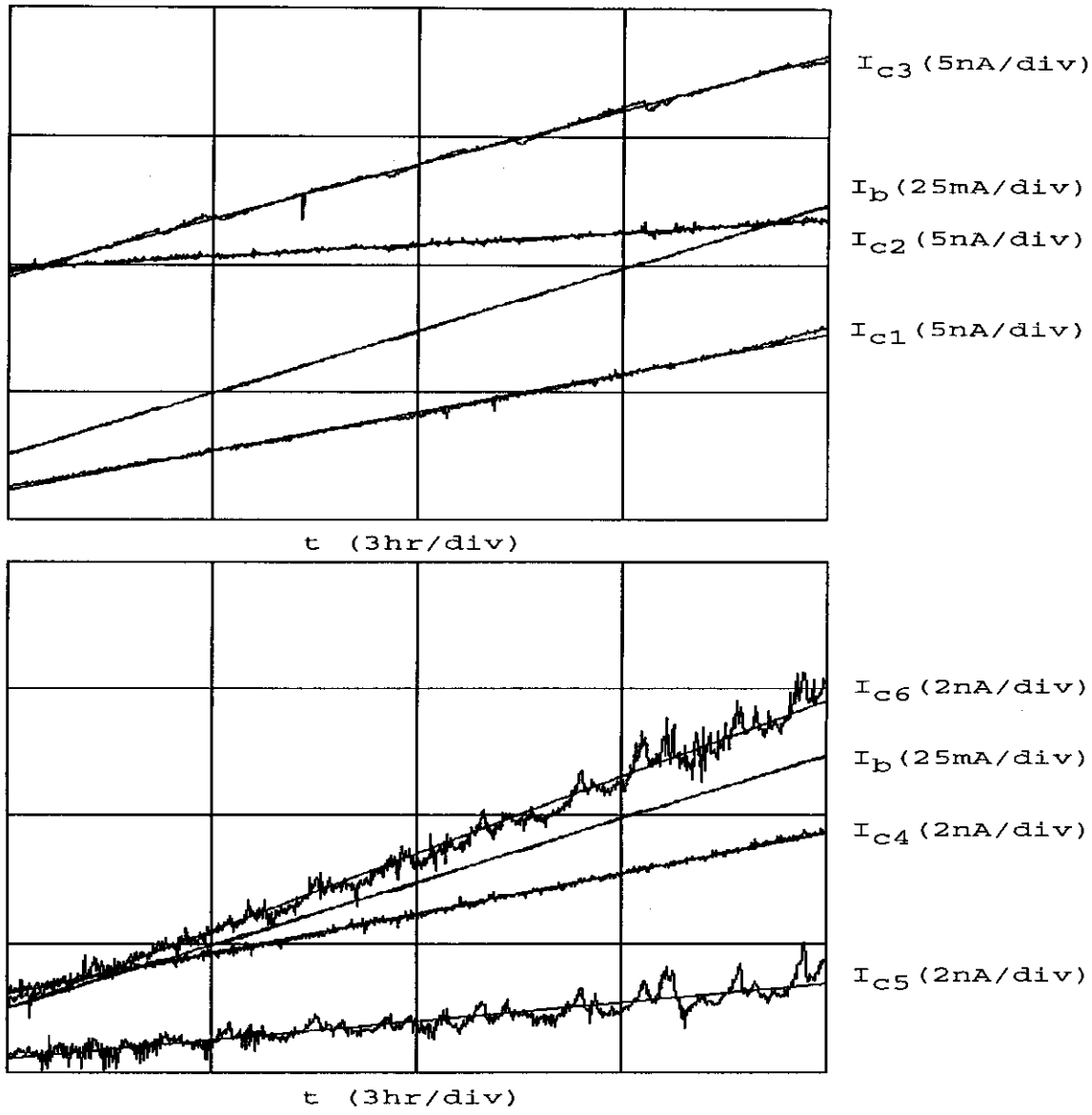

$I_b = 0.001135 \times t + 12.55$

$I_{c1} = 0.000142 \times t + 1.153$ $\quad I_{c2} = 0.0000445 \times t + 9.863$

$I_{c3} = 0.000197 \times t + 9.672$ $\quad I_{c4} = 0.0000574 \times t + 1.240$

$I_{c5} = 0.0000271 \times t + 0.226$ $\quad I_{c5} = 0.000111 \times t + 1.002$

Figure 2.4: Beam and clearing current vs. time. I_{ci} is the clearing current in i-th sector. See Fig. 1.4 for the definition of sectors.

$$T_n = (\frac{dI_c}{dQ_b})^{-1} = \frac{1}{f_0}\frac{dI_b/dt}{dI_c/dt} \tag{2.5}$$

where I_c is the total clearing current, Q_b and I_b are the total beam charge and current respectively, and f_0 the revolution frequency. The slopes extracted from Fig. 2.4 for each sector are listed in Table 2.4. The overall neutralization time measured is thus

sector no.	1	2	3	4	5	6	total
$\frac{dIcn}{dIb}(10^{-6})$	0.125	0.039	0.174	0.051	0.024	0.0978	0.37

Table 2.4: Relative neutralization rate

4.3 seconds. Comparing with the direct calculation in section 2.2, this measured neutralization time agrees with the calculation within a factor of 2. Just as there are some uncertainties related to the neutralization time measurement, so are there uncertainties related to the calculation. The biggest one is in the vacuum pressure. Ion gauges in the accumulator are few and far between and as a result they cannot give an accurate picture of the pressure distribution. They only serve as an order of magnitude check. The pressure we used in the calculation may be off by as much as a factor of two. From the clearing current data, it is obvious that the pressure varies quite a lot from sector to sector. The measurement result should be a more reliable estimate than the calculation. Despite all the uncertainties, it is safe to say that the calculation and measurement results agree quite well, at least they are consistent with the ion gauge measurement.

2.3.3 Clearing Electrode System Upgrade

The old Accumulator clearing system had a fixed $100V$ voltage capability and clearing current monitoring was done on a sector by sector basis. Since this system was initially installed when the Accumulator was built in 1984[24][25], we need to examine it and determine whether it is adequate for current machine operation and whether it is enough for conditions expected in the Collider upgrade.

The potential distribution calculated in section 2.3.1 cannot be used directly to determine the clearing electrode voltage. Specifically, assuming clearing electrodes are flush to the beam pipe, twice the beam center potential will not be enough to completely extract locally trapped ions, instead a smaller potential well remains. Fig. 2.5 illustrates this effect. What determines the necessary clearing voltage are the maximum beam trapping field and the electrode separation.

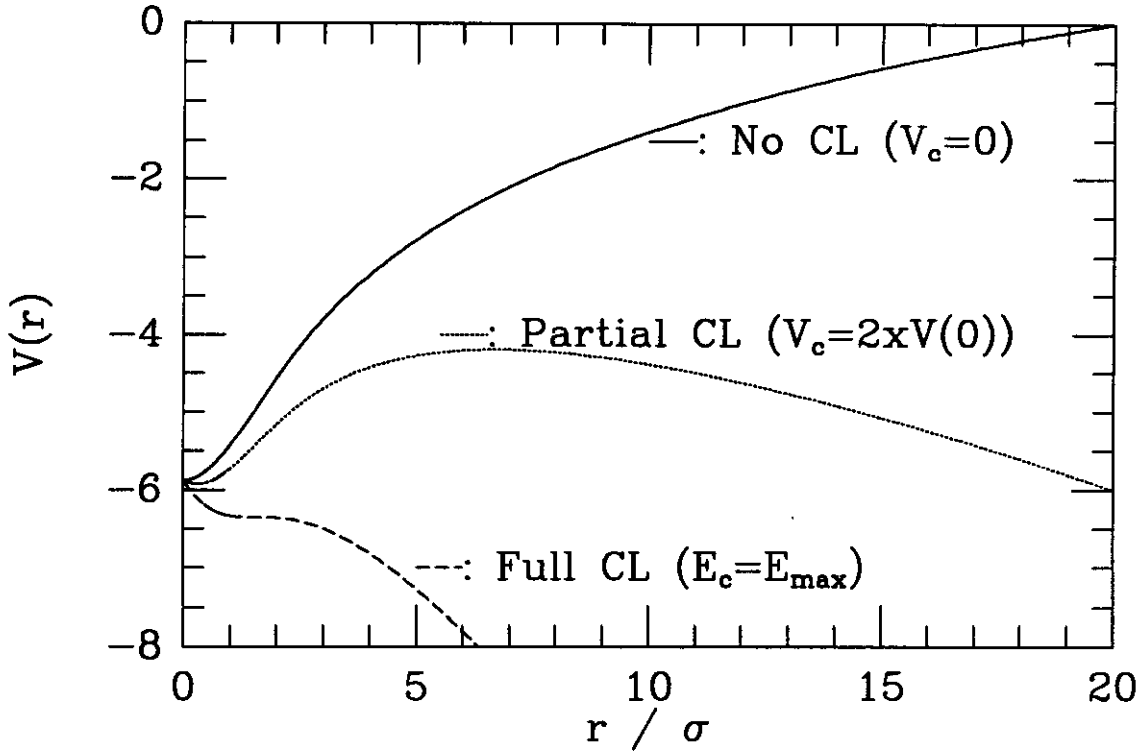

Figure 2.5: Beam potential with different levels of clearing voltage. CL stands for CLearing.

The electric field of a charged particle beam with a bi-Gaussian cross-section is[26]

$$\begin{pmatrix} E_x \\ E_y \end{pmatrix} = \frac{\sqrt{2\pi}\lambda Z}{\sqrt{\sigma_x^2 - \sigma_y^2}} \begin{pmatrix} Im \\ Re \end{pmatrix} \left\{ W\left(\frac{x+iy}{\sqrt{2(\sigma_x^2-\sigma_y^2)}} \right) - e^{-\frac{1}{2}\left(\frac{x^2}{\sigma_x^2}+\frac{y^2}{\sigma_y^2}\right)} W\left(\frac{x\frac{\sigma_y}{\sigma_x} + iy\frac{\sigma_x}{\sigma_y}}{\sqrt{2(\sigma_x^2-\sigma_y^2)}} \right) \right\} \tag{2.6}$$

where Z is the charge state of the particles and λ the line density of the beam, σ_x

and σ_y are the horizontal and vertical rms beam size respectively. W is the complex error function defined by

$$W(z) = e^{-z^2}\left(1 + \frac{2i}{\sqrt{\pi}}\int_0^z e^{t^2}\,dt\right) = e^{-z^2}(1 - \mathrm{erf}(-iz)) \tag{2.7}$$

The relative magnitudes of the electric field are plotted in Fig. 2.6 for both a round beam and a beam with an aspect ratio $\sigma_y/\sigma_x = 4$ which is about the maximum value $\sigma_{y,x}/\sigma_{x,y}$ achieves in the accumulator. The maximum electric field occurs at $r = 1.6\sigma$ for a round Gaussian beam. When $\sigma_x \neq \sigma_y$, the field distribution has a maximum on the short axis, but not exactly at 1.6σ, and a saddle point on the long axis. As we can see from Fig. 2.6, however, the field distribution around the maximum is quite flat and the field at 1.6σ on the short axis is very close to the real maximum. In the case of $\sigma_y/\sigma_x = 4$ that is only 2% off. The "maximum" transverse electric field is thus calculated for one sector and is shown in Fig. 2.7.

The maximum clearing voltage needed is simply the maximum field times the maximum beam pipe dimension, which is $0.28m$, so the clearing voltage needed is determined to be $1kV$. Actually the maximum field does not occur at places where maximum beam pipe size is large, thus $1kV$ has some safety factor built into it.

The clearing electrode system has been recently upgraded to have a maximum clearing voltage of $1kV$. The calculation has indicated the old clearing electrode system is indeed inadequate. Immediately after the clearing voltage was raised in November of 1992 a record luminosity then was achieved. The main reason was that the beam was stable enough for the $4-8GHz$ longitudinal stochastic cooling system to be turned on. It provided additional longitudinal cooling and further increased the longitudinal density which increased the number of antiprotons extracted to the Main Ring. The clearing electrode system upgrade has brought significant improvements to the Accumulator performance[27]. Fig. 2.8 summarizes the improvement by showing the transverse beam size and longitudinal density of the beam for many pbar extractions before and after the clearing electrode upgrade. As can be seen from Fig. 2.8 beam longitudinal density nearly doubled at the 90% transmission efficiency emittance after the upgrade.

The effect of the clearing fields on the beam is negligible because of the high

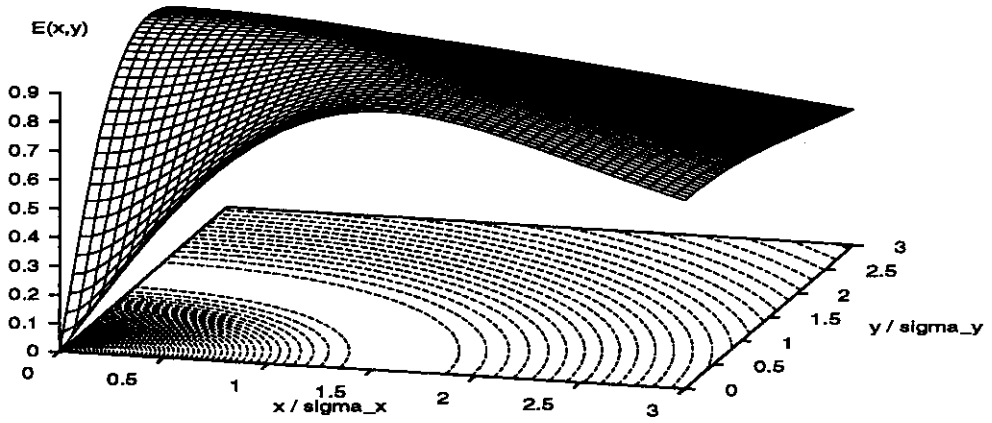

(a)

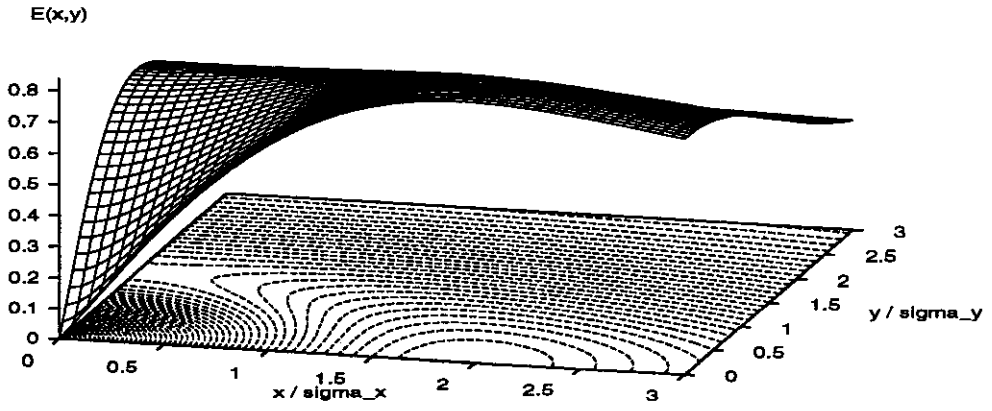

(b)

Figure 2.6: Relative electric field distribution in bi-Gaussian beams
(a): Round beam, (b): $\sigma_y/\sigma_x = 4$

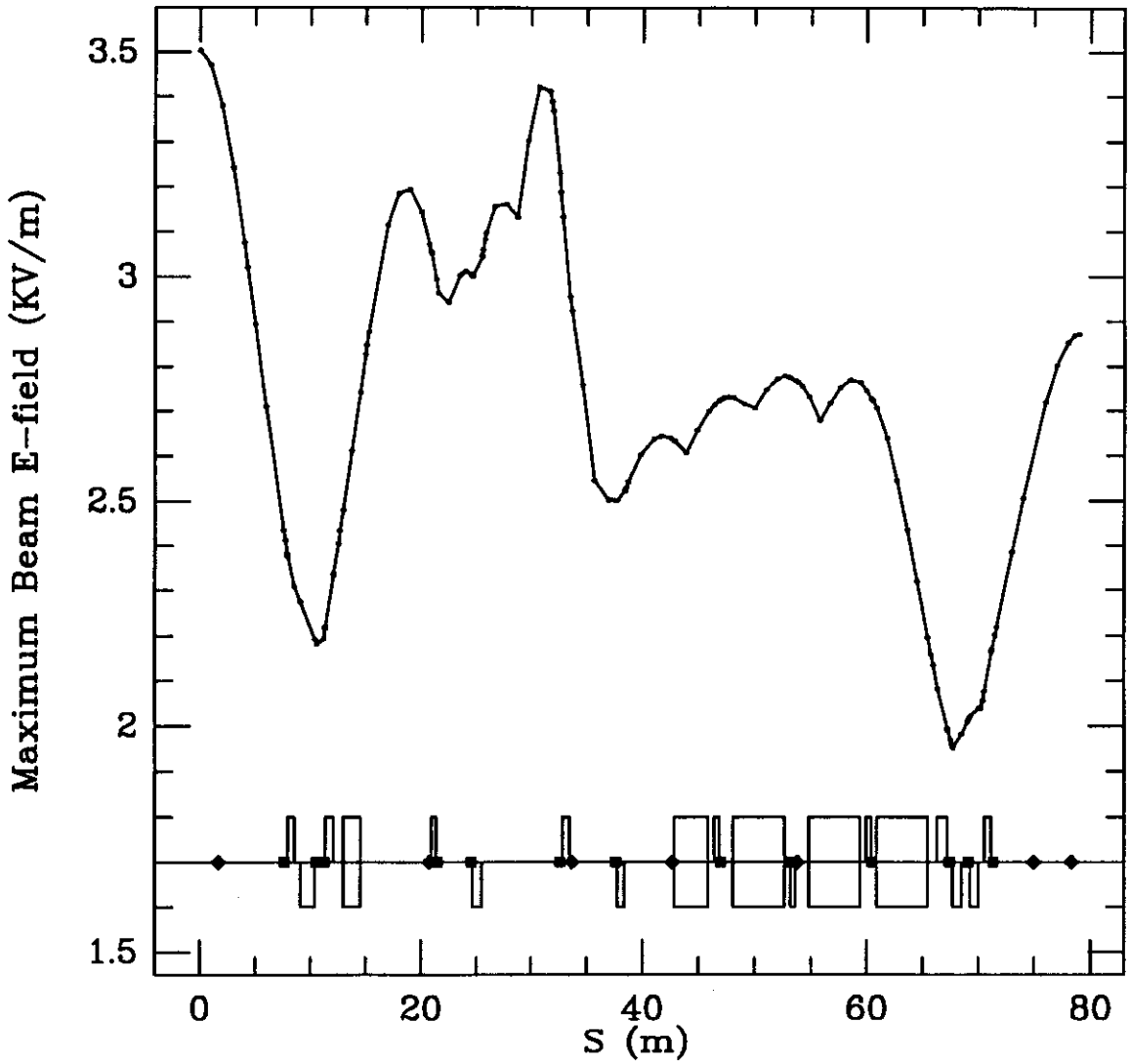

Figure 2.7: Distribution of maximum transvese electric field

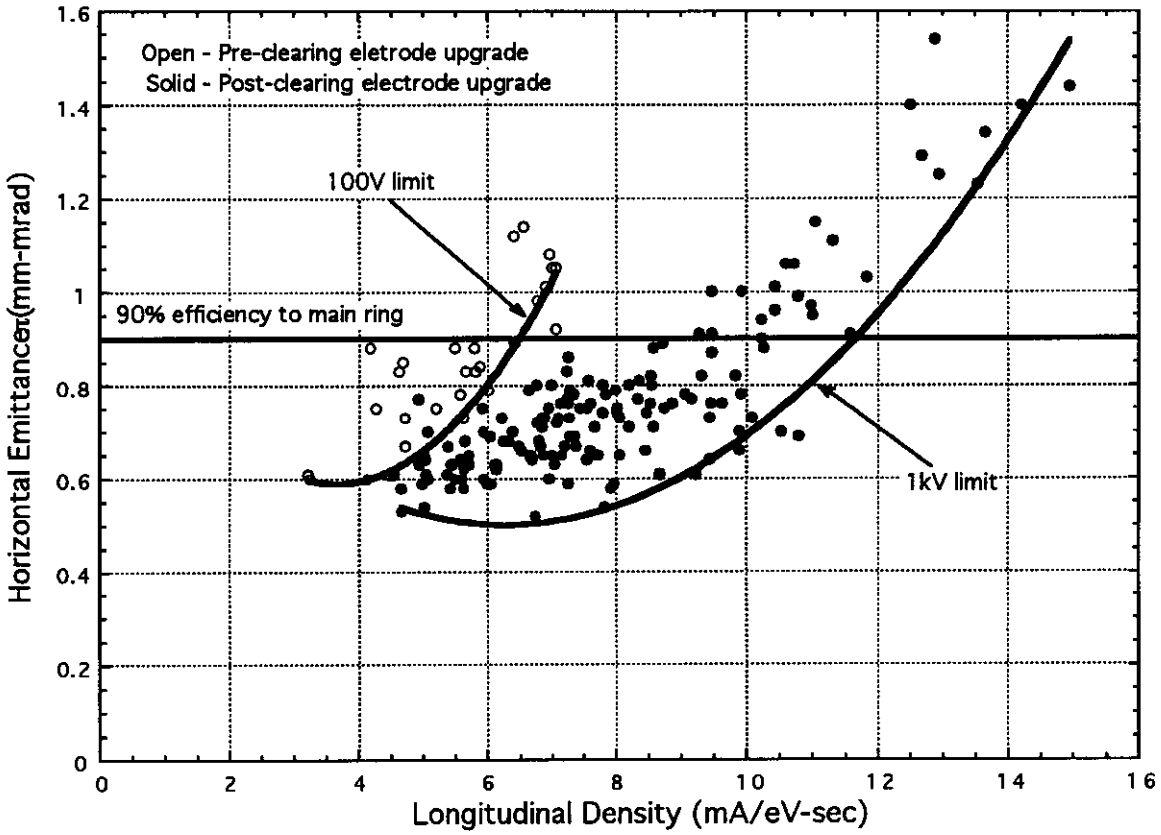

Figure 2.8: Antiproton beam quality comparison before and after the ion clearing upgrade. The data points give the stable beam conditions. The fitted lines show the limits before (100V limit) and after (1kV limit) the upgrade.

momentum of th beam. This can be easily estimated. The typical beam pipe is 4 inches in diameter. With 1kV voltage the transverse electric field is $E \approx 10^4 V/m$. A clearing electrode is about 20cm in length, so the kick a beam particle receives as it passes a pair of electrodes is

$$\Delta x' = \frac{\Delta p_\perp}{p_\parallel} = \frac{eEL}{p_\parallel} \approx 2 \times 10^{-7} rad \tag{2.8}$$

where L is the length of the electrode, $p_\parallel = 8.8 Gev/c$ is the particle's longitudinal momentum. Considering that a beam with $1\pi mm \cdot mrad$ emittance (95% of the beam) has an rms beam size of about 1.5mm and thus an rms x' of about $10^{-4} rad$, this transverse kick is indeed negligible.

In addition to the increase of clearing voltage, clearing current monitoring has also been improved. Instead of the sector by sector monitoring, electrodes in each sector are grouped into about eight sets and each set has an independent clearing current readout. This capability enabled us to perform the following measurement to verify the beam potential distribution model that was presented in section 2.3.1. At the beginning of the experiment, the clearing currents of all the electrode groups were averaged and recorded as the base currents. The supply to each group of electrodes was successively disconnected temporarily to record the change in clearing current distribution. The ion flux that would otherwise be extracted by the electrodes being disconnected should redirect itself according to the local potential distribution, e.g. if there is a high potential barrier on the left hand side of the electrodes and a potential well on the right hand side, then disconnecting this group should result in almost all the ion flux flowing to the right resulting in a large increase of clearing current on the electrodes to the right and minimum increase on those to the left. Two measurements in sector A10 together with its beam potential distribution are shown in Fig. 2.9. The beam parameters for the measurements and beam potential calculations are: beam current $I = 67mA$, horizontal emittance $\epsilon_h = 1.1\pi mm \cdot mrad$, vertical emittance $\epsilon_v = 0.7\pi mm \cdot mrad$, and rms momentum spread $\sigma_p = 2.3 MeVc$. The situations in sector A60, shown in Fig. 2.10, is very similar to that in sector A10 because of their similar local beam potential structure. The measurement in sector A30, see Fig. 2.11, however, behaves very differently from the corresponding one in sector A10. The

difference can be attributed to the local devices which have significantly altered the local beam potential distribution which are reflected in the calculation result plotted together.

2.4 Diagnostic System and Instrumentation

2.4.1 Schottky Pickups

Schottky noise, named after Walter Schottky for his discovery and study of the random thermionic emission in vacuum tubes arising from the independent motions of individual particles, is an important beam diagnostic tool. The beam consists of a large, but finite, number of particles. Each particle will give rise to its own excitation in the detection device. The random, fluctuating component is called the Schottky noise, the detection of which is the basis for the stochastic cooling technique. The Schottky signal is much easier to observe in DC beam machines than bunched beam machines because of the absence of the much stronger coherent signals which occur in bunched beams. Schottky signal analysis is a very powerful tool to study the machine and beam behavior, e.g. the longitudinal Schottky spectrum gives the momentum distribution of beam particles because of the relation between revolution frequency and momentum deviation (Eq. 1.3). The power in each of the transverse Schottky spectrum bands is proportional to the beam emittance[28]. This is one way the accumulator emittance is measured. Betatron tunes are also measured with transverse Schottky signals.

The Fermilab accumulator has 10 transverse and 3 longitudinal Schottky pickups in different frequency ranges[29].

2.4.2 RF System

There are three RF systems in the accumulator, one with $h = 84$ and two others with $h = 2$, where the harmonic number h is the ratio of the RF frequency to the beam revolution frequency. One of the two $h = 2$ systems has a suppressed RF cycle in every two cycles, which means half of the beam will not see any RF fields. In some

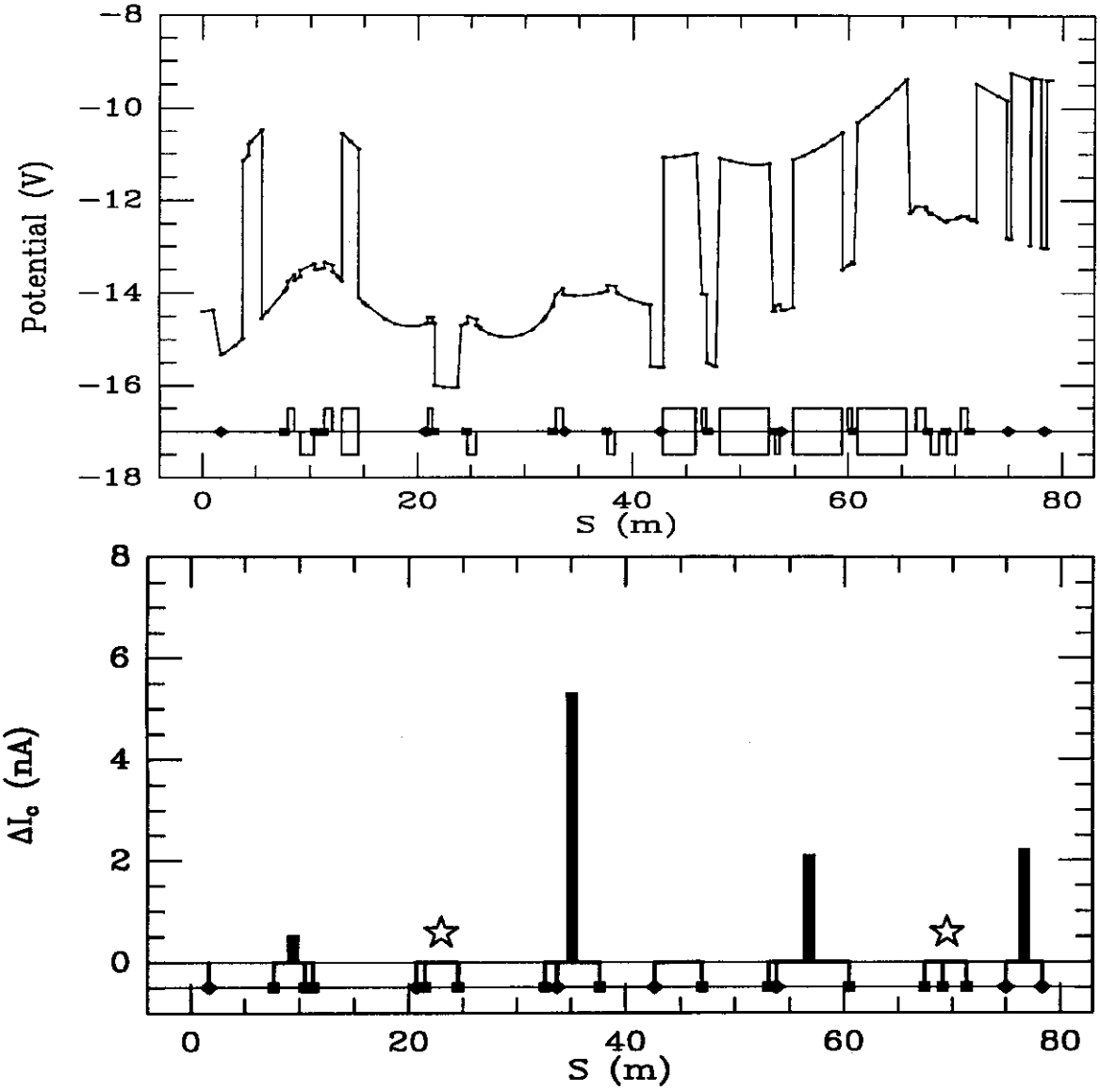

Figure 2.9: Clearing current re-distribution in sector A10 with some electrodes turned off. Electrode sets marked with $\star$ are off.

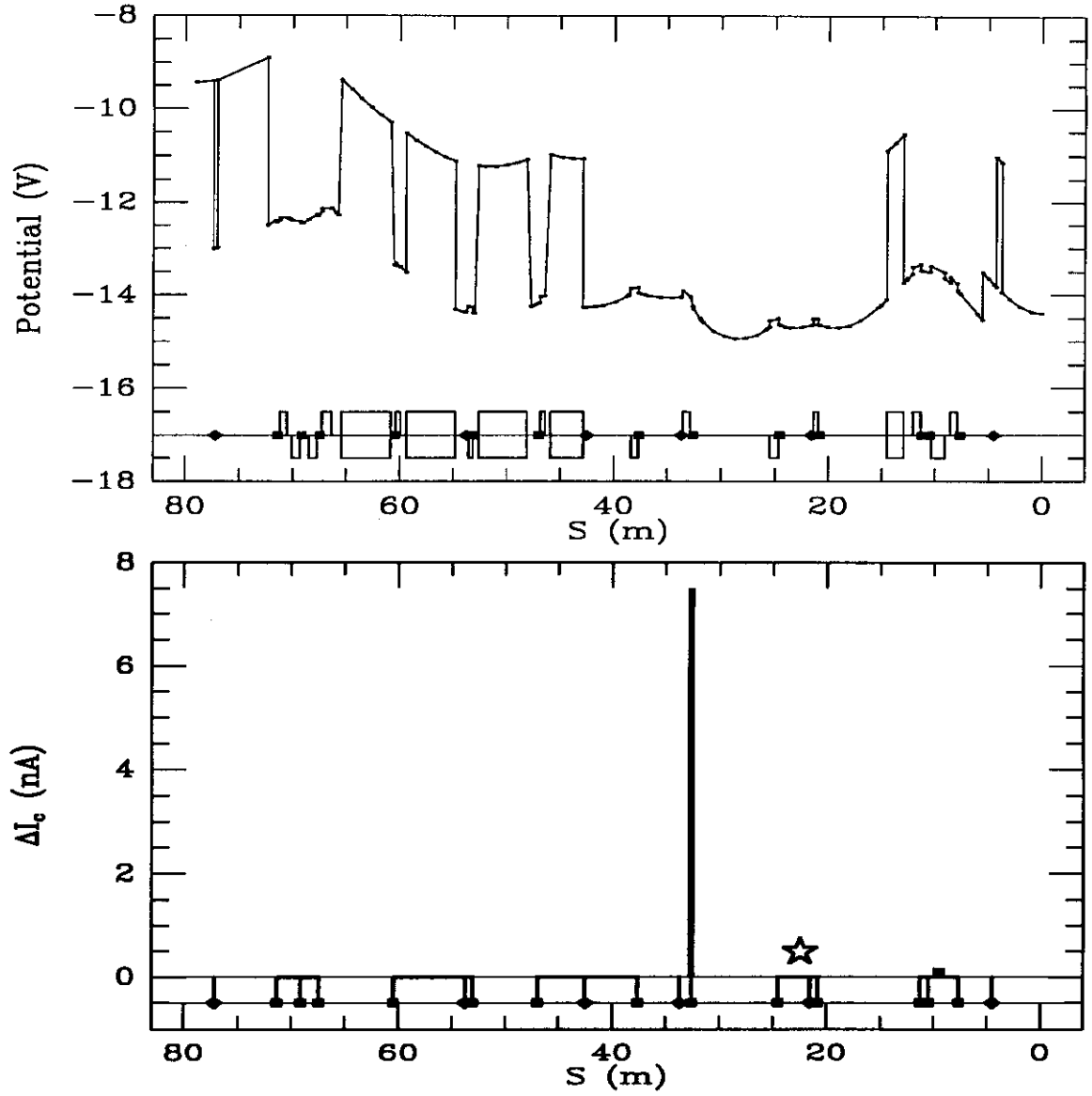

Figure 2.10: Clearing current re-distribution in sector A60 with some electrodes turned off. Electrode sets marked with $\star$ are off.

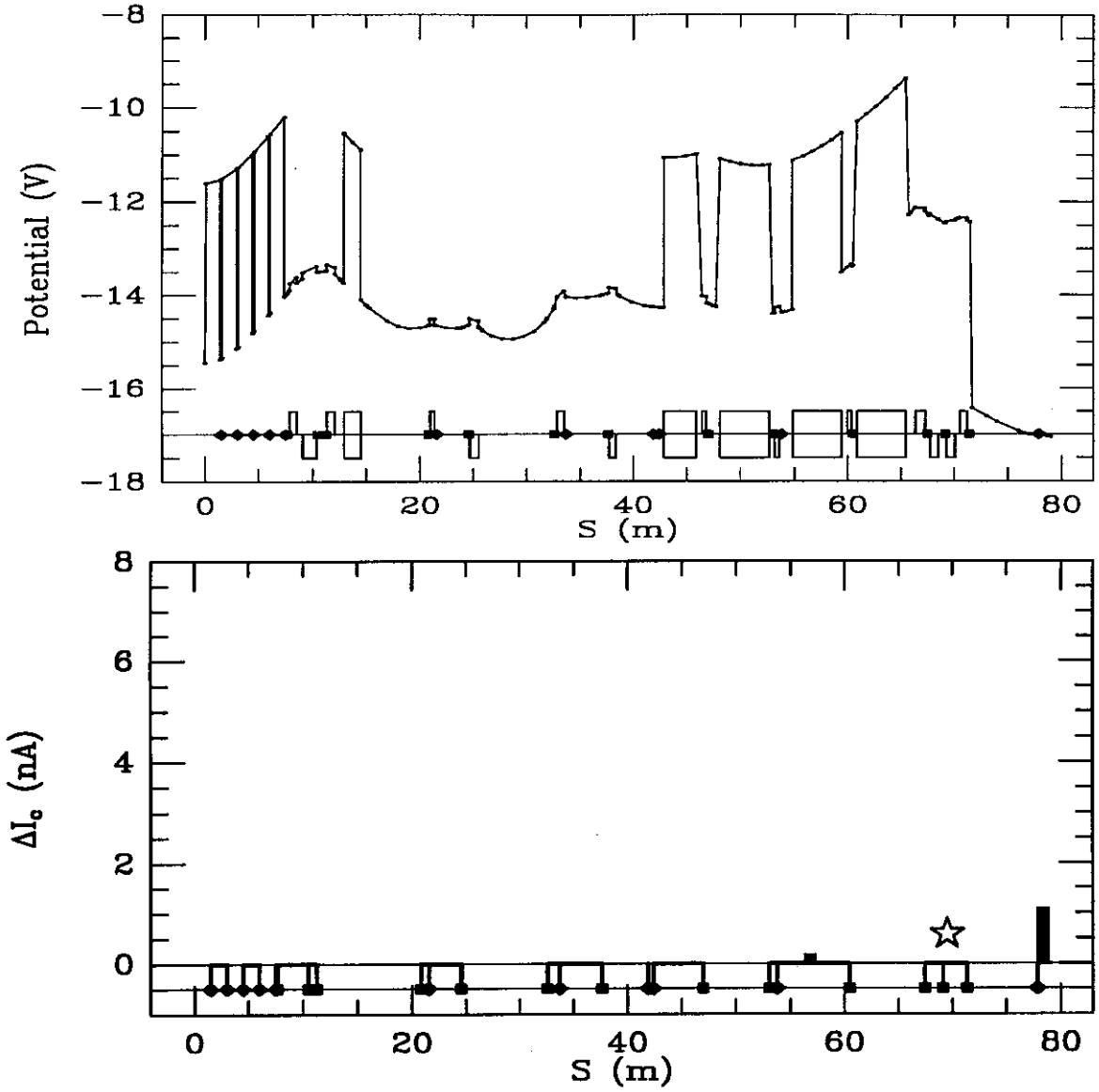

Figure 2.11: Clearing current re-distribution in sector A30 with some electrodes turned off. Electrode sets marked with ⋆ are off.

of the experiments the $h = 2$ system without cycle suppression was used to create partially or completely bunched beams.

2.4.3 Damper System

The accumulator has a damper system that is capable of damping dipole oscillations of the beam[30] in both the horizontal and vertical planes. The coherent oscillation signal of the beam is detected and after signal processing and amplification a corrective field is applied through kickers. The damper is a wide band system with a frequency range of about 150kHz–150MHz. The damper system is needed for beam currents above about $20mA$, so the damper system is left on all the time for normal operation.

The damper pick-ups are very useful in many of the experiments to monitor various modes of beam coherent oscillation. The damper pick-ups can be tapped and the signals are then fed to spectrum analyzers. A range of frequencies may be monitored for the occurrence of any coherent oscillation power, or the power of a specific line of coherent oscillation may be monitored to observe its change with time. When there is no external coherent driving fields in the machine, these coherent lines indicate beam coherent instabilities — a potentially destructive phenomenon which we will discuss in the next chapter.

Chapter 3

Beam Coherent Instabilities

3.1 Introduction

Charged particle beams in accelerators will interact electromagnetically with their environment. The fields generated by the beam are called wake fields. Depending on the characteristics of the surroundings these wake fields will have a variety of properties. In some cases the frequency spectra are concentrated in a few narrow bands like those generated by RF cavities; in other cases the wake fields have very wide frequency spectra like those generated in smooth vacuum chambers. These fields then act back on the beam, perturbing the particle motion. If the beam intensity is large enough and other conditions are met, this interaction may lead to the growth of a coherent oscillation of the beam – a beam coherent instability. If we expand the meaning of wake fields to include the fields due to trapped ions, the impedance also describes the beam-ion interaction. Since there are similarities between the normal beam coherent instabilities, especially the resistive wall instability which will be discussed below, and beam-ion coherent instability, it is necessary and also interesting to take a brief look at both of them and compare. For a more detailed introduction to beam coherent instabilities see [31] and the references therein.

Beam oscillations and instabilities can be categorized as dipole mode, quadrupole

mode, etc. In a dipole mode oscillation, the beam's centroid oscillates, while in a quadrupole mode, the beam's shape oscillates. The most common instabilities are dipole instabilities, so we will concentrate on dipole mode oscillation and instability.

The quantity to describe the wake fields is the wake function W. They are categorized into different orders, denoted by their subscript, 0 for monopole force, 1 for dipole, and so on. It is easy to see that there is no monopole transverse force, so the lowest order of forces seen by a test particle a distance Z behind a beam with a dipole moment D can be written as

$$\begin{aligned} F_\perp &= eD\,W_1^\perp(Z)/L \\ F_\parallel &= eQ\,W_0^\parallel(Z)/L \end{aligned} \tag{3.1}$$

where the superscript $\perp$ stands for transverse direction and $\parallel$ for longitudinal. Q is the beam charge and D its dipole moment. However the longitudinal and transverse wake functions are not independent because electromagnetic fields are governed by Maxwell's equations. The Maxwell's equations dictate the transverse and longitudinal forces to follow[32][31]

$$\nabla_\perp F_\parallel = \frac{\partial}{\partial z}\vec{F}_\perp \tag{3.2}$$

which is referred to as Panofsky-Wenzel theorem. It follows that transverse and longitudinal wake functions of the same order satisfy

$$W_m^\parallel = W_m^{\perp\prime} \tag{3.3}$$

where the prime represents $\frac{\partial}{\partial z}$. So we do not need to identify the direction a wake function refers to and can simply use the transverse wake function without the superscript. Equation 3.1 is then

$$\begin{aligned} F_\perp &= eD\,W_1(Z)/L \\ F_\parallel &= eQ\,W_0'(Z)/L \end{aligned} \tag{3.4}$$

The frequency domain equivalent of the wake functions are impedances. They are very important in beam coherent instability theories. They are defined as

$$\begin{aligned} Z_m^\parallel &= \int_{-\infty}^{\infty} e^{i\omega z/c}\,W_m'(z)\,\frac{dz}{c} \\ Z_m^\perp &= -i\int_{-\infty}^{\infty} e^{i\omega z/c}\,W_m(z)\,\frac{dz}{c} \end{aligned} \tag{3.5}$$

where L is the circumference of the machine.

In the frequency domain Panofsky-Wenzel theorem takes the form

$$Z_m^{\parallel}(\omega) = \frac{\omega}{c} Z_m^{\perp}(\omega) \tag{3.6}$$

Wake fields and impedances as defined here should really be a local concept, each component producing its own electromagnetic field when the beam passes by and making its own contribution to the total impedance of the machine. These wake fields and impedances, as well as the external focusing forces, are not uniformly distributed. However, since we are concerned with a coherent beam instability which usually develops over many turns, the wake fields and impedances are usually referred as the average over the whole machine, and the machine is treated as having a uniform focusing.

The impedance can be either calculated or measured. In a calculation, the impedance of every component and joint must be calculated or estimated in order to get the impedance for the whole machine. Since the vacuum pipe consists of many different pieces with different sizes and shapes, the calculations usually cannot be done analytically, especially for places where vacuum pipe size or shape changes take place. With the development of fast computers and sophisticated electromagnetic field calculation programs, most of the calculation can be done numerically, though it is typically very time and effort consuming. The measurement of impedance can be done either on the work bench for each component just as in the calculation method, or using a beam-based measurement for the whole machine. The calculation and measurement of machine impedance is a special area of study and research in accelerator physics[33][34] [35][36] [37][38]. By introducing wake functions and impedances, however, the details of the beam-environment interaction are separated from the beam instability calculation. We can now assume the machine impedance is known and concentrate on its impact on beam stability.

There are two approaches in describing beam instability. The direct approach deals with the beam response in physical space. The other approach employs Vlasov equations[31][39] and deals with the phase space distribution of the particles. The direct approach provides more physical insight into the problem, but sometimes is

more subtle and can be misleading, especially when non-linearity is involved[40]. The Vlasov approach, on the other hand, is more complicated mathematically, but is otherwise straightforward. Here we will take the Vlasov approach after a brief introduction to the Vlasov equation.

3.2 Brief Introduction to Vlasov Equation

Suppose the phase space density function describing the system is $\Psi(\vec{r},\vec{v},t)$ and it satisfies the Boltzmann equation

$$\frac{\partial\Psi}{\partial t}+\vec{v}\cdot\nabla\Psi+\frac{\vec{F}}{\gamma m}\cdot\frac{\partial\Psi}{\partial\vec{v}}=\left(\frac{\partial\Psi}{\partial t}\right)_c \tag{3.7}$$

where m is particles' mass, $\gamma=\sqrt{1-\beta^2}$, and $(\partial\Psi/\partial t)_c$ is the contribution due to collisions. If collisions can be neglected then we have the Vlasov equation

$$\frac{\partial\Psi}{\partial t}+\vec{v}\cdot\nabla\Psi+\frac{\vec{F}}{\gamma m}\cdot\frac{\partial\Psi}{\partial\vec{v}}=0 \tag{3.8}$$

The natural normalization for Ψ is

$$\int\Psi(\vec{r},\vec{v},t)\,d\vec{r}\,d\vec{v}=N \tag{3.9}$$

where N is the total number of particles. However, in order to see the explicit dependence on the beam intensity we will use the following normalization instead,

$$\int\Psi(\vec{r},\vec{v},t)\,d\vec{r}\,d\vec{v}=1 \tag{3.10}$$

For simplicity we usually consider only one transverse dimension, say y and ignore any coupling for now from the other transverse degree of freedom. However since a particle's momentum affects its transverse motion, the longitudinal dimension must be included. The Vlasov equation then becomes

$$\frac{\partial\Psi}{\partial t}+\dot{\theta}\frac{\partial\Psi}{\partial\theta}+\dot{p}\frac{\partial\Psi}{\partial p}+\dot{y}\frac{\partial\Psi}{\partial y}+\frac{F_y}{\gamma m}\frac{\partial\Psi}{\partial\dot{y}}=0 \tag{3.11}$$

$\dot{\theta}$ is simply the particle's revolution frequency ω_r and p its momentum deviation from that of the synchronous particle. The transverse force F_y is composed of the external focusing force and the wake force, i.e.

$$\frac{F_y}{\gamma m} = -\omega_\beta^2 y + \frac{F_w}{\gamma m} \tag{3.12}$$

where ω_β is the angular frequency of the beam's betatron oscillation. When dealing with transverse motion, the longitudinal wake field is usually ignored and a particle's energy is unchanged, i.e. $\dot{p} = 0$. So the Vlasov equation in our application is

$$\frac{\partial \Psi}{\partial t} + \omega_r \frac{\partial \Psi}{\partial \theta} + \dot{y}\frac{\partial \Psi}{\partial y} + (-\omega_\beta^2 y + \frac{F_w}{\gamma m})\frac{\partial \Psi}{\partial \dot{y}} = 0 \tag{3.13}$$

where θ is the azimuthal angle along the machine, $\theta = s/R$, and ω_r is the angular revolution frequency.

In the following sections the application of the Vlasov equation to the beam coherent instability problem is developed using different beam models. We will start with a simple model where all particles behave like one, and then add non-linear effects to the model. The important concept of Landau damping will be introduced in the process. Finally the effects of ions on the beam coherent instability are discussed.

3.3 Coherent Instability and Landau Damping

With the complexity of the electromagnetic environment embedded in the definition of impedance, the difficulty of studying beam coherent instability is greatly reduced. We will concentrate on the issue of transverse stability here, simply because this has been observed and is a major operational difficulty in the Fermilab accumulator. The analysis of the longitudinal case is very similar.

Recall that in Eq. 1.5, the machine lattice is described as piecewise-constant focusing. Because beam instabilities develop on a time scale much larger than the revolution period, the beam model considered here is simplified as being uniformly focused by an averaged focusing field around the whole machine. Thus the betatron motion of a beam particle becomes simply harmonic oscillation and can be described

by the following equation

$$\frac{d^2y}{dt^2} + \omega_\beta^2\, y = \frac{F_w}{\gamma m} \tag{3.14}$$

where ω_β is the angular betatron frequency. The force in the direction of the oscillation F_w is from the accumulated wake field excited by the beam's previous oscillation, i.e.

$$F_w(z,t) = \frac{e}{L}\int_{-\infty}^{t} \frac{c\,dt'}{L}\, D(z,t')\, W(ct - ct') \tag{3.15}$$

where

$$D(z,t) = \overline{y}(z,t) N e \tag{3.16}$$

is the dipole moment of the beam, N is the total number of beam particles and e their charge. The corresponding Vlasov equation is, see Eq. 3.13,

$$\frac{\partial \Psi}{\partial t} + \dot{y}\frac{\partial \Psi}{\partial y} + (-\omega_\beta^2 y + \frac{F_w}{\gamma m})\frac{\partial \Psi}{\partial \dot{y}} + \omega_r \frac{\partial \Psi}{\partial \theta} = 0 \tag{3.17}$$

There are some very important effects which need to be considered before proceeding further. Beam particles usually have a small spread in their momenta and each particle's revolution frequency, ω_r, depends on its longitudinal momentum through the slip factor. Their betatron frequency, ω_β, will also have a chromatic spread due to the momentum spread. In addition, nonlinearity in the external focusing will also introduce a spread in betatron frequencies. This frequency spread causes a decoherence effect, i.e. without an external sustaining force, the initial coherent motion of the beam will gradually decrease because the frequency spread causes the coherent energy to randomize into incoherent motion. This decrease in the beam's coherent oscillation also reduces the interaction of the beam with its environment and increases the stability of the beam as a whole, as we will see later.

In general, with the presence of nonlinearity, the particles' motion is no longer a harmonic oscillation and the external focusing force is a function of particles' position. But if this nonlinearity is small we can treat it as only changing the frequency of the particles while keeping the motion harmonic, e.g. a particle oscillating under a nonlinear force $F(y)$

$$m\ddot{y} = F(y) \tag{3.18}$$

Taking the above approximation and assuming the solution is

$$x = A\cos(\omega(A)t + \phi_0) \tag{3.19}$$

We insert it into equation 3.18 and multiply both sides with the cos term and average it over one full cycle to obtain

$$-\frac{m}{2}A\omega^2 = \overline{F(A\cos(\omega t + \phi_0)) \cdot \cos(\omega t + \phi_0)} \tag{3.20}$$

The resulting equation will give us the dependence of frequency ω on the amplitude A. For a force of the following form

$$F(y) = \frac{2e^2\lambda}{y}(1 - e^{-\frac{y^2}{2\sigma^2}}) \tag{3.21}$$

this dependence is

$$\omega = \frac{2e}{A\sigma}\sqrt{\frac{\lambda}{m}}\sqrt{1 - e^{-\frac{A^2}{4\sigma^2}}I_0(\frac{A^2}{4\sigma^2})} \tag{3.22}$$

where I_0 denotes the zeroth order modified Bessel function[41]. When the nonlinearity is not small, this approximation simply picks up the dipole component of the motion and ignores the higher order modes of motion. It, however, is still a reasonable approximation if we are only concerned with effects that happen on a time scale much larger than the oscillation period.

We define phase space action-angle coordinates as

$$\begin{aligned} y &= A\cos\phi \\ \dot{y} &= \omega_\beta A\sin\phi \end{aligned} \tag{3.23}$$

The nonlinearity in this approximation means that we have

$$\omega_\beta = \omega_\beta(p, A) \tag{3.24}$$

The phase space area element in the action-angle coordinate is

$$\begin{aligned} dy\, d\dot{y} &= \begin{vmatrix} \frac{\partial y}{\partial A} & \frac{\partial y}{\partial \phi} \\ \frac{\partial \dot{y}}{\partial A} & \frac{\partial \dot{y}}{\partial \phi} \end{vmatrix} dA\, d\phi \\ &= (\omega_\beta A + \frac{\partial \omega_\beta}{\partial A}A^2\sin^2\phi)\, dA\, d\phi \end{aligned} \tag{3.25}$$

On average it is

$$dy\, d\dot{y} = \frac{1}{2} d(\omega_\beta A^2)\, d\phi \tag{3.26}$$

Using the averaged format simplifies the equations to come. It also has some physical meaning. The phase space trajectory of a particle with initial conditions described by Eq. 3.23 has an area of $\pi\omega_\beta A^2$. An angular section of that area increment would be that in Eq. 3.26. The final result is not affected by this approximation.

The phase space distribution function in general will depend on both longitudinal momentum and the transverse coordinates,

$$\Psi = \Psi(A, \phi, p) \tag{3.27}$$

For simplicity we will assume the dependence on momentum can be separated, i.e.

$$\Psi(A, \phi, p) = \Psi(A, \phi)\, g(p) \tag{3.28}$$

with the following normalization condition

$$\begin{aligned} \int \Psi_0\, dy\, d\dot{y} = \pi \int \Psi_0(A)\, d(\omega_\beta A^2) = 1 \\ \int g(p)\, dp = 1 \end{aligned} \tag{3.29}$$

The stability of the beam is studied using the perturbative method. First, consider the stable beam having an equilibrium distribution. Then some small coherent perturbation is added to this equilibrium distribution. If any mode of perturbation grows initially then the beam is considered unstable for that mode of oscillation. If no growth of any perturbation occurs then the beam is stable.

The stationary solution of Eq. 3.17, Ψ_0, satisfies

$$\dot{y}\frac{\partial \Psi_0}{\partial y} - \omega_\beta^2 y \frac{\partial \Psi_0}{\partial \dot{y}} = 0 \tag{3.30}$$

Using the phase space action-angle coordinates equation 3.30 is simply

$$\frac{\partial \Psi_0}{\partial \phi} = 0 \tag{3.31}$$

i.e.

$$\Psi_0 = \Psi_0(A) \cdot g(p) \tag{3.32}$$

On top of the equilibrium distribution, we introduce a small coherent perturbation to the beam distribution

$$\Psi = \Psi_0 + \Psi_1 e^{i(n\theta - \Omega t)} \tag{3.33}$$

This perturbation will cause the beam center to have an oscillation

$$\overline{y} = Y e^{i(n\theta - \Omega t)} \tag{3.34}$$

where the amplitude Y is

$$\begin{aligned} Y &= \int \Psi \cdot y \, dy \, d\dot{y} \, dp \, e^{-i(n\theta - \Omega t)} \\ &= \frac{1}{2\pi} \int \Psi_1 A \cos\phi \, d(\omega_\beta A^2) \, d\phi \, dp \end{aligned} \tag{3.35}$$

The corresponding wake force, following equation 3.15 and 3.5 is

$$F_w = i \frac{Ne^2 Z(\Omega)}{T_0 L} Y e^{i(n\theta - \Omega t)} \tag{3.36}$$

Since we are studying the stability of these perturbations, we can assume the perturbation is very small and consequently keep only the lowest order terms in Ψ_1. We thus have the linearized Vlasov equation:

$$-i(\Omega - n\omega_r)\Psi_1 - \omega_\beta \frac{\partial \Psi_1}{\partial \phi} + i \frac{Ne^2 Z(\Omega)}{\gamma m T_0 L} \frac{\partial \Psi_0}{\partial \dot{y}} Y = 0 \tag{3.37}$$

From Eq. 3.32 we have

$$\frac{\partial \Psi_0}{\partial \dot{y}} = \frac{d\Psi_0}{dA} \frac{2A \sin\phi}{\partial(\omega_\beta A^2)/\partial A}. \tag{3.38}$$

Equation 3.37 becomes

$$-i(\Omega - n\omega_r)\Psi_1 - \omega_\beta \frac{\partial \Psi_1}{\partial \phi} + i \frac{Ne^2 Z(\Omega) \Psi_0'(A)}{\gamma m T_0 L} \frac{2A \sin\phi}{\partial(\omega_\beta A^2)/\partial A} Y = 0 \tag{3.39}$$

Since Ψ_1 is periodic in ϕ we can do a Fourier series expansion in ϕ.

$$\Psi_1(A, \phi) = \sum_l R_l(A) e^{il\phi} \tag{3.40}$$

The beam dipole oscillation amplitude is

$$Y = \frac{1}{2} \int (R_1 + R_{-1}) A \, d(\omega_\beta A^2) \, dp \tag{3.41}$$

and equation 3.39 becomes

$$-i(\Omega - n\omega_r + l\omega_\beta)R_l + i\frac{Ne^2Z(\Omega)\Psi_0'(A)}{\gamma mT_0L}(\delta_{l,1} - \delta_{l,-1})\frac{A\omega_\beta}{\partial(\omega_\beta A^2)/\partial A}Y = 0 \quad (3.42)$$

It can be seen from the equation above that R_1 and R_{-1} are the only relevant terms since we are only concerned with the dipole motion of the beam. The equation can then be further written as

$$R_1 + R_{-1} = i\frac{Ne^2Z(\Omega)}{\gamma mT_0L}\frac{\Psi_0'(A)}{(\Omega - n\omega_r)^2 - \omega_\beta^2}Y \quad (3.43)$$

and with Eq. 3.41, it gives us the dispersion relation

$$1 = i\frac{Ne^2Z(\Omega)}{\gamma mT_0L}\int\frac{\Psi_0'(A)g(p)\omega_\beta A^2\,dA\,dp}{(\Omega - n\omega_r)^2 - \omega_\beta^2} \quad (3.44)$$

Equation 3.44 gives the correspondence between beam coherent oscillation frequencies and beam and machine conditions. When the imaginary part of that frequency becomes positive, the corresponding oscillation is unstable.

First let us apply equation 3.44 to the simplest case where all particles behave like one, i.e. a rigid beam, and there is no non-linearity in the external focusing. In this case frequencies ω_r, ω_β are fixed. Using the normalization condition Eq. 3.29, Eq. 3.44 simplifies to

$$(\Omega - n\omega_r)^2 - \omega_\beta^2 = -i\frac{Ne^2Z(\Omega)}{\gamma mT_0L} \quad (3.45)$$

When the beam intensity is small we have

$$|n\omega_0 - \Omega| \approx \omega_\beta \quad (3.46)$$

or

$$\Omega \approx n\omega_0 \pm \omega_\beta = (n \pm Q)\omega_r \quad (3.47)$$

where $Q = \omega_\beta/\omega_0$ is the tune of betatron motion. These are simply the betatron sideband frequencies and they are called "fast-wave" and "slow-wave" respectively.

Using the approximation above for Ω on the right hand side of Eq. 3.45 gives us the first order growth rate

$$Im\,\Omega = \mp\frac{Ne^2}{\omega_\beta\gamma mT_0L}Re\,Z[(n \pm Q)\omega_0] \quad (3.48)$$

The top sign is for the fast-wave where $\Omega \approx n\omega_r + \omega_\beta$ and the lower one for the slow-wave where $\Omega \approx n\omega_r - \omega_\beta$ and this convention will be followed throughout this section.

In the Fermilab accumulator, the resistive wall impedance dominates at the low frequencies[42]. The resistive wall impedance is due to the finite beam pipe wall conductivity. For a simple case of a circular pipe of radius b and conductivity σ_c this impedance is[31]

$$\frac{Z(\omega)}{L} = \sqrt{\frac{2}{\pi\sigma_c}}\frac{1}{b^3\sqrt{|\omega|}}(1-i) \tag{3.49}$$

The growth rate of fast-wave and slow-wave oscillation corresponding to this resistive wall impedance is thus

$$\frac{1}{\tau} = \mp\sqrt{\frac{2}{\pi\sigma}}\frac{Ne^2}{\gamma m\omega_\beta T_0}\frac{1}{b^3\sqrt{(n\pm Q)\omega_0}} \tag{3.50}$$

Since real machines have naturally positive real impedances, it follows that with this rigid beam model, the fast-wave is always stable and the slow-wave is always unstable.

In real machines we have to include the non-linearities and momentum spreads. Usually the frequency spread caused by the betatron amplitude and momentum spreads is small compared to beam revolution frequency and low order betatron sidebands are far from overlapping, so we can safely assume that at most one pole in the denominator in Eq. 3.44 contributes at one time, i.e.

$$\begin{aligned}
&\int \frac{\Psi_0'(A)g(p)\omega_\beta A^2\,dA\,dp}{(\Omega - n\omega_r)^2 - \omega_\beta^2} \\
&= \frac{1}{2}\int \Psi_0'(A)g(p)A^2\left[\frac{1}{\Omega - n\omega_r - \omega_\beta} - \frac{1}{\Omega - n\omega_r + \omega_\beta}\right]dA\,dp \\
&\cong -\frac{1}{2}\int \frac{\Psi_0'(A)g(p)A^2\,dA\,dp}{\omega_\beta \pm (n\omega_r - \Omega)}
\end{aligned} \tag{3.51}$$

Now let us assume that there is one dominating source causing the betatron frequency ω_β spread and this source is momentum spread. Momentum deviation causes spreads in both the particles' revolution frequency and the betatron oscillation frequency:

$$\omega_r = \omega_0 + \eta\omega_0 p \tag{3.52}$$

$$\omega_\beta = \omega_{\beta 0} + (\xi + Q\eta)\omega_0 p \tag{3.53}$$

where p is the particle's momentum deviation from the nominal momentum.

With these assumptions and approximations, Eq. 3.44 simplifies to

$$1 = i\frac{Ne^2 Z(\Omega)}{2\gamma m T_0 L}\frac{1}{\alpha\omega_0\omega_{\beta 0}}\int\frac{g(p)dp}{p \mp p_\Omega} \tag{3.54}$$

where $\alpha = \xi \pm (n \pm Q)\eta$, and p_Ω is the momentum deviation corresponding to Ω, i.e.

$$p_\Omega = \frac{\Omega - (n \pm Q)\omega_0}{\alpha\omega_0}. \tag{3.55}$$

To search for the stability boundary of the system we rewrite the dispersion equation 3.54 and replace $Z(\Omega)$ with $U(\Omega) + iV(\Omega)$, thus turning it into a equation for the curve describing the boundary in the $U + iV$ impedance plane.

$$U(\Omega) + iV(\Omega) = i\frac{2\gamma m T_0 L\alpha\omega_0\omega_{\beta 0}}{Ne^2}\left[\int\frac{g(p)dp}{p \mp p_\Omega}\right]^{-1} \tag{3.56}$$

The integration in the above equation has an real and imaginary part, but mathematically the imaginary part has an ambiguous sign:

$$\int_{-\infty}^{\infty}\frac{\rho(p)\,dp}{p - p_\Omega} = PV\int_{-\infty}^{\infty}\frac{\rho(p)\,dp}{p - p_\Omega} \pm i\pi\rho(p_\Omega) \tag{3.57}$$

where PV stands for Cauchy principal value,

$$PV\int_{-\infty}^{\infty}\frac{\rho(p)\,dp}{p \mp p_\Omega} = \int_0^{\infty} dp\,\frac{\rho(p \pm p_\Omega) - \rho(\pm p_\Omega - p)}{p} \tag{3.58}$$

The ambiguity arises from the two possible integration paths near the pole at $p = p_\Omega$: either above or below it. The ambiguity can be resolved with a more careful mathematical treatment and physical arguments[43], but since we are searching the threshold where the motion becomes unstable, we can imagine the oscillation has an infinitely small growth rate, i.e. $\Omega \to \Omega + i\epsilon$, and thus remove the ambiguity and find the stability boundary. For this purpose

$$\int_{-\infty}^{\infty}\frac{\rho(p)\,dp}{p \mp p_\Omega} = PV\int_{-\infty}^{\infty}\frac{\rho(p)\,dp}{p \mp p_\Omega} \pm i\pi\rho(p_\Omega) \tag{3.59}$$

$$U(\Omega) + iV(\Omega) = \frac{2\gamma mL}{Ne^2} \frac{\omega_{\beta 0} \cdot [\xi \pm (n \pm Q)\eta]}{\mp \pi \rho(p_\Omega) + iPV \int_{-\infty}^{\infty} \frac{\rho(p)\, dp}{p - p_\Omega}} \tag{3.60}$$

For convenience and nevertheless being close to reality we use a Gaussian momentum distribution which is close to what is measured in the accumulator, see Sec. 2.4.1. We have thus

$$\rho(p) = \frac{1}{\sqrt{2\pi}\sigma_p} \exp(-\frac{p^2}{2\sigma_p^2}) \tag{3.61}$$

and the integration can be carried out

$$\int_{-\infty}^{\infty} \frac{\rho(p)\, dp}{p \mp p_\Omega} = \pm i \sqrt{\frac{\pi}{2}} \frac{1}{\sigma_p} W(\frac{p_\Omega}{\sqrt{2}\sigma_p}) \tag{3.62}$$

where W is the complex error function defined as

$$W(z) = e^{-z^2} [1 + \mathrm{erf}(iz)] \tag{3.63}$$

The stable oscillation boundary on the impedance plane for a beam with Gaussian momentum distribution is, finally

$$U(\Omega) + iV(\Omega) = \mp \frac{8\pi\sqrt{2\pi}\gamma mc}{Ne^2} \frac{Q[\xi \pm (n \pm Q)\eta]\sigma_p}{W(p_\Omega/\sqrt{2}\sigma_p)} \tag{3.64}$$

For a typical set of accumulator operation parameters, beam current $I = 100mA$, transverse beam emittance $\epsilon_h = \epsilon_v = 1\pi mm \cdot mrad$, rms momentum spread $\sigma_p = 2.6MeVc$, and chromaticity $\xi_x = \xi_y = 0.3$, the horizontal stability diagram for $(2 - q_x)\omega_0$ frequency is shown in Fig. 3.1. The region to the right of the imaginary axis and to the left of plotted boundary is the stable area. If the impedance of the machine $Z(\omega)$ is within the area, then the oscillation will be stable. If $Z(\omega)$ is outside the area for some frequencies, then it will cause an instability at some frequency and some means such as active damping will have to be used to stabilize the beam motion.

In real machines real part of the impedance is always positive, so the fast-wave modes are always stable. Without any frequency spreads, the rigid beam case, the slow-wave modes are always unstable. This can be seen by using a *delta*-function for $g(p)$ and $\Psi_0(A)$ in Eq. 3.51 and solve for Ω in Eq. 3.44 with a positive real part in the impedance. With frequency spreads, a slow-wave mode is not always unstable. When its frequency lies within the range of individual particles' resonant frequency

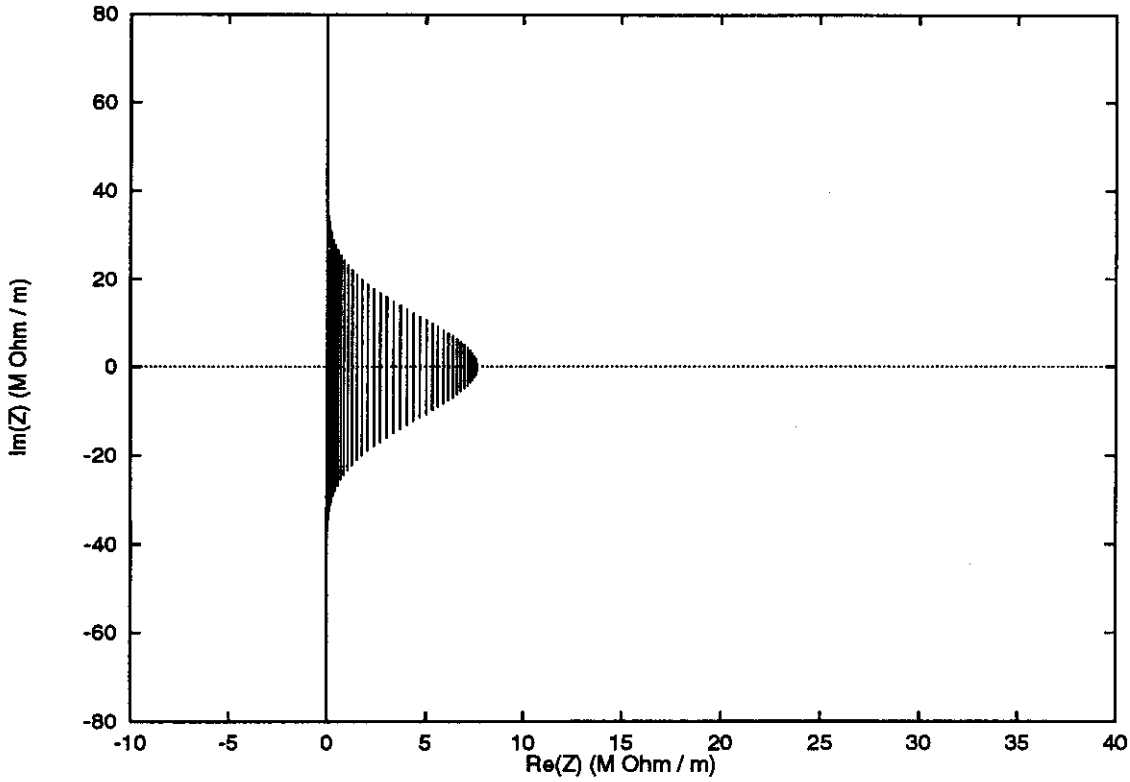

Figure 3.1: Horizontal Beam Stability Diagram. Parameters used are $I = 100mA, \epsilon = 1\pi\, mm \cdot mrad, \xi = 0.3$. Shaded region is the stable area.

spectrum, $\mathrm{Re}W(p_w/\sqrt{2}\sigma_p) \neq 0$, some of the perturbations that are unstable for a rigid beam may now be stable for a beam with frequency spread. It is because the coherent oscillation energy, which otherwise would act back on the beam and increase the oscillation, is continuously absorbed by those resonant beam particles and turned into incoherent oscillation energy thus preventing the coherent motion from growing. This effect is called Landau damping[43]. If, however, the frequency is outside the spectrum or the machine impedance is too big, the oscillation will still be unstable.

If we go back to equation 3.60 and 3.51, we can see that the source of Landau damping comes from the spread in the oscillation frequencies of the beam particles. The bigger the spread, the more damping there is. In the approximation we made earlier that the transverse oscillation frequency spread of the particles are dominated by their momentum spread, the damping is directly connected to the momentum spread of the beam. The beam's coherent energy is gradually converted to the incoherent oscillations of near resonant particles, and will continue until those particles are lost due to their large amplitudes and no longer contribute to the energy absorbing process. Landau damping as a result will be reduced as those particles are gradually lost. In the other extreme, the non-linearity of the focusing magnetic field dominates this frequency spread, the damping is proportional to the derivative of the frequency distribution[40]. Landau damping ceases to exist as particles redistribute themselves, driven by the coherent energy, to the final state of flat local frequency distribution.

3.4 The Effect of Trapped Ions

Trapped ions oscillate in the electric field of the beam. They unavoidably exert forces back on the beam. A part of the beam disturbs the motion of the ions which in turn interact with trailing beam particles. This presents another mechanism for the beam to coherently interact with itself, just as the way beam interacts with the beam pipe, RF cavity, etc. We expect, therefore, similar effects from the ions as we have seen in the last section from machine impedance sources, and we will follow a parallel path in the analysis.

Quantities related to the beam will have a subscript b while those related to ions

will have a subscript i. Vlasov equations for the transverse motion of the beam and ions are

$$\begin{aligned} \frac{\partial \Psi_b}{\partial t} + \dot{y}_b \frac{\partial \Psi_b}{\partial y_b} + \frac{F_b}{\gamma m_b} \frac{\partial \Psi_b}{\partial \dot{y}_b} + \omega_r \frac{\partial \Psi_b}{\partial \theta} &= 0 \\ \frac{\partial \Psi_i}{\partial t} + \dot{y}_i \frac{\partial \Psi_i}{\partial y_i} + \frac{F_i}{m_i} \frac{\partial \Psi_i}{\partial \dot{y}_i} &= 0 \end{aligned} \tag{3.65}$$

The forces are a little more complicated than before

$$\begin{aligned} \frac{F_b}{\gamma m_b} &= -\omega_\beta^2 y_b - \omega_{bi}^2 \cdot (y_b - \overline{y_i}) + F_w \\ \frac{F_i}{m_i} &= -\omega_{ib}^2 \cdot (y_i - \overline{y_b}) \end{aligned} \tag{3.66}$$

where ω_{bi} is the angular bounce frequency of the beam in the field of trapped ions, and ω_{ib} that of the ions in the field of beam. Both frequencies are functions of oscillation amplitudes in the averaged approximation. m_b, m_i are the masses of beam particles and ions respectively. F_w is the wake force generated by the beam as seen in the previous section. We have neglected the self-force of the beam and ions on themselves. This is reasonable because neutralization levels are usually small and the ions' self-force to beam-ion force is of the same ratio; moreover the beam self-force is greatly suppressed by the relativistic effect (factor of $1/\gamma^2$). Let

$$\omega_b^2 = \omega_\beta^2 + \omega_{bi}^2 \tag{3.67}$$

$$\omega_i^2 = \omega_{ib}^2 \tag{3.68}$$

those forces can be written as

$$\begin{aligned} F_b/\gamma m_b &= -\omega_b^2\, y_b + \omega_{bi}^2\, \overline{y_i} + F_w \\ F_i/m_i &= -\omega_i^2\, y_i + \omega_{ib}^2\, \overline{y_b} \end{aligned} \tag{3.69}$$

For the equilibrium solutions, no coherent oscillations are present and therefore $\overline{y_b} = \overline{y_i} = 0$, and $F_w = 0$. Following the previous section we define

$$\begin{aligned} y_b &= A_b \cos\phi_b & \qquad y_i &= A_i \cos\phi_i \\ \dot{y}_b &= \omega_b A_b \sin\phi_b & \qquad \dot{y}_i &= \omega_i A_i \sin\phi_i \end{aligned}$$

We will have, on average,

$$\begin{aligned} dy_b\, d\dot{y}_b &= \frac{1}{2} d(\omega_b A_b^2) d\phi_b \\ dy_i\, d\dot{y}_i &= \frac{1}{2} d(\omega_i A_i^2) d\phi_i \end{aligned} \tag{3.70}$$

And equilibrium solutions will not depend on phase space angle ϕ,

$$\begin{aligned} \Psi_{b0} &= \Psi_{b0}(A_b)\, g(p) \\ \Psi_{i0} &= \Psi_{i0}(A_i) \end{aligned} \tag{3.71}$$

Strictly speaking, ω_b, ω_{ib} and Ψ_{i0} are all functions of longitudinal position, i.e. θ, because beam size, therefore beam and ion bounce frequencies, varies around the machine and the ions are not uniformly distributed. We have ignored their dependence on the azimuthal angle θ for the same reason that we have used a uniform machine model, see section 3.1.

Assuming small perturbations, we have

$$\begin{aligned} \Psi_b &= \Psi_{b0} + \Psi_{b1} e^{i(n\theta - \Omega t)} \\ \Psi_i &= \Psi_{i0} + \Psi_{i1} e^{i(n\theta - \Omega t)} \end{aligned} \tag{3.72}$$

We also have

$$\begin{aligned} \overline{y_b} &= Y_b\, e^{i(n\theta - \Omega t)} \\ \overline{y_i} &= Y_i\, e^{i(n\theta - \Omega t)} \end{aligned} \tag{3.73}$$

where we have defined the amplitudes as

$$\begin{aligned} Y_b &\equiv \frac{1}{2\pi} \int \Psi_{b1}\, A_b \cos\phi_b\, d(\omega_b A_b^2)\, d\phi_b\, dp \\ Y_i &\equiv \frac{1}{2\pi} \int \Psi_{i1}\, A_i \cos\phi_i\, d(\omega_i A_i^2)\, d\phi_i \end{aligned} \tag{3.74}$$

The wake force is then

$$F_w = i \frac{Ne^2}{T_0 L} Z(\Omega) Y_b e^{i(n\theta - \Omega t)} \tag{3.75}$$

The linearized Vlasov equations are

$$\begin{aligned} -i(\Omega - n\omega_r)\Psi_{b1} - \omega_b \frac{\partial \Psi_{b1}}{\partial \phi_b} + (i \frac{Ne^2}{\gamma m_b T_0 L} Z(\Omega) Y_b + \omega_{bi}^2 Y_i) \frac{\partial \Psi_{b0}}{\partial \dot{y}_b} &= 0 \\ -i\Omega\Psi_{i1} - \omega_i \frac{\partial \Psi_{i1}}{\partial \phi_i} + \omega_{ib}^2 Y_b \frac{\partial \Psi_{i0}}{\partial \dot{y}_i} &= 0 \end{aligned} \tag{3.76}$$

With the Fourier series expansion

$$\begin{aligned}\Psi_{b1} &= \sum_l R_{bl} e^{il\phi_b} \\ \Psi_{i1} &= \sum_l R_{il} e^{il\phi_i}\end{aligned} \tag{3.77}$$

dipole coherent oscillation amplitudes are

$$\begin{aligned}Y_b &= \frac{1}{2}\int (R_{b1} + R_{b-1}) A_b \, d(\omega_b A_b^2)\, dp \\ Y_i &= \frac{1}{2}\int (R_{i1} + R_{i-1}) A_i \, d(\omega_i A_i^2)\end{aligned} \tag{3.78}$$

Following straightforward steps, equation 3.76 evolves to

$$\begin{aligned}Y_b &= i\frac{Ne^2 Z(\Omega)}{\gamma m_b T_0 L} Y_b \cdot \int \frac{\Psi'_{b0}(A_b) g(p) \omega_b A_b^2 \, dA_b \, dp}{(\Omega - n\omega_r)^2 - \omega_b^2} + Y_i \cdot \int \frac{\Psi'_{b0}(A_b) \omega_{bi}^2 \omega_b A_b^2 \, dA_b \, dp}{(\Omega - n\omega_r)^2 - \omega_b^2} \\ Y_i &= Y_b \cdot \int \frac{\Psi'_{i0}(A_i) \omega_{ib}^2 \omega_i A_i^2 \, dA_i}{\Omega^2 - \omega_i^2}\end{aligned} \tag{3.79}$$

Finally we have the dispersion equation including the effect of trapped ions

$$\begin{aligned}1 &= i\frac{Ne^2 Z(\Omega)}{\gamma m_b T_0 L} \cdot \int \frac{\Psi'_{b0}(A_b) g(p) \omega_b A_b^2 \, dA_b \, dp}{(\Omega - n\omega_r)^2 - \omega_b^2} \\ &\quad + \int \frac{\Psi'_{b0}(A_b) \omega_{bi}^2 \omega_b A_b^2 \, dA_b \, dp}{(\Omega - n\omega_r)^2 - \omega_b^2} \cdot \int \frac{\Psi'_{i0}(A_i) \omega_{ib}^2 \omega_i A_i^2 \, dA_i}{\Omega^2 - \omega_i^2}\end{aligned} \tag{3.80}$$

In general ω_{bi}^2 is a function of A_b and therefore cannot be pulled out of the integration, but if it is only a weak function of A_b, or if ω_r and ω_b are not dependent on A_b, which is almost true, then ω_{bi}^2, or another quantity of the same order, can be taken out as a constant. This constant, let us call it ω_c^2, measures the average coupling strength from ions to the beam. In the limit that ω_r and ω_b do not depend on A_b, ω_c is simply the rms bounce frequency of the beam inside the ion cloud. In this approximation the dispersion equation is

$$1 = i\frac{Ne^2}{\gamma m_b T_0 L} \int \frac{g(p)\, dp}{(\Omega - n\omega_r)^2 - \omega_b^2} \cdot [Z(\Omega) + Z_i(\Omega)] \tag{3.81}$$

where

$$Z_i(\Omega) = -i\frac{\gamma m_b T_0 L \omega_c^2}{Ne^2} \cdot \int \frac{\Psi'_{i0}(A_i) \omega_{ib}^2 \omega_i A_i^2 \, dA_i}{\Omega^2 - \omega_i^2} \tag{3.82}$$

The quantity $\gamma m T_0 L \omega_c^2 / N e^2$ in Z_i is independent of the beam intensity and is proportional to the machine neutralization level. In the case above, if we take the simple-minded picture that the beam and ion cloud share the same bi-Gaussian transverse distribution then

$$\omega_c^2 = \frac{\eta N e^2}{L \gamma m_b} \frac{1}{\sigma_y(\sigma_x + \sigma_y)} \tag{3.83}$$

and hence

$$Z_i(\Omega) = -i \frac{T_0}{\sigma_y(\sigma_x + \sigma_y)} \cdot \int \frac{\Psi'_{i0}(A_i) \omega_{ib}^2 \omega_i A_i^2 \, dA_i}{\Omega^2 - \omega_i^2} \tag{3.84}$$

As we expected, the main effect of trapped ions comes in the form of some extra impedance in the machine. This is the Z_i term in equation 3.81. If the stability boundary discussed in the previous section leaves an impedance budget, then this "ion impedance" may take away this budget and cause a beam instability. The other contribution of the ions is to shift the beam oscillation frequency, which is contained in the term $\omega_b^2 = \omega_\beta^2 + \omega_{bi}^2$. This shift, however, is usually very small and can barely be measured with an adequate clearing electrode system and therefore can be ignored most of the time.

If we take the same limit as in the last section, i.e. the beam frequency spreads are dominated by a Gaussian momentum distribution, the stable beam oscillation boundary on the impedance plane is

$$U(\Omega) + iV(\Omega) = \mp \frac{8\pi\sqrt{2\pi}\gamma m_b c}{N e^2} \frac{Q[\xi \pm (n \pm Q)\eta]\sigma_p}{W(p_n/\sqrt{2}\sigma_p)} - Z_i(\Omega) \tag{3.85}$$

It is, however, much more difficult to get the details about the ion impedance Z_i, because it depends on the neutralization profile, ion amplitude distribution, etc. None of these is known in detail. Instead, we want to try to get a rough estimation of Z_i and if possible a qualitative picture of the effect. For a start, we assume trapped ions have the same transverse distribution as the beam, and again take this distribution as Gaussian. Since this is the average around the machine, we may further simplify it as a round Gaussian with an rms size that is the machine average. The bounce frequency dependence on the amplitude for an ion in a Gaussian beam was already given in equation 3.22. The function, $\Psi(A)$, and the true density distribution in oscillation amplitude, $D(A)$ are shown in Fig. 3.2. Also shown in Fig. 3.2 are the same function

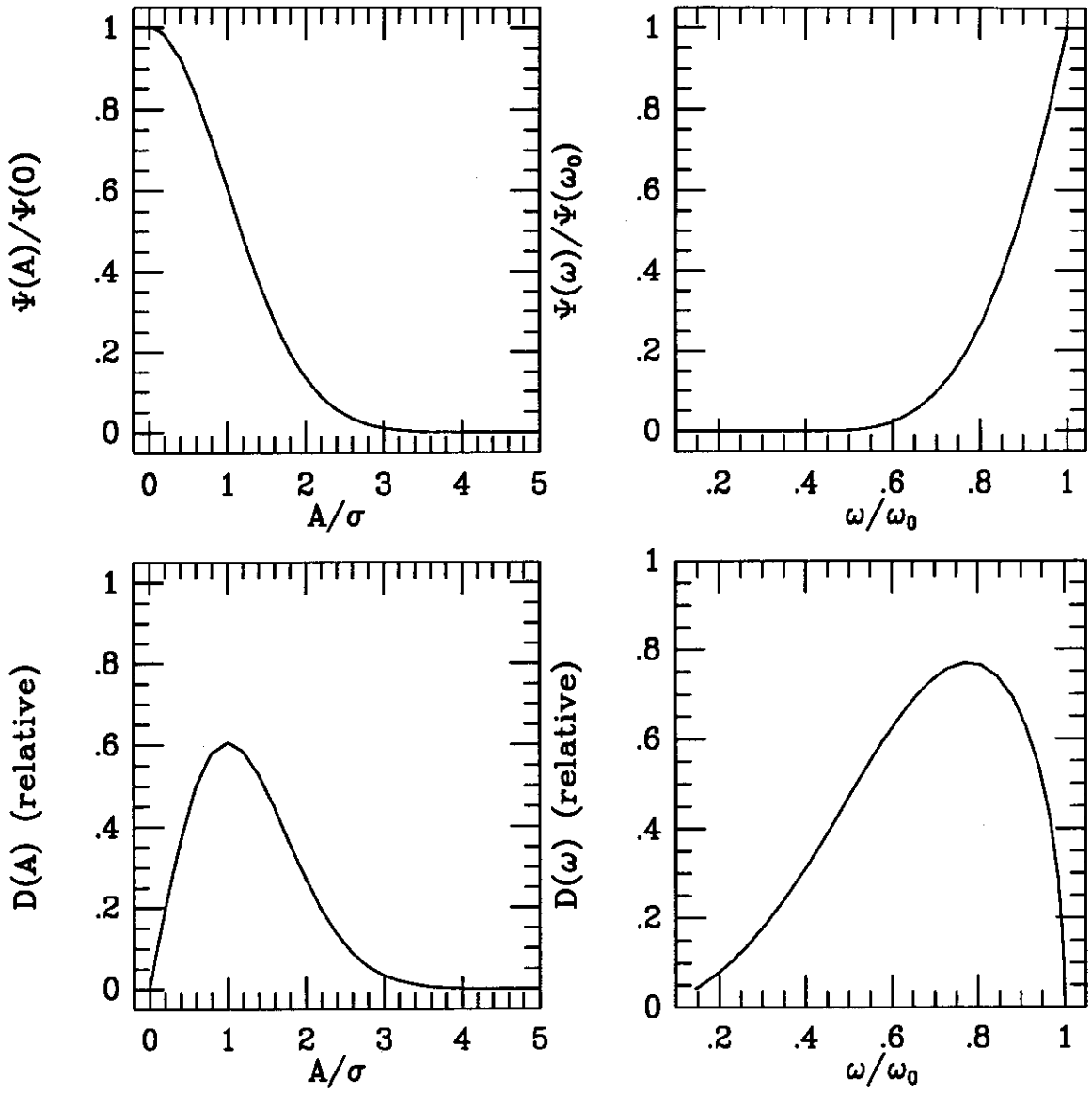

Figure 3.2: Various distribution functions for a round Gaussian ion distribution

plotted as a function of ion bounce frequency, i.e. $\Psi(\omega)$, and the density distribution of the frequency. For this purpose, with the normalization condition and $\omega_{bi} = \omega_i$, we can rewrite the ion impedance as

$$Z_i(\Omega) = -i\frac{T_0}{\sigma_y(\sigma_x+\sigma_y)} \cdot \left\{1 + \frac{\Omega}{2}\int \Psi'_{i0}(\omega_i)\omega_i A_i^2(\omega_i) \cdot [\frac{1}{\omega_i - \Omega} - \frac{1}{\omega_i + \Omega}]\, d\omega_i\right\} \quad (3.86)$$

Around the stability boundary we have

$$\int \frac{\Psi'_{i0}(\omega_i)\omega_i A_i^2(\omega_i)\, d\omega_i}{\omega_i \mp \Omega} = PV \int \frac{\Psi'_{i0}(\omega_i)\omega_i A_i^2(\omega_i)\, d\omega_i}{\omega_i \mp \Omega} \pm i\pi\Psi'_{i0}(\Omega)\Omega A_i^2(\Omega) \quad (3.87)$$

Since $\Psi'_{i0}(\Omega)\Omega A_i^2(\Omega)$ is a even function, together with equation 3.58 we have

$$Z_i(\Omega) = \frac{T_0}{\sigma_y(\sigma_x+\sigma_y)} \cdot \left\{\pi\Psi'_{i0}(\Omega)\Omega^2 A_i^2(\Omega) - i\Omega PV \int \frac{\Psi'_{i0}(\omega_i)\omega_i A_i^2(\omega_i)\, d\omega_i}{\omega_i - \Omega} - i\right\} \quad (3.88)$$

The single sign of the ion-impedance term means trapped ions will damp one of the two waves, slow wave or fast wave, and anti-damp the other, depending on its distribution. Usually, more ions are distributed in the small amplitude, high oscillation frequency region, and the distribution tapers off toward large amplitudes, see Fig. 3.2. Consequently we usually have a plus sign of $\Psi'_{i0}(\Omega)$ and thus positive "ion resistance". This will damp the fast wave and anti-damp the slow wave which is also anti-damped by the normal machine impedance, i.e. the positive U_i reduces the precious stable area for machine impedance. For illustration let us take this simplified model of trapped ions described above and put in the same set of parameters used to produce Fig. 3.1 in section 3.3. The stability diagram with 1% neutralization is shown in Fig. 3.3. Since this is to be compared with the case where no trapped ions are included, the same diagram in Fig. 3.1 is also plotted. As the stable area on the diagram is between the right size of the imaginary axis and the left side of the boundary, we can see from Fig. 3.3 that the stable area when there is no ion trapping has vanished because of this 1% trapped ions. It demonstrates that it does not take a high level of ion neutralization to destabilize an otherwise stable situation.

We have to point out first of all that the theory inevitably overestimates the effect of ions by ignoring the longitudinal motion of ions. The longitudinal motion causes ions to lose the coherent phase information so even when they have the resonant

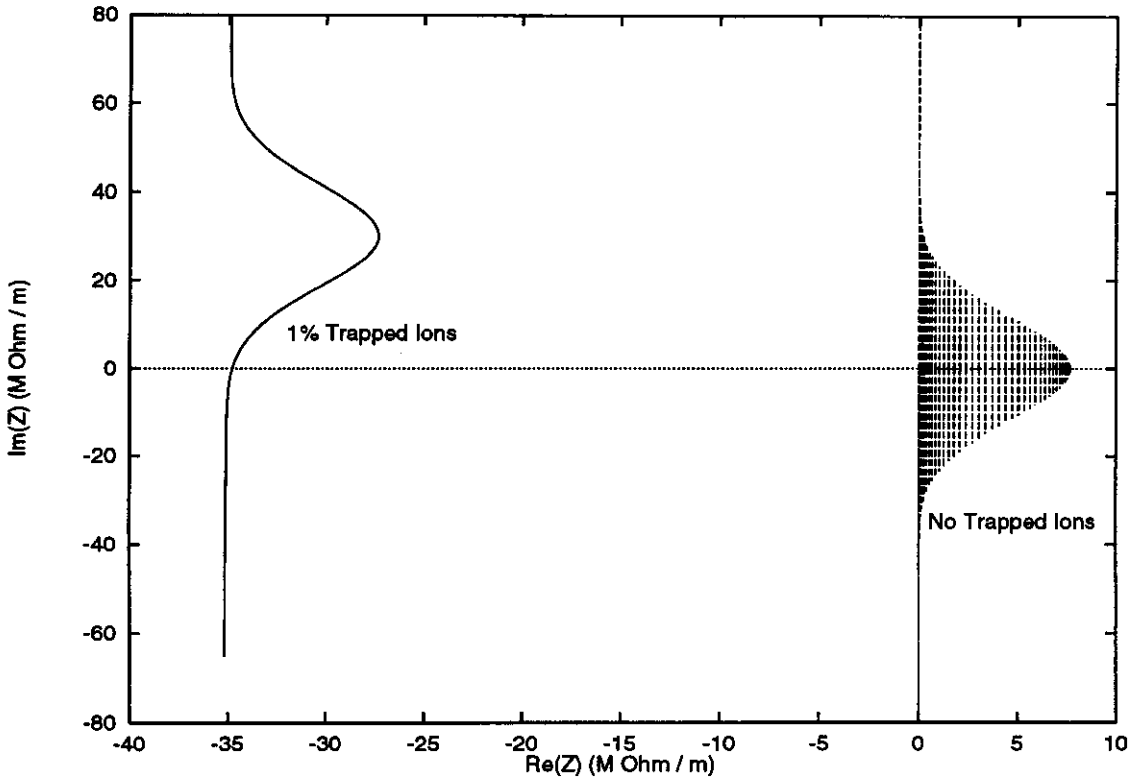

Figure 3.3: Horizontal beam stability diagram with 1% neutralization. Parameters used: $I = 100mA, \epsilon = 1\pi\, mm \cdot mrad, \xi = 0.3$.

frequency, they may not stay resonant. However, to include this effect quantitatively is extremely difficult because it is dependent on the detailed knowledge of ions' distribution and their longitudinal flow. Secondly, this is only a perturbative treatment and not a self consistent one. We started with an equilibrium distribution and evaluate the stability of any small perturbation, but the unstable motions may change the "equilibrium" distribution and alter the assumption on which we have based our theory. To develop a fully self-consistent theory is very difficult. However, we can imagine an iterative process where the theory together with some physical arguments form a closed loop and we can at least get a qualitative explanation of what we have observed, which we will carry out in the following sections.

3.5 Observation in the Accumulator

Before the clearing electrode system upgrade was made, transverse beam coherent oscillations were routinely observed with coherent pickups, observable with 10-20 mA of beam or more. An example is shown in Fig. 3.4. Most of the time we see the oscillations near the $(1-q)$ and $(2-q)$ betatron sideband frequencies and sometimes the $(3-q)$ frequency when the transverse beam emittances are small. This is consistent with the spectrum of ion bounce frequencies. These oscillations can be stable for a very long time without disastrous effects, especially during antiproton stacking when the beam transverse emittances and momentum spread are large. Before antiproton transfer from the accumulator to the Main Ring, the beam is cooled down by the stochastic cooling systems both longitudinally and transversely, see Fig. 3.5. Because of the reduction in beam momentum spread Landau damping is reduced and beam may become unstable. The beam transverse emittances may experience a sudden increase as a consequence. Most of the time, emittance blowups cause no beam loss, but beam loss sometimes does happen as a consequence of the instability, see Fig. 3.5.

Experiments have been done with the added capability of varying the clearing voltage of the new clearing electrode system to determine the effect of trapped ions on the beam coherent oscillation. In Fig. 3.6 the beam coherent oscillation strengths are

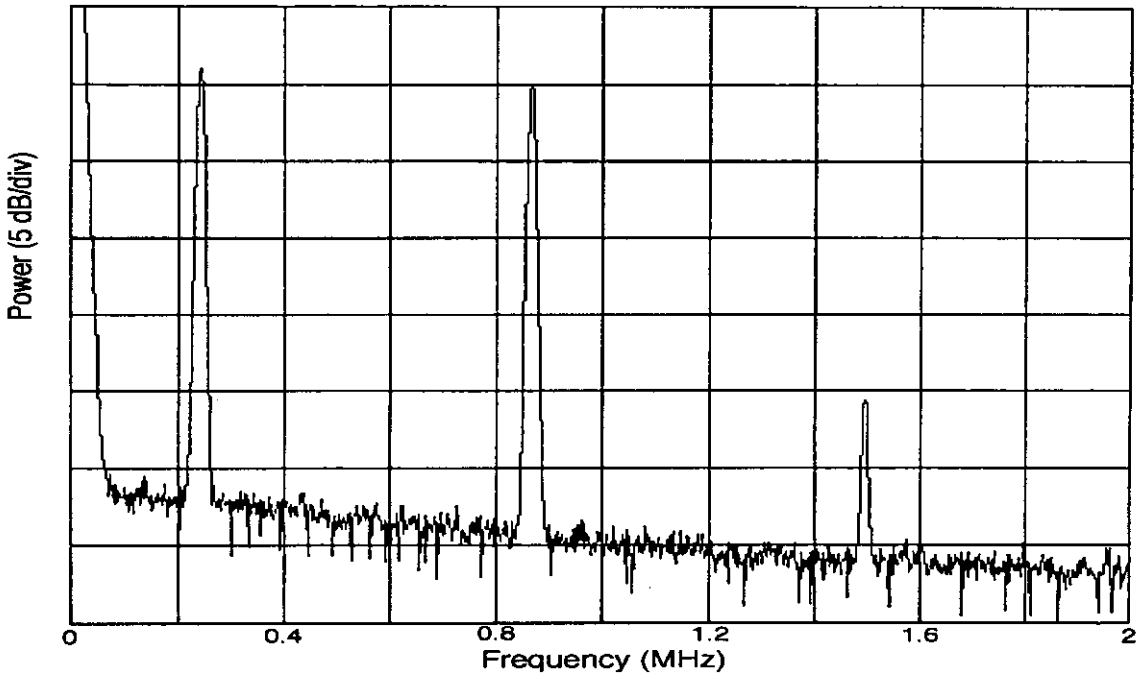

Figure 3.4: Beam coherent oscillation power spectrum. The four peaks from left to right are: $1/f$ noise, (1-q), (2-q) and (3-q) lines.

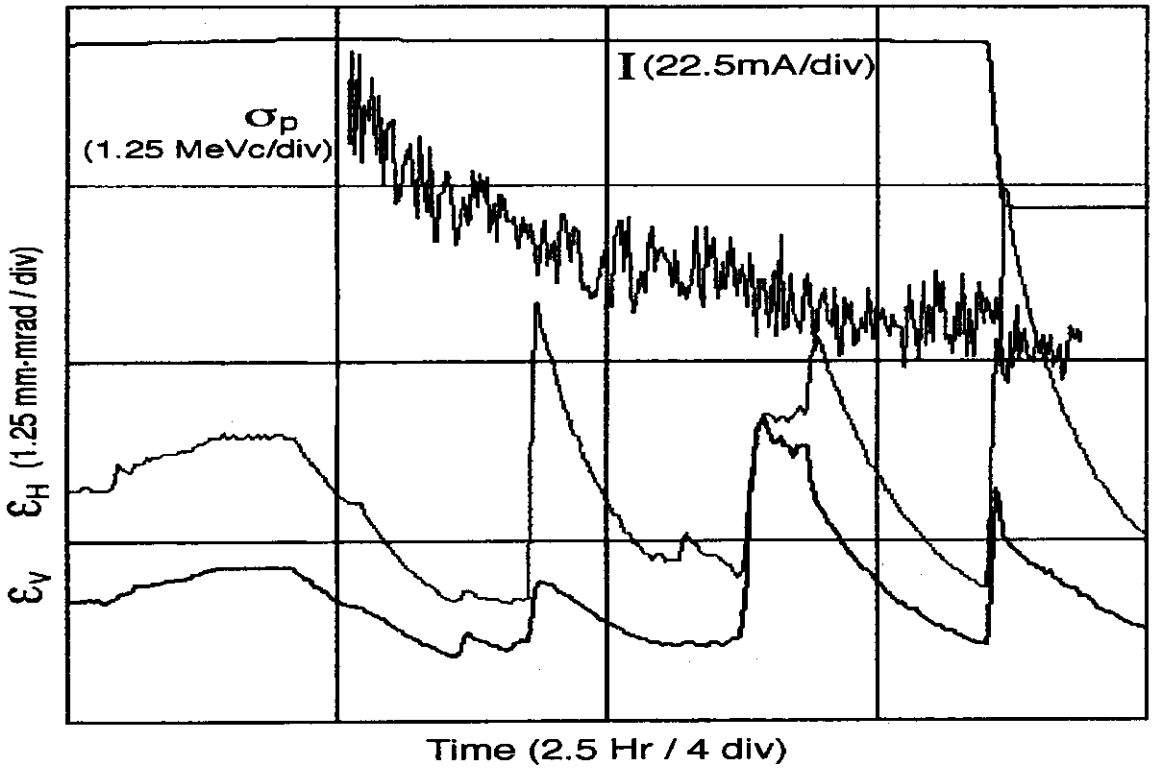

Figure 3.5: Beam emittance blowups when cooled

monitored with the damper pickup signal. With about $88mA$ of beam in the machine and clearing voltages set to $900V$, three lines at betatron sideband frequencies are visible, the left most peak is due to the $1/f$ noise and should be ignored. Higher frequency lines have not been observed and the monitoring frequency range is thus limited to that in Fig. 3.6. Among the 6 sectors in the accumulator, sector 20 is one of the three that show much smaller clearing currents compared with the other three sectors, so we have chosen to vary the clearing voltage of sector 20 to reduce the possibility of any harmful effects on the beam quality. With the gradual decrease of the clearing voltage in sector 20, which means the gradual increase of trapped ions, the beam coherent oscillation gradually increased power in all three modes. Fig. 3.6 shows the superimposed traces of spectra for sector 20's clearing voltages at $900, 100, 50$ and 10 volts (other sectors maintain the 900V clearing voltage). Clearly trapped ions increased the observed beam coherent oscillation power.

One explanation can be made with the model we developed in previous sections, that as the beam current increases, the ion impedance will gradually push the otherwise stable beam into the unstable region and cause the beam-ion coherent oscillation to grow. Unlike the normal machine impedance, the ion impedance changes as the beam-ion interaction alters the "equilibrium" ion distribution. When the beam develops an instability, resonant ions also undergo oscillation growth. Since the beam is normally much stronger and more rigid, the initial growth in the coherent oscillation tends to heat the ion distribution and drive the resonant ions to larger amplitudes. As a result, the initial ion distribution in Fig. 3.2 will be distorted and a notch in $\Psi'(\omega)$ with given depth may develop. This change in the ion distribution may put the beam near the edge of the modified stability area and the beam-ion oscillation stability may become semi-stable. A simple minded example, where a 100% notch is added without any other distortion, is used and the corresponding stability diagram changes from that in Fig. 3.3 to that shown in Fig. 3.7. A loop is created and part of its interior is stable area. The amplitude of the initial oscillation may be reduced or vanish as a result. This kind of effect has been observed in the Fermilab accumulator. One example is shown in Fig. 3.8 where the $(2-q)$ line power is monitored as a function of time. The main feature is that as the instability develops, the coherent line power jumps

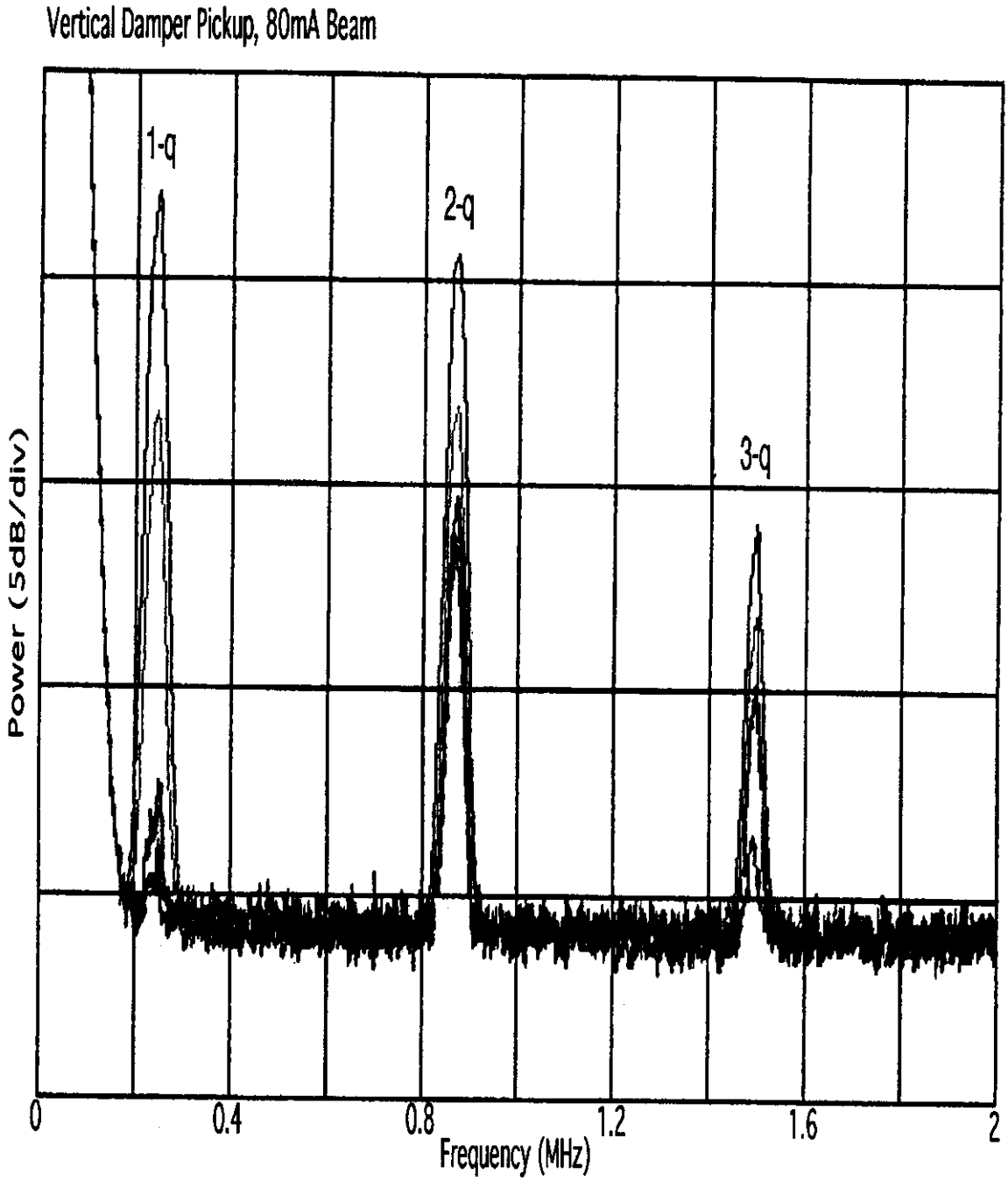

Figure 3.6: Coherent power spectrum with various clearing voltages. The four traces of coherent oscillation power are, from bottom up, with clearing voltages of 900V, 100V, 50V and 10V respectively.

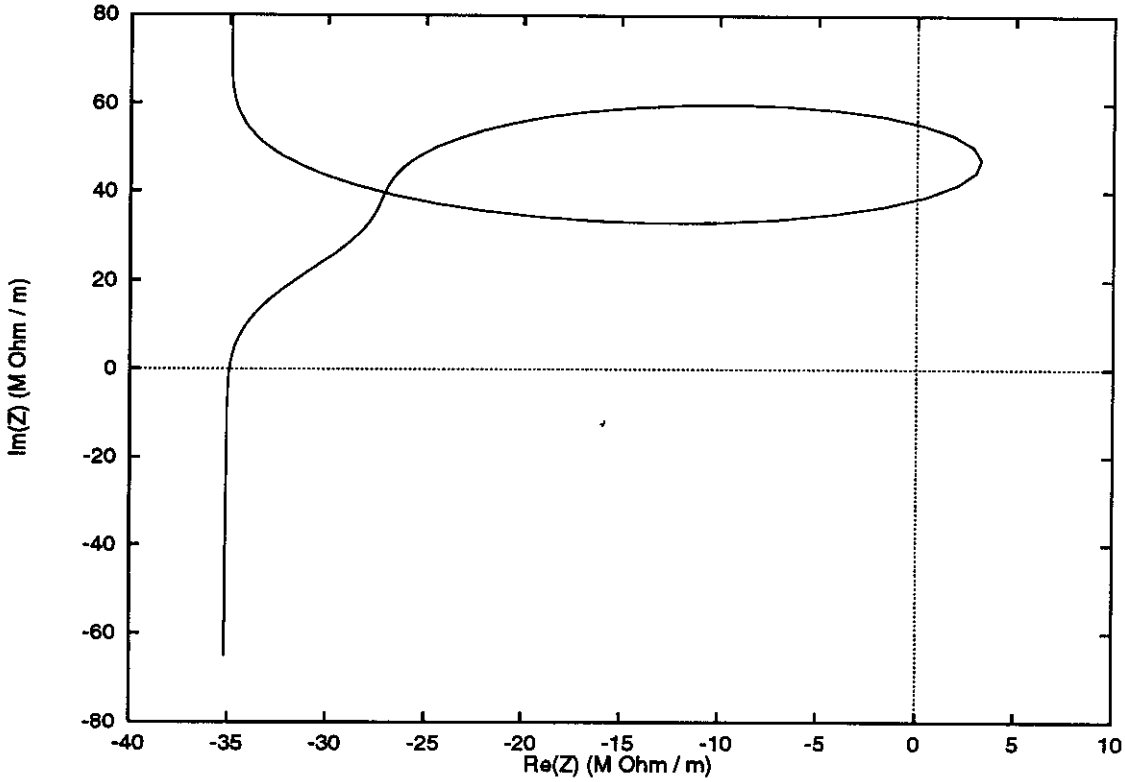

Figure 3.7: Horizontal beam stability diagram with 1% neutralization and notch distortion in ion distribution. Parameters used: $I = 100mA, \epsilon = 1\pi\, mm \cdot mrad, \xi = 0.3$.

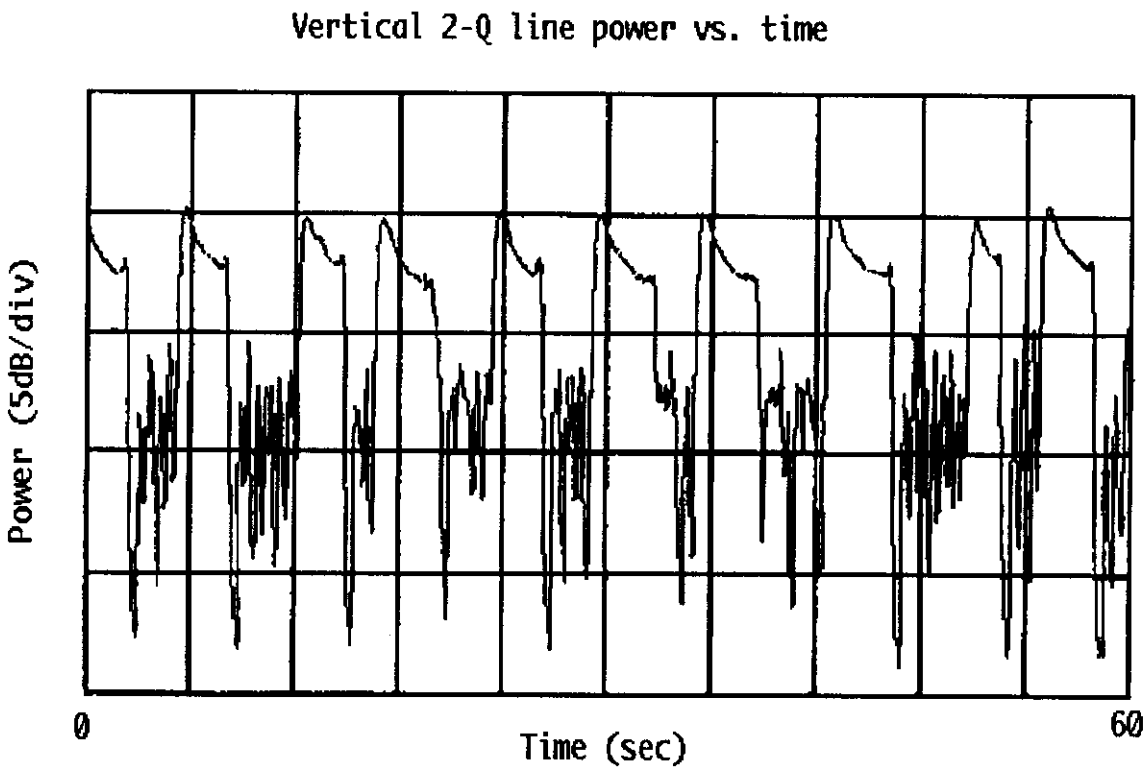

Figure 3.8: Coherent oscillation power change with time

up, undergoes a gradual decrease and then drops. After a few seconds, the instability re-occurs and the whole process appears to be semi-periodic. It is not difficult to see that on average some level of beam coherent oscillation is needed to maintain this modified ion distribution as the creation of new ions and the natural tendency of ions without heating will bring back the original ion distribution which caused the oscillation to grow in the first place. This process can be enhanced through the increase of beam current and/or the reduction of beam momentum spread, where either the beam moves closer to instability intrinsically because of the weakening of Landau damping or trapped ions become stronger or both can occur. When the trapped ions are strong enough and the instability growth is too fast for ions to respond, a true instability will develop and the beam transverse emittances will suffer explosive growth as has been observed. However, although this semi-periodic behavior follows the expected characteristics of the beam-ion interaction and notch development in the ion distribution, it is not a proof of this explanation. What is shown in Fig. 3.8 is only one example and the pattern of oscillation power as a function of time can be quite different at different times.

3.6 Beam Shaking

As we have seen from the result of section 3.4, the coherent influence of trapped ions on the beam, in the form of an extra impedance, can be diminished on two fronts: by reducing the overall neutralization level, i.e. diminishing ω_c in Eq. 3.82, or by changing the coupling to the coherent mode, i.e. reducing the integration term in the same equation. The first approach is the basic and direct solution and takes the form of clearing electrodes.

An adequate clearing electrode system usually takes away the majority of neutralizing ions, however, there usually are space between the electrodes and places like inside dipole magnets where there are no electrodes due the tight space there. As a result, machines are usually left with a residual low-level neutralization. The low level of neutralization usually has little effect on incoherent beam motion, but it may still cause a coherent beam instability, as we have seen from the examples in the last

section.

Beam shaking was first proposed by Yuri Orlov and co-workers[17][15] to further suppress the transverse beam coherent instability. It has been tested on several machines with negatively charged beams with generally positive results[44][12]. Permanent beam shakers have been installed on the CERN AA and the Fermilab accumulator as part of normal operation. Since then there have been variations proposed[10][45].

The basic setup of beam shaking includes a signal generator that can generate sinusoidal signals at the desired RF frequencies, an RF power amplifier and electrodes that deliver the kick to the beam. The beam undergos an oscillation that translates into an oscillating electric field at the same frequency which acts on ions around the machine. Near-resonant ions will be driven to larger amplitudes. Ions are in a nonlinear potential well created by the beam. Their bounce frequency will change, usually go down, as their amplitudes go up. Because of the longitudinal potential well depth variation, ions also oscillate in the longitudinal direction, and as a result they sweep through a range of transverse bounce frequencies. This enhances the effectiveness of beam shaking as, in the adiabatic limit, an ion's amplitude can only increase when its bounce frequency crosses the beam shaking frequency. For the natural distribution of ions, shown qualitatively in Fig. 3.2, this will tend to flatten the trapped ions' phase space distribution which will reduce the ion impedance around that frequency according to the theory in the last section. When the shaking frequency is close to the beam-ion coherent oscillation frequency this reduction in ion impedance will result in a stabilizing effect.

Beam shaking has been shown to improve machine performance[44][12]. However, since the clearing electrode system upgrade, beam shaking on the Fermilab Accumulator has not yielded a noticeable improvement and has since been turned off except for occasional studies.

Chapter 4

Bunched Beam Ion Dynamics

4.1 Introduction

Because of the presence of residual gas in the vacuum chamber, positive ions are constantly created by collisions with beam particles. When there is only a negatively charged DC beam present, positive ions created are almost always stable. They undergo oscillations in the electric field of beam. The strength of the beam only affects the oscillation frequencies of the ions. If the beam is bunched, then the ions experience a time-varying focusing force. The beam bunches can be viewed, in the simplest model, as focusing elements acting on ions[14][16]. The effect of these "focusing elements" on the ion motion depends on the beam transverse distribution and the bunch spacing scheme[46]. We will introduce some of the basic concerns with ion trapping in bunched beams and apply the normal procedure to the case of the Tevatron upgrade with separated proton and antiproton orbits.

The fields of an ultra-relativistic beam are almost purely transverse. In this limit the transverse electric field due to a Gaussian bunch with rms size in horizontal and vertical direction being σ_x and σ_y respectively is[26]

$$\begin{pmatrix} E_x \\ E_y \end{pmatrix} = Ze\frac{2\lambda\sqrt{\pi}}{\sqrt{2(\sigma_x^2-\sigma_y^2)}} \times \begin{pmatrix} Im \\ Re \end{pmatrix} \left\{ W\left(\frac{x+iy}{\sqrt{2(\sigma_x^2-\sigma_y^2)}}\right) - e^{-\frac{1}{2}\left(\frac{x^2}{\sigma_x^2}+\frac{y^2}{\sigma_y^2}\right)} W\left(\frac{x\frac{\sigma_y}{\sigma_x}+iy\frac{\sigma_x}{\sigma_y}}{\sqrt{2(\sigma_x^2-\sigma_y^2)}}\right) \right\}$$

where Z is the ion charge state, r_p the classical radius of proton and λ the particle line density, and W is the complex error function.

If the beam pulse length is short compared to an ion oscillation time, in general we can neglect the motion of ions during the time the beam bunch passes by them and treat the kick from the beam as a δ-function like impulse at the time when the center of bunch passes the ions i.e. using a thin lens approximation. Only the ion velocity is changed by the kick in this approximation, not its position. In the Tevatron, $\sigma_z = 40$cm. Taking $L = 2\sigma_z = 80$cm as the bunch length and simplifying the bunch as longitudinally uniform and transversely round, the analogue to the linear focusing strength in lattice theory is then (see Section 4.2), $K = \frac{ZNr_p}{A\sigma^2 L}$, where N is the number of particles per bunch and r_p the classical radius of proton. The thin lens approximation requires $\sqrt{KL} \ll 1$. For the Tevatron, the average transverse beam size is $\sim 0.5cm$ and in the above simplification $\sqrt{KL} \approx 0.6\sqrt{\frac{Z}{A}}$ for the biggest antiproton bunch density in the upgrade. Thus the thin lens approximation is only valid for ions with $\frac{A}{Z} \gtrsim 4$.

In this approximation we can write the change in transverse velocity of the ion due to a Gaussian bunch as

$$\begin{pmatrix} \Delta x' \\ \Delta y' \end{pmatrix} = \frac{Z}{A}\frac{2Nr_p\sqrt{\pi}}{\sqrt{2(\sigma_x^2-\sigma_y^2)}} \times \begin{pmatrix} Im \\ Re \end{pmatrix} \left\{ W\left(\frac{x+iy}{\sqrt{2(\sigma_x^2-\sigma_y^2)}}\right) - e^{-\frac{1}{2}\left(\frac{x^2}{\sigma_x^2}+\frac{y^2}{\sigma_y^2}\right)} W\left(\frac{x\frac{\sigma_y}{\sigma_x}+iy\frac{\sigma_x}{\sigma_y}}{\sqrt{2(\sigma_x^2-\sigma_y^2)}}\right) \right\}$$

where N is the total number of particles per bunch, A the ratio of ion to proton mass and

$$x' = \frac{1}{c}\frac{dx}{dt}$$
$$y' = \frac{1}{c}\frac{dy}{dt}$$

4.2 Linear Theory

For small amplitude ion oscillations ($x \ll \sigma_x$, $y \ll \sigma_y$) the transverse electric field can be linearized to give

$$E_x = \frac{2Ze\lambda}{(\sigma_x + \sigma_y)} \frac{x}{\sigma_x}$$

$$E_y = \frac{2Ze\lambda}{(\sigma_x + \sigma_y)} \frac{y}{\sigma_y}$$

We use s_b for the distance between two consecutive bunches and L for bunch length. The ion motion can be described by the following transfer matrices M_x, M_y for the passage of one bunch to the next one:

$$\begin{pmatrix} x \\ x' \end{pmatrix}_{n+1} = M_x \begin{pmatrix} x \\ x' \end{pmatrix}_n$$

where

$$M_x = \begin{pmatrix} 1 & s_b - L \\ 0 & 1 \end{pmatrix} \begin{pmatrix} \cos(\sqrt{K}L) & \frac{1}{\sqrt{K}}\sin(\sqrt{K}L) \\ -\sqrt{K}\sin(\sqrt{K}L) & \cos(\sqrt{K}L) \end{pmatrix}$$

and similarly for M_y in the vertical direction.

In the thin lens approximation, the equations above simplify to

$$\Delta x' \equiv a_x x = \frac{2ZNr_p}{A(\sigma_x + \sigma_y)} \frac{x}{\sigma_x}$$

$$\Delta y' \equiv a_y y = \frac{2ZNr_p}{A(\sigma_x + \sigma_y)} \frac{y}{\sigma_y}$$

and

$$M_x = \begin{pmatrix} 1 & s_b \\ 0 & 1 \end{pmatrix} \begin{pmatrix} 1 & 0 \\ -a_x & 1 \end{pmatrix}$$

If the bunches are equally spaced, and the fluctuation in bunch to bunch density and revolution frequency are neglected, then the stability of ions requires that $TrM_x < 2$ and $TrM_y < 2$. This then leads to a critical mass such that ions with mass greater than critical will be stable and smaller than critical unstable. The critical mass is thus set by the higher of $TrM_x = 2$ and $TrM_y = 2$. Explicitly we have

$$A_c = \frac{ZNs_b r_p}{2(\sigma_x + \sigma_y)} \cdot \frac{1}{\min(\sigma_x, \sigma_y)}$$

As can be seen here, the most probably place for ion trapping to occur is where the beam size is big i.e. large beta functions. In the Tevatron this corresponds to regions of large beta function values just outside the colliding points.

The variation in the spacing between bunches and in bunch-to-bunch density will introduce stop bands in the otherwise stable region of ion mass. In general if we have n different bunch spacings $s_1, \ldots, s_n$ and bunch densities $a_1, \ldots, a_n$ that is repetitive, then the ion stability will be determined by the transfer matrix

$$M = M_1 \cdot M_2 \ldots M_i \ldots M_n$$

where

$$M_i = \begin{pmatrix} 1 & s_i - L \\ 0 & 1 \end{pmatrix} \begin{pmatrix} \cos(\sqrt{K_i}L) & \frac{1}{\sqrt{K_i}}\sin(\sqrt{K_i}L) \\ -\sqrt{K_i}\sin(\sqrt{K_i}L) & \cos(\sqrt{K_i}L) \end{pmatrix}, i = 1 \ldots n$$

and in general we will have n stable bands in ion mass.

4.3 Nonlinear Effects

The electric field expressed at the beginning of this section is very nonlinear when the distance is greater or comparable to the beam's rms size. If we want to consider also the stability of large amplitude ions, or the effect of proton beam from a separated orbit when we have two beams in the ring, then we have to work with the nonlinear force. First, when ions are far enough from the beam center this force becomes locally defocusing. The consequence of this is that the stability for large amplitude ions is almost solely determined by the longest gap between any two consecutive bunches. Secondly, it introduces coupling between the horizontal and vertical directions.

The calculation is not as simple as in the linear case. We have to track the motion of ions to test their stability. A computer code was developed to do both the linear calculation and nonlinear tracking of the ions. To avoid the extremely time-consuming

numerical integration, the code uses the thin lens approximation, which means it is not applicable to very light ions. The effect due to the fluctuations in bunch density is ignored. The code also tracks ion motion inside a dipole magnet. Caution has to be taken here. In the Tevatron, the magnetic field of the dipole magnets is 3.8 T and the corresponding proton cyclotron frequency is $\omega = \frac{eB}{m_p} = 0.36GHz$. The rotation angle of a proton during the 3 ns of the beam bunch passage time is 60 degrees. Therefore the range of this thin lens approximation in the nonlinear calculation should be $A \gtrsim 20$, regardless of bunch density.

4.4 Tevatron

4.4.1 Tevatron Upgrade

With the Fermilab upgrade plan, the Tevatron in its 1991 and following collider runs will have separated proton and anti-proton orbits. The average separation is greater than 5σ[47]. The electric force due to proton beam, which acts as a clearing force to ions, is greatly reduced and therefore leaves the possibility of having ions trapped around the anti-proton orbit. Here we investigate whether there will be trapped ions in the Tevatron using the upgrade performance parameters and if so, where and under what circumstances this will happen.

Listed in Table 4.1 are the parameters for Tevatron collider run III, IV and V, that are of concern in the following calculation, under the Fermilab upgrade plan. The bunch spacing scheme notation can be best explained using an example, e.g. $5 \times 42 + 161$ means there are five bunches that are separated by 42 RF buckets plus another bunch that is separated by 161 RF buckets from the end of the five bunches. The pattern will be repeated, if necessary, until the number of bunches is equal to the required number.

4.4.2 Calculation Results

Fig. 4.1 shows the Tevatron lattice functions in the collider mode. There are two characteristic parts. One includes the regular cells and the other the low beta

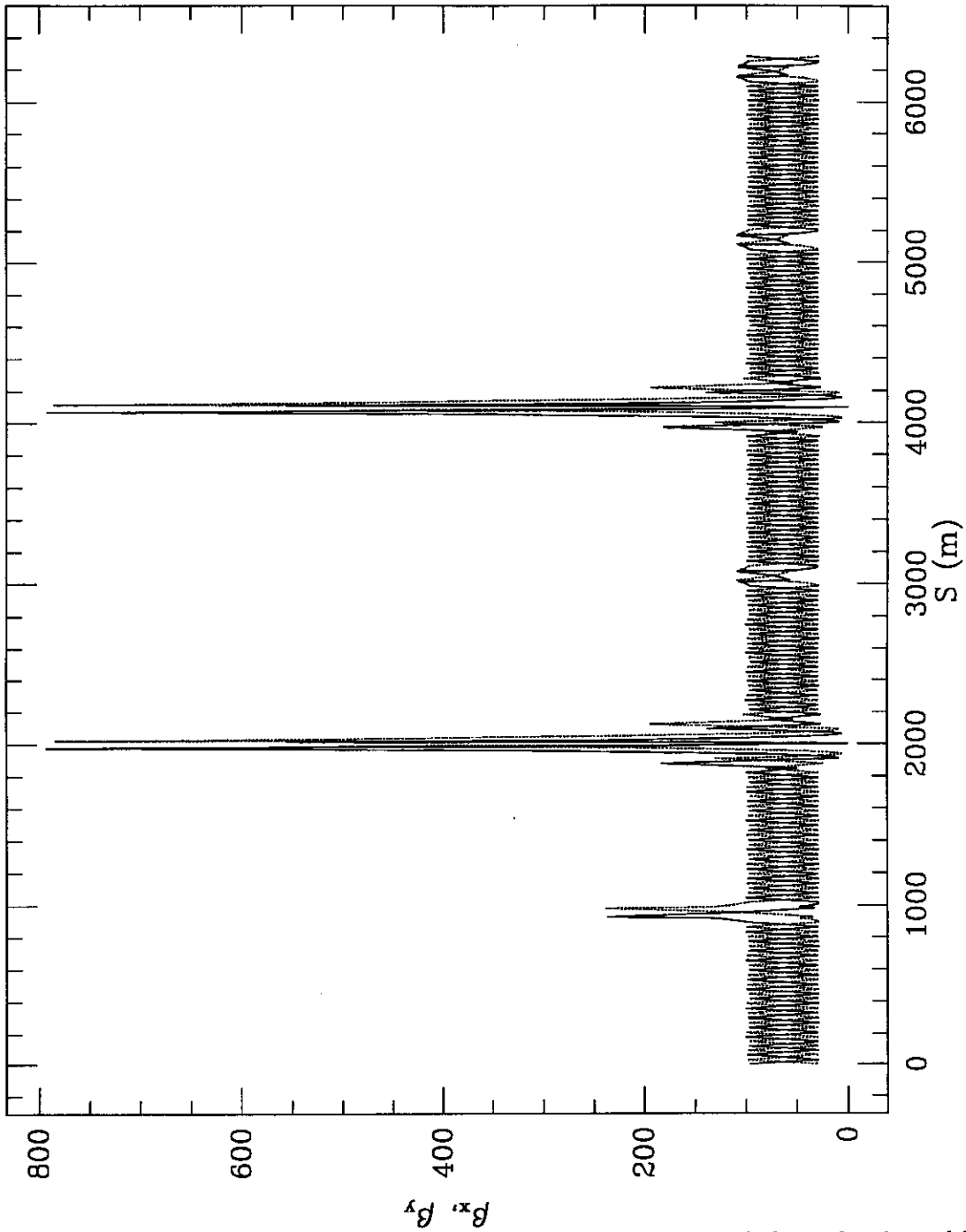

Figure 4.1: Tevatron beta functions. β_x is the solid line and β_y is the dotted line.

Run #		III	IV	V
Number of bunches		6	18 (36)	18 (36)
Bunch spacing (RF buckets)		185 186	$5 \times 42 + 161$ $(11 \times 21 + 140)$	$5 \times 42 + 161$ $(11 \times 21 + 140)$
# of particles/Bunch (10^{10})	proton	7 – 10	10 – 15	33 – 50
	pbar	7.2	3.4 (1.7)	7.3 (3.7)
Transverse emittance (95%, π mm-mrad)	proton	15	15	30
	pbar	14	19	22
Momentum spread (rms, 10^{-4})	proton	1.2	1.2	1.2
	pbar	1.2	0.38	0.27

Table 4.1: Parameters for the Tevatron upgrade

insertions. Linear calculations have been carried out, ignoring the proton beam, for one representative regular lattice point $s = 320$. Fig. 4.2 shows the stable mass bands for all three operational modes. In this and all following calculations we will only pay attention to ions with $\frac{A}{Z} = 1, 2, 4, 28$ which corresponds to singly ionized H, H_2, He, N_2, CO and most fully ionized ion species. For comparison we also show the results for cases of 18 and 36 bunches in Fig. 4.3, but with the bunches distributed in almost periodic fashion, i.e. instead of $(5 \times 42 + 161)$ in the 18 bunch case, we use $(5 \times 62 + 61)$, and instead of $(11 \times 21 + 140)$ we use $(11 \times 31 + 30)$. The comparison is unambiguous — the big gap (abort gap), greatly destablizes ions. Also by doing tracking on cases where the linear calculation predicts stable motion in both horizontal and vertical direction for different initial amplitudes ($< \sigma$), we verified the observation made in the previous section that because of the accumulation of the nonlinear effect, except for very small amplitude oscillations, these narrow stable bands virtually do not exist.

From the stability plot we can see that, in the mass range of interest, the stable bands are all very narrow. This means even very small amplitude ions are barely stable. Adding the proton beam to the nonlinear calculation, with reasonable separation, we find that ions are knocked out almost immediately. This can be easily explained using the following argument. The average force from the proton beam is $\propto \frac{N_p}{R}$ where R is the separation between proton and antiproton beam, and the

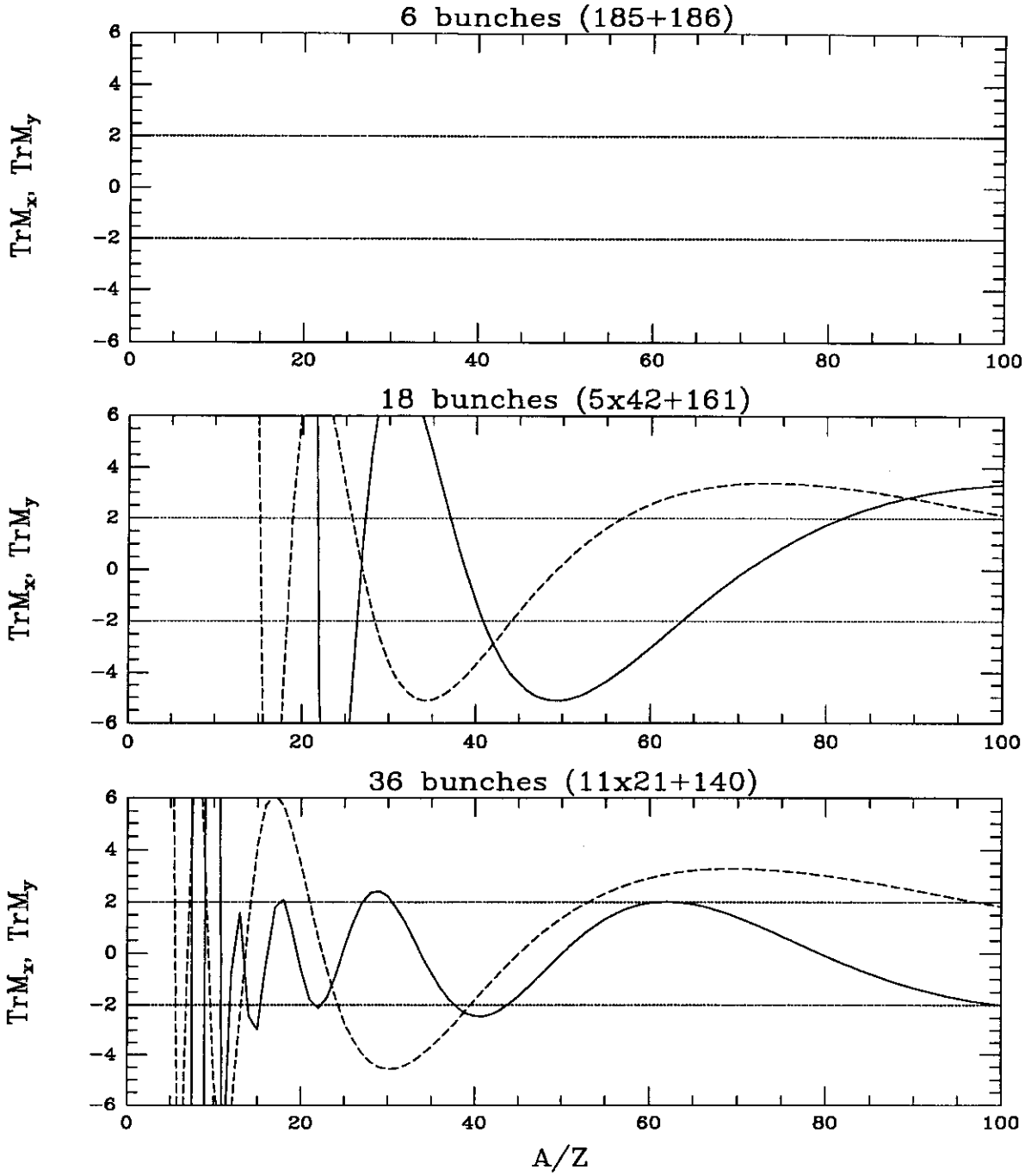

Figure 4.2: Linear stability plot at S=320m. Solid lines are for $Tr(M_x)$ and dashed-lines are for $Tr(M_y)$. The stable region is the area of $-2 < Tr(M_{x,y}) < 2$.

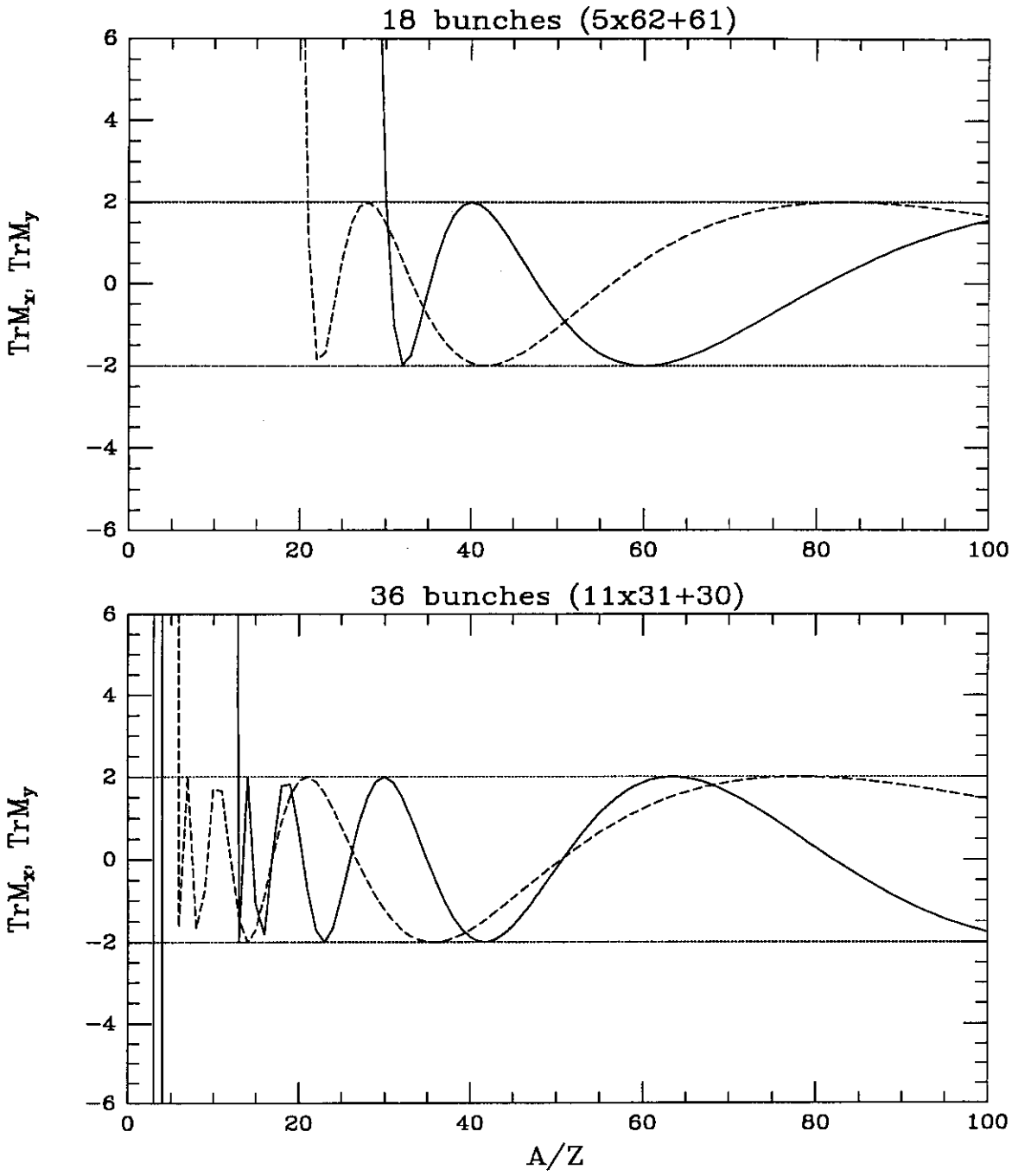

Figure 4.3: [Linear stability plot at S=320m. Solid lines are for $Tr(M_x)$ and dashed-lines are for $Tr(M_y)$. The stable region is the area of $-2 < Tr(M_{x,y}) < 2$.

maximum focusing force from the antiproton beam is $\propto \frac{N_p}{\sigma_p}$. So when $\frac{N_p}{N_{\bar{p}}} > \frac{R}{\sigma_p}$ no ions are stable. When this is not satisfied the proton beam field contributes to driving the ions out of the linear antiproton beam force region and into unstable motion.

This leaves our concern only to the high beta sections around the colliding points, which, according to linear theory, are the most probable places to trap ions.

Linear and nonlinear calculations have been done at $s = 2040$ which has $\beta_x \sim 87m, \beta_y \sim 390m$. Fig. 4.4, 4.5 show the linear calculation results. This should be the most favorable place for ion trapping because β_y is close to its maximum and occurs inside a dipole magnet and thus horizontal motion is automatically stable. The cycloidal motion due to crossed $\vec{E}$ and $\vec{B}$ fields results in a secular longitudinal (z) drift. Stable ions drift towards the ends of dipole magnet and accumulate there. In our simulation we neglect the effect of this drift on the bunch passing time because the drift is usually $\lesssim 1m$ in the time scale of our simulation compared to the length in one RF bucket $\sim$ 5.6m and the length of dipole magnets $\sim$ 6m. In Fig. 4.6 we show a sample Poincare plot of a stable motion for $A = 28$ with only an anti-proton beam. In all three modes, light ions are unstable as can be seen from linear stability plot, but for the two multi-bunch modes with only an antiproton beam, ions with $A = 28$ and $A = 44$ are stable and, this stability only occurs inside the dipole magnetic field. In all the listed operation modes, adding the proton beam with the design density clears ions out except when the two beams are very close to being purely horizontally separated. There will be both horizontal and vertical separators between the colliding point and the dipole magnet in consideration according to the proposed separator locations[47], and the separation between proton and antiproton beams is only 2–3σ around this point. These conditions exclude the possibility of trapping ions here.

To summarize, in the Tevatron, there will not be any light ions trapped with or without a proton beam. With the planned intensity proton beam present other ions of concern are not likely to be trapped either. If there is only an antiproton beam in the ring, then trapping is possible for ions like CO, N_2 and CO_2, but almost exclusively in dipole magnets. Inside superconducting magnets, residual gas is composed of mostly light ions and very few heavy ions, and additionally as these heavy ions get further

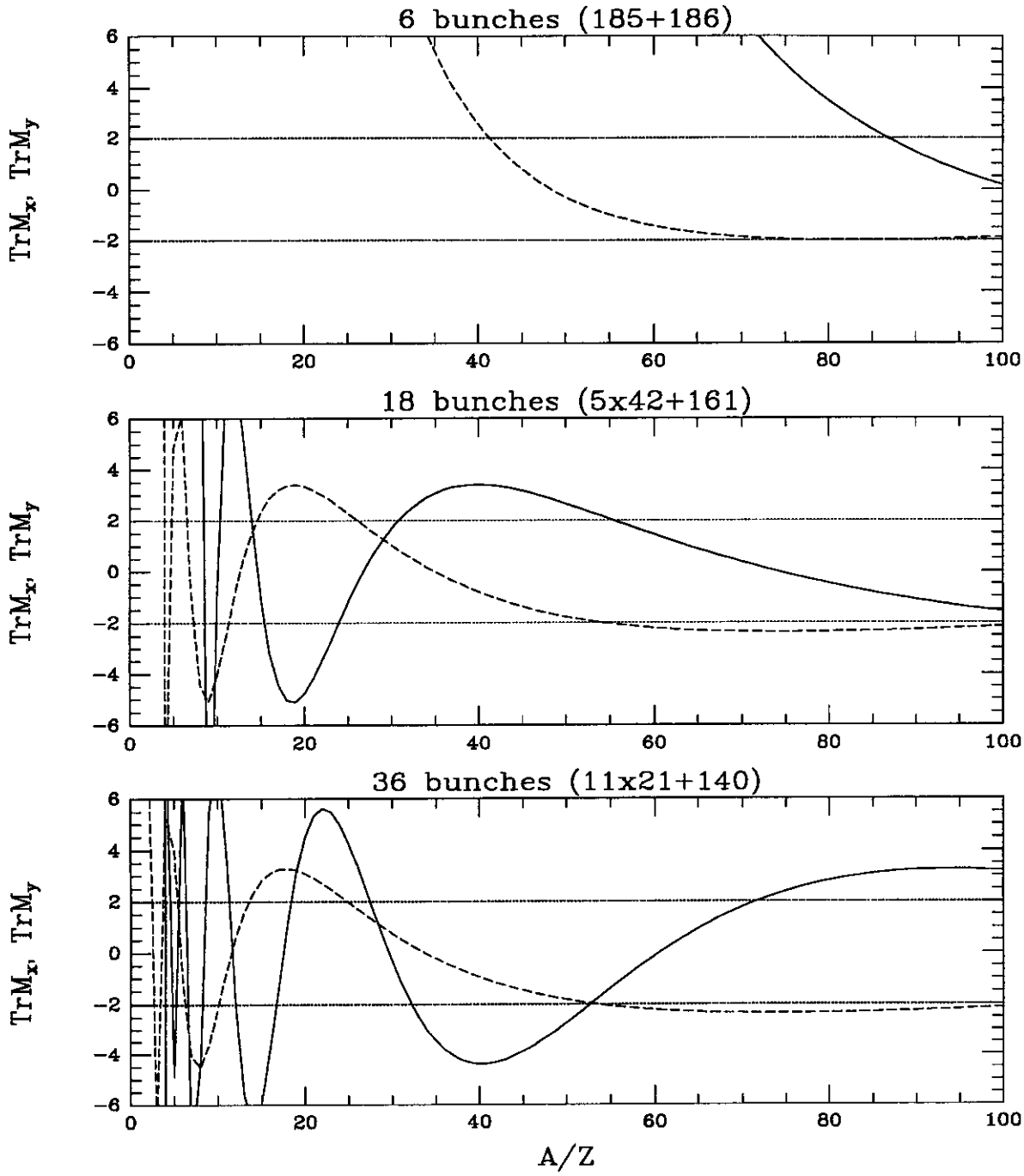

Figure 4.4: Linear stability plot at S=2040m. Solid lines are for $Tr(M_x)$ and dashed-lines are for $Tr(M_y)$. The stable region is the area of $-2 < Tr(M_{x,y}) < 2$.

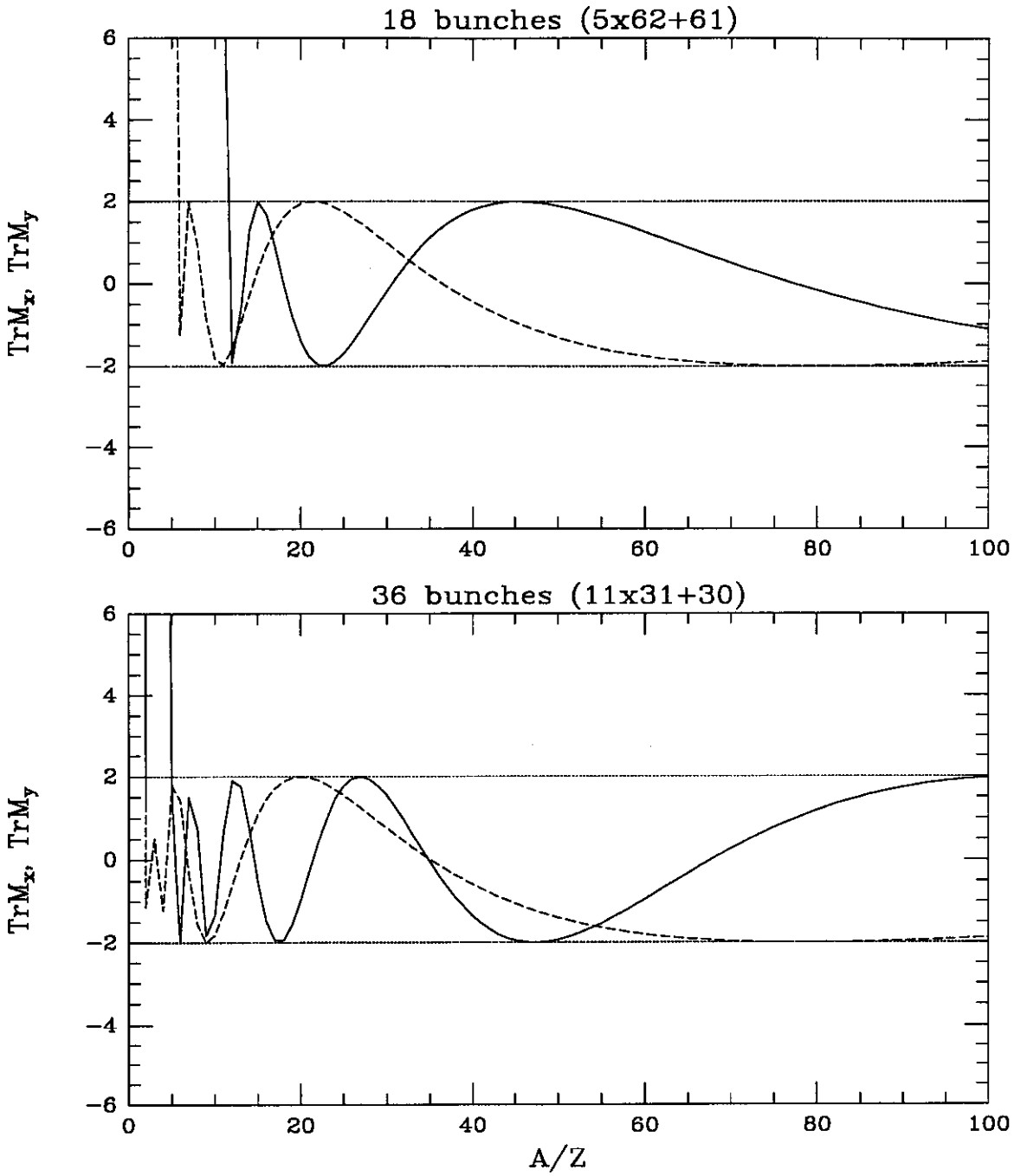

Figure 4.5: Linear stability plot at S=2040m. Solid lines are for $Tr(M_x)$ and dashed-lines are for $Tr(M_y)$. The stable region is the area of $-2 < Tr(M_{x,y}) < 2$.

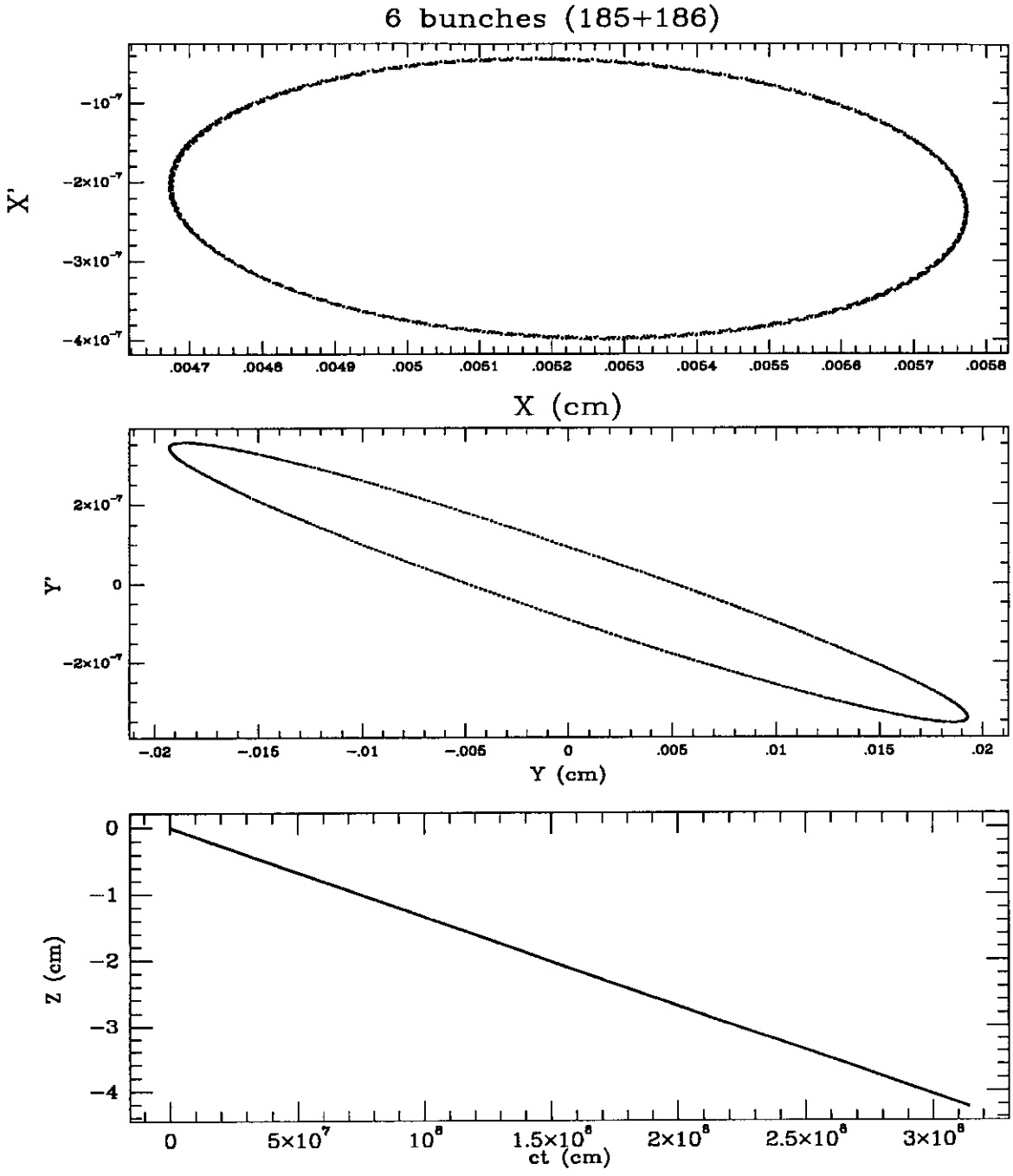

Figure 4.6: Stable ion Poincare plot with pbar beam only

ionized they will become unstable. Therefore it is safe to say that in collider runs III, IV and V ion trapping will not be a problem for the Tevatron.

Chapter 5

IDEA - Ion Detector and Energy Analyzer

5.1 Introduction

The diagnostic system of the accumulator provides valuable information about the beam and trapped ions, but does not provide enough details for ion trapping studies. To directly obtain the information about the ions coming out of the beam potential well and establish the direct link between the beam instability and trapped ions, we built and installed an Ion Detector and Energy Analyzer (IDEA). The hope was that with a direct observation, we could gain more information on e.g. what happens when a coherent instability develops between the beam and trapped ions the direct effect of beam shaking on ions, and ion energy distribution and etc. We will describe the detector setup and the whole system here, and present the experimental modelling results in the next chapter.

5.2 Structure and Installation

The mechanical setup together with its relative position with respect to the vacuum pipe is shown in Fig. 5.1. The probe can be moved into position manually once the gate valve is opened. The probe orientation, see Fig. 5.2 can be rotated through a range of almost 180° through the Fermilab control system. The precision of the angle control is about $\pm 1°$, and can be improved in the future by modifying the mechanical setup. By mounting the assembly at different rotational angles, we can make the probe scan across the beam longitudinally or transversely.

In Fig. 5.3, the schematic drawing of the probe and setup of the electric control and data acquisition system is shown. In the front of the probe are the two energy discrimination electrodes. We will call the outermost electrode the front plate and the inside one gate plate. These two plates can be independently biased with voltages remotely. The next grounded grid serves to separate of energy discrimination part from the detection part. These grids consist of stainless steel plates with circular holes in the center, and the holes are covered by nickel mesh with about 70% transmission. Applying various voltages on either the front plate or the gate plate will repel ions with less equivalent kinetic energy per unit charge, thus selecting only those with higher kinetic energy. With a voltage scan, we can measure ions' integrated energy distribution, which after differentiation yields the true energy distribution of the ions.

At the heart of the probe is a three stage Micro Channel Plate (MCP) (Hamamatsu Type F1551-31). An MCP is a device consisting of a two-dimensional array of millions of very small diameter glass capillaries (channels) fused together and sliced in the shape of a thin disc[48], see Fig. 5.4 for an illustration. The inside wall of each channel is processed to have a specific resistance, forming an independent secondary electron multiplier. When a voltage is applied across the two ends, secondary electrons emitted from the channel wall on impact by the input particles are accelerated by the electric field, striking the opposite wall and producing more secondary electrons. This process is repeated many times along the channel, as a result forming a high gain device. Two or three of these discs can be stacked together to form a two or three stage MCP with gains as high as a few 10^7.

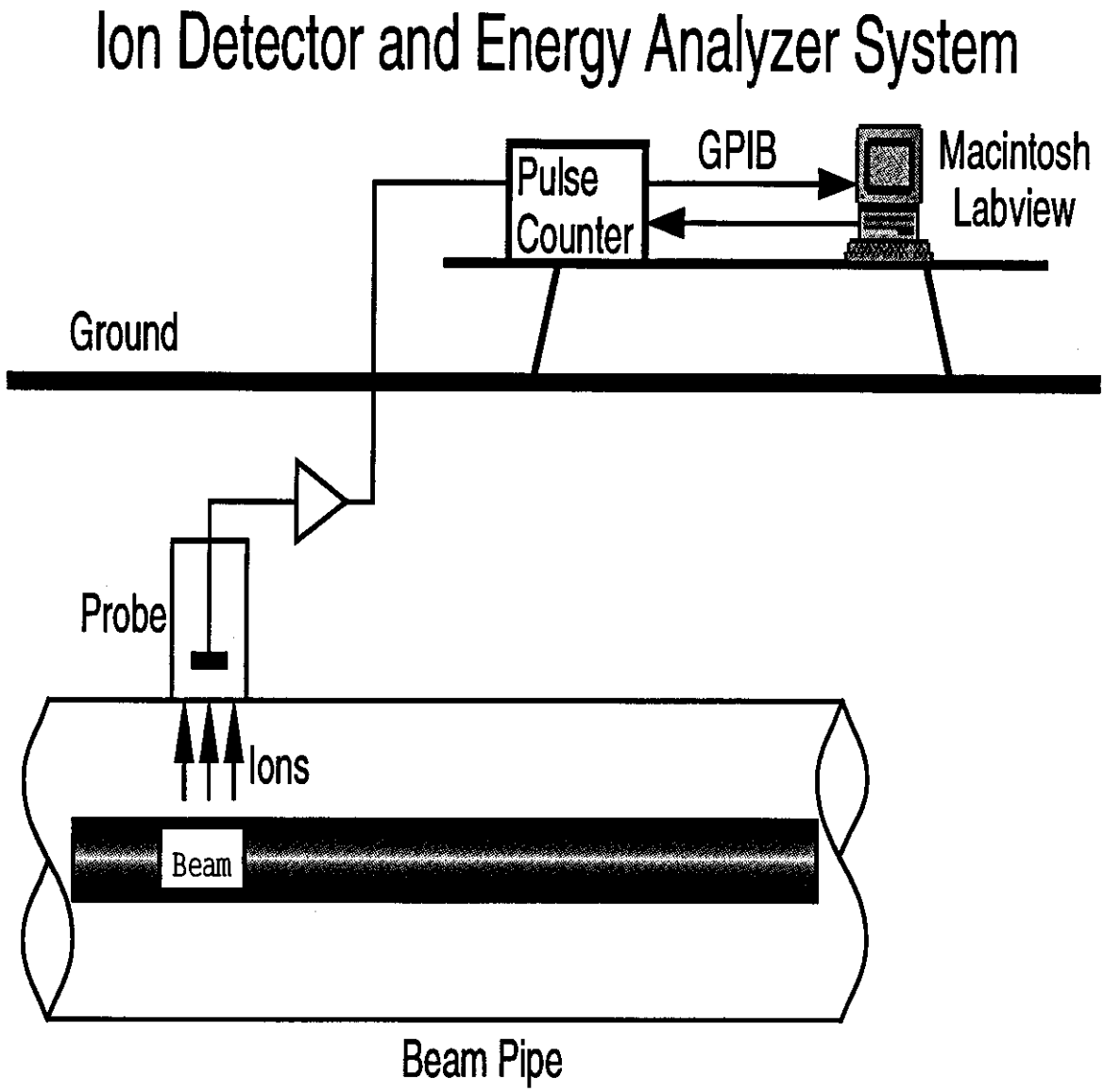

Figure 5.1: Schematics of Ion Detector and Energy Analyser system

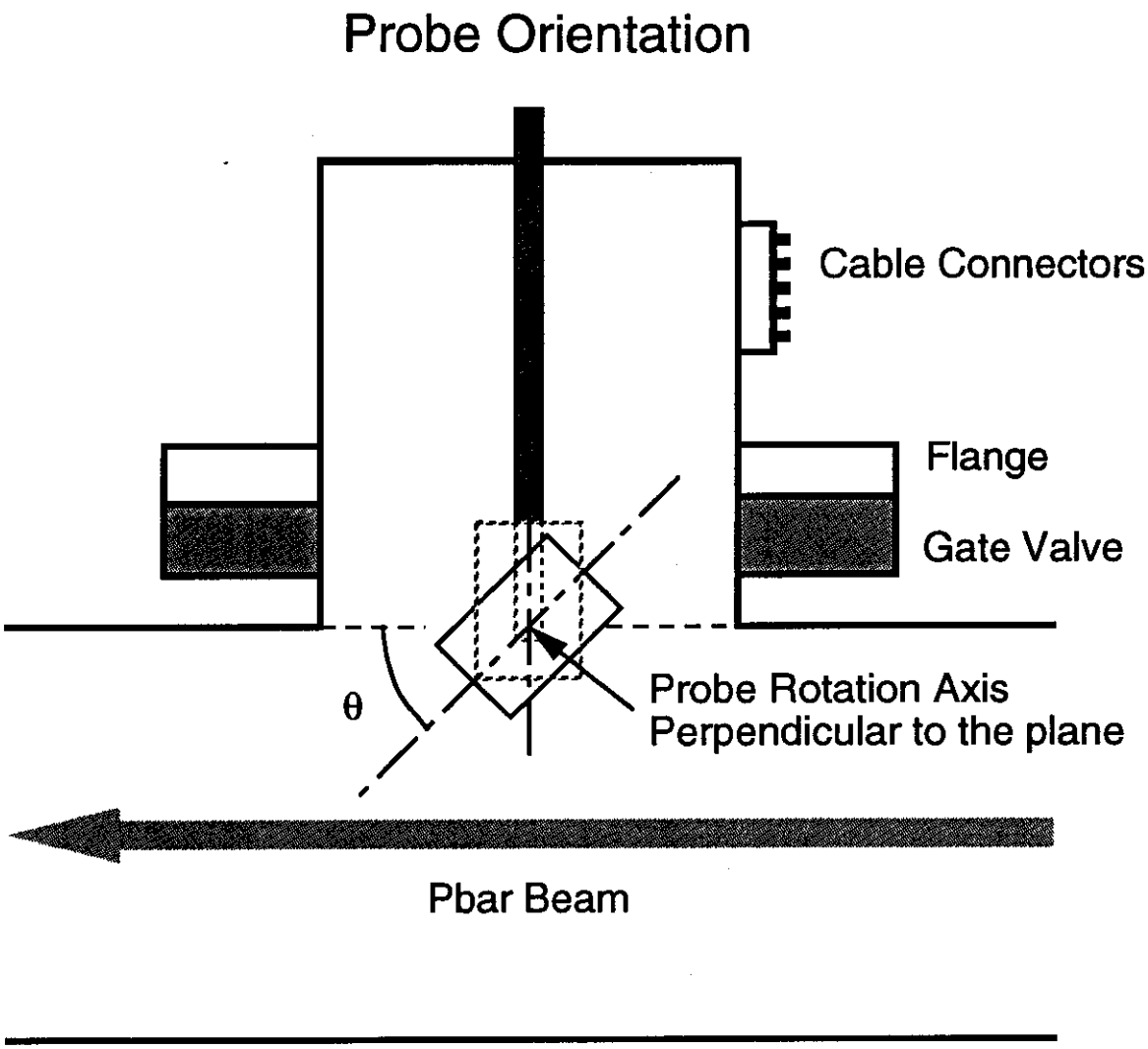

Figure 5.2: IDEA probe orientation

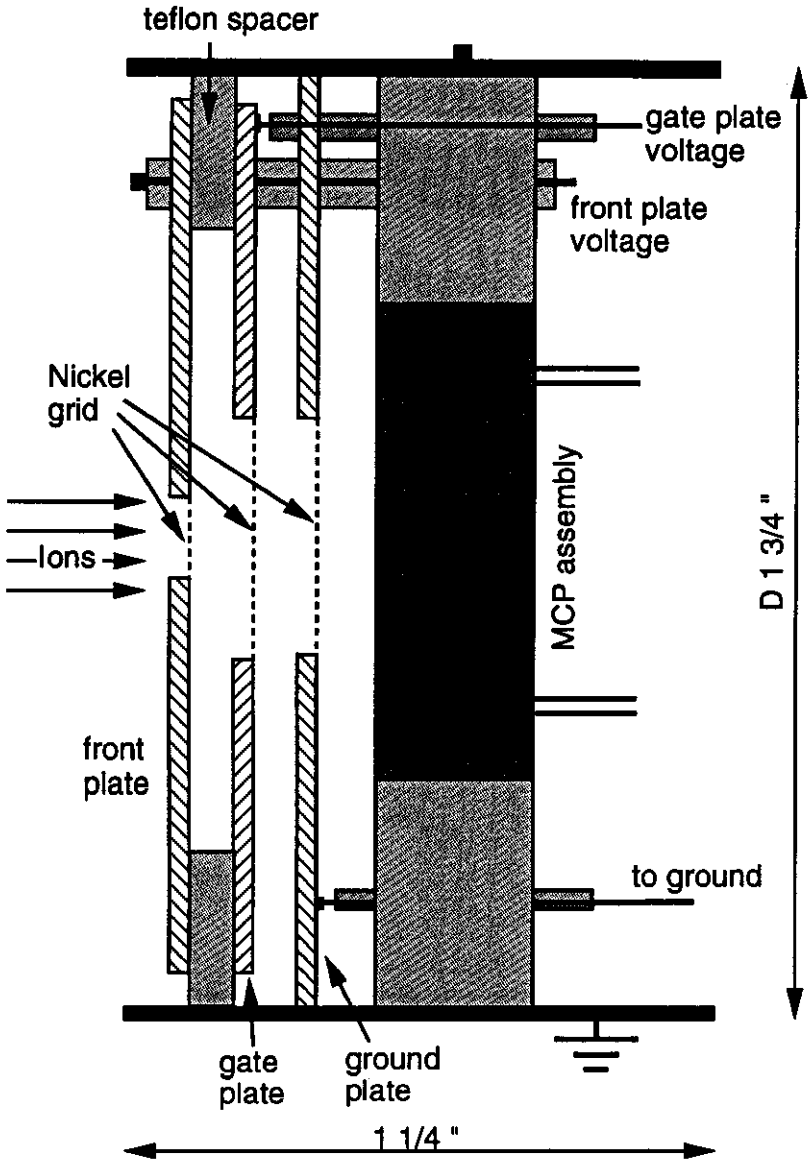

Figure 5.3: Schematic drawing of the IDEA probe. Scales are approximate.

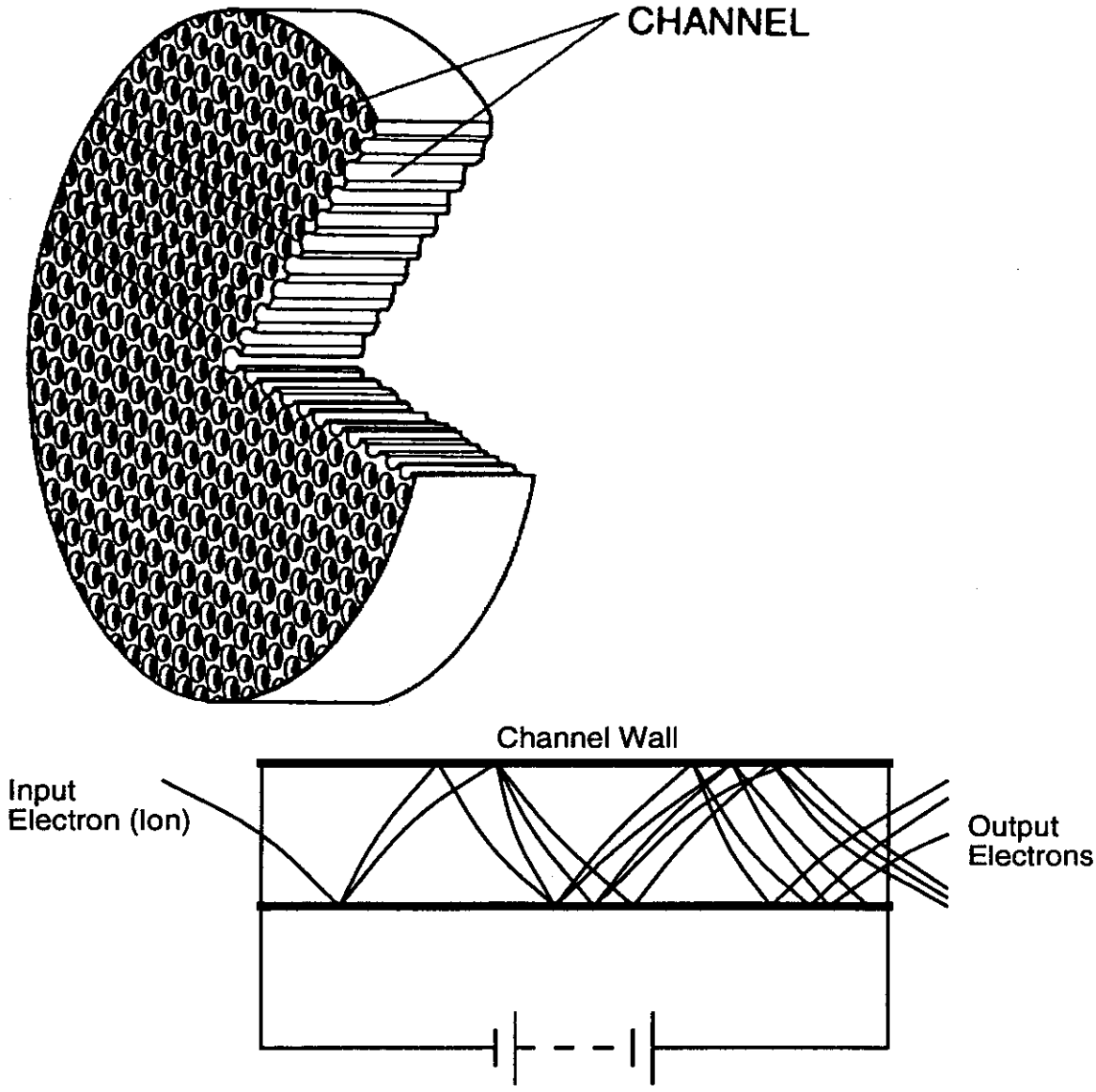

Figure 5.4: Schematic construction and operating principle of MCP

The gain of an MCP as a function of the voltage applied across it looks qualitatively like what is shown in Fig. 5.5[48]. To obtain a high gain for the ease of

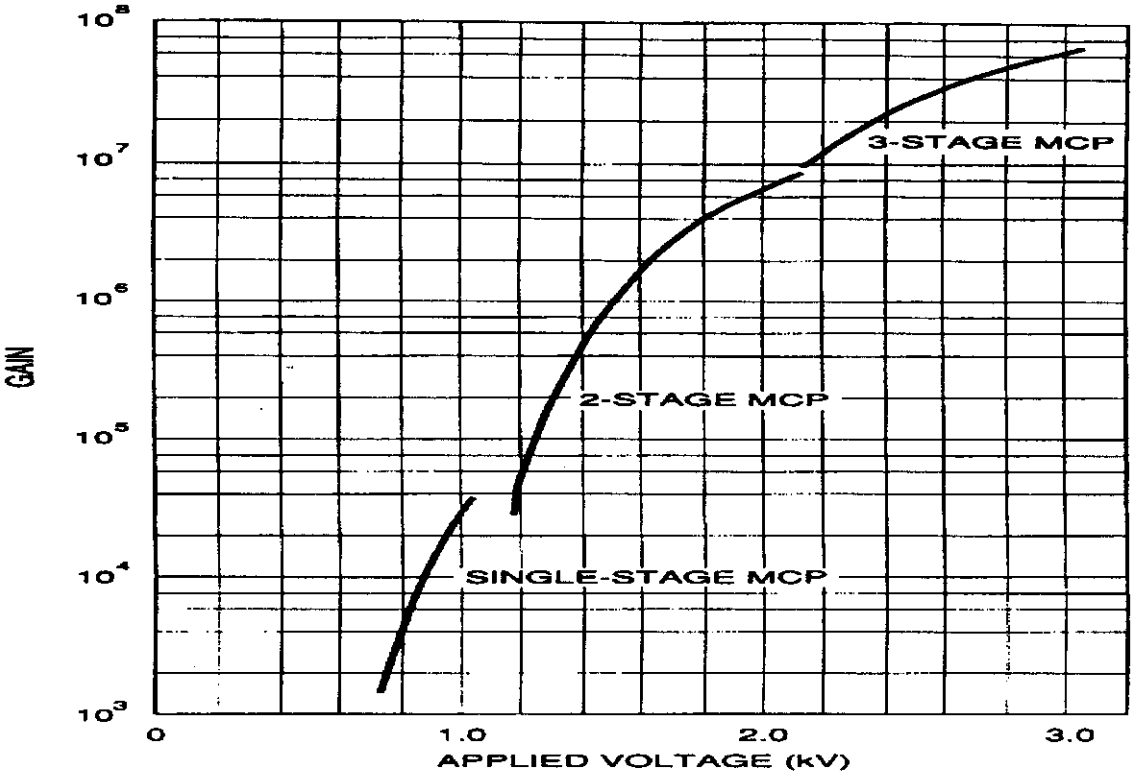

Figure 5.5: MCP gain characteristics

electronics in later stages, a high voltage $\gtrsim 2KV$ must be applied. There are two ways to apply the high voltage to the MCP, by either applying a positive high voltage on the back plane or by applying a negative high voltage on the front plane of the MCP. Since we are interested in detecting positively charged ions, the approach with a negative high voltage on the front plane is selected, see Fig. 5.6. This way, the field generated by this negative voltage between the MCP and the last grounded plate in the probe also accelerates the ions to a high kinetic energy level, increasing the detection efficiency of the ions by the MCP. In addition, this voltage also gates out at least the majority, if not all, of the electrons that enter the probe, reducing greatly the number of false counts. As for those really energetic electrons that may overcome this voltage and cause false counts, they are unlikely to be affected by the low gate

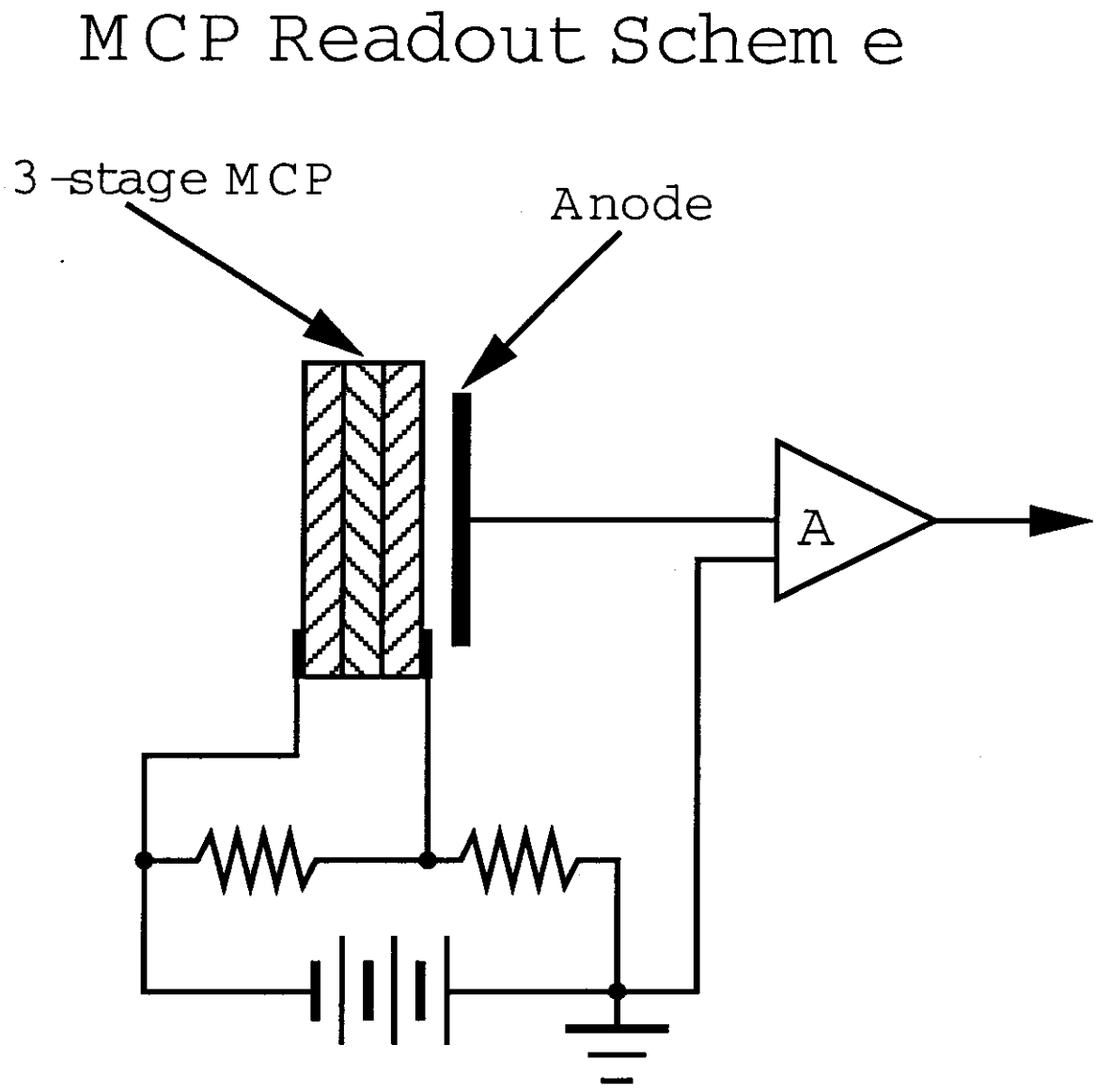

Figure 5.6: MCP readout scheme

voltage and serve only as a background in the energy scan measurements. Low energy neutral particles can enter the probe, but their detection efficiency is very low, a few percent. This high voltage configuration also makes the connection to the following amplifier easier, since there is no need for any voltage separation between the probe and the amplifier, which is at ground.

The low negative voltage on the back plane of the MCP serves the purpose of focusing and accelerating the electrons, thus ensuring the capture efficiency at the anode. Pulses coming out of the MCP have a large amount of charge, $\sim 10^6 - 10^7 e$, and a very short time structure, $\sim$ nanoseconds. They are then amplified by the preamplifier and other amplifiers if needed and then counted. The preamplifier stays in the accumulator tunnel close to the detector to avoid signal loss and to minimize the effect of electronic noise. The pulse counter is placed remotely for ease of control and operation.

The structure is installed in sector A60 about 1.6 meters downstream from the center of quadrupole magnet no. 6 where the vacuum chamber is a round pipe of 4 inch diameter. The actual position, together with the beam potential, is shown in Fig. 5.7. The local lattice functions have the following values, $\beta_x = 22m, \beta_y = 2m, D = 1.3m$. A small β_y enables the probe to partially enter into the vacuum pipe, so the angular scan can be made, without danger of being hit by the beam. It is mounted on the Accumulator beam pipe through a rotatable flange. The vacuum of the IDEA assembly can be separated from the beam pipe vacuum by a gate valve.

5.3 Control and Data Acquisition

The signal pulses out of the MCP, after amplification, are counted and the count rate information recorded. The pulse height discrimination and counting are done with a Stanford Research Systems' SR400 dual photon counter. The large number of high power devices in the Accumulator and Debuncher enclosure makes it a very noisy electronic environment. The electron multiplication in the MCP is a random process, and so are the amplitudes of the final pulses. The pulse height distribution is the superposition of the intrinsic distribution of the MCP and the noise spectrum.

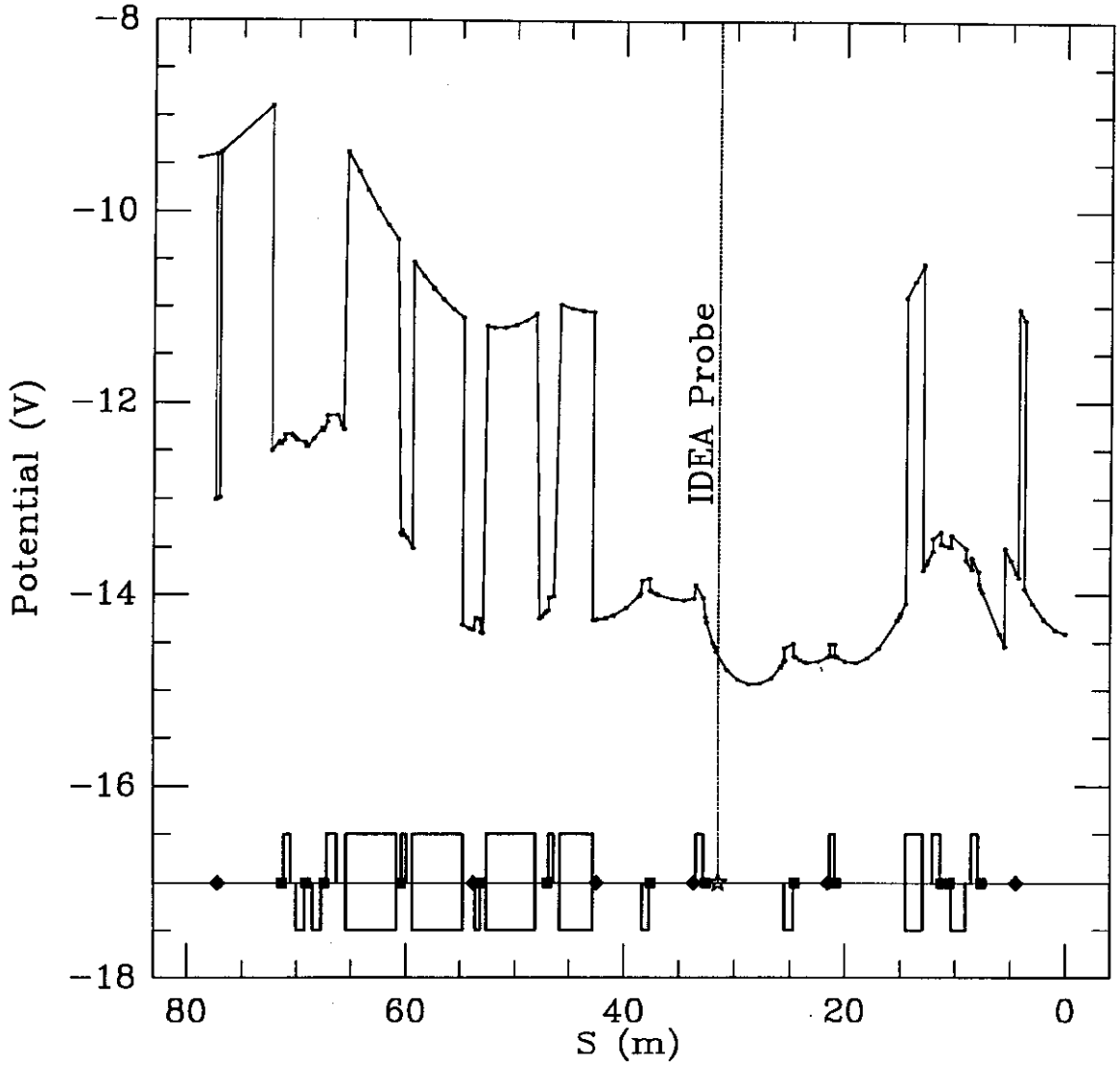

Figure 5.7: Probe installation position and beam potential

It can be measured by varying the discrimination level. It is also affected by the gain of the MCP: the bigger the MCP gain, the more spread there is in the final pulse heights. A typical distribution measured is shown in Fig. 5.8. The dark current of the MCP is extremely small. In the counting mode, the dark count rate with no beam in the accumulator was measured to be about 0.5Hz, negligible compared to signal rates. The working discrimination level can be anywhere above the noise level, but the best signal to noise ratio is achieved when it is set to include as most signal pulses as possible. It can be seen from Fig. 5.8 that the discrimination level setting is not very critical in our case, and is set near and above the level corresponding to the minimum in the pulse height distribution, 20mV in this case.

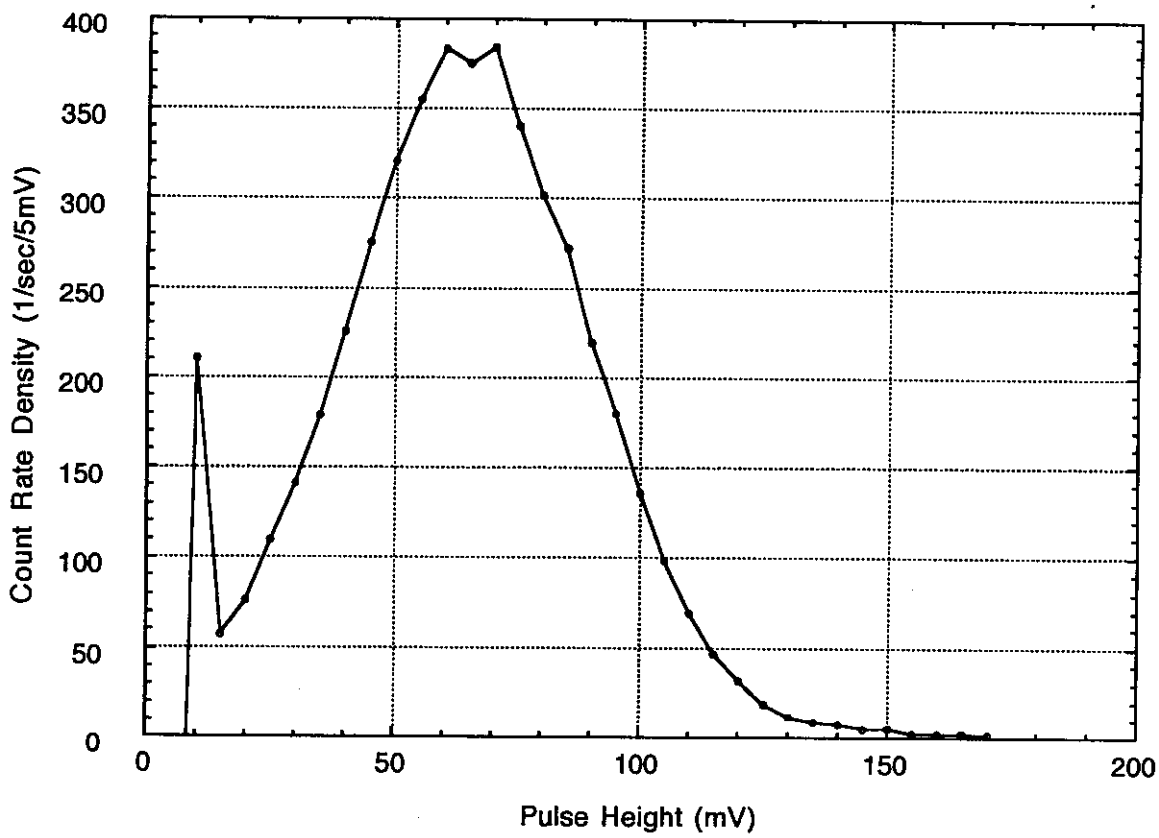

Figure 5.8: IDEA pulse height distribution with MCP HV=-2kV

The maximum counting rate that can be obtained using this configuration is limited by either the bandwidth of the pulse counting electronics, including preamplifier,

or the strip current capacity of the MCP. The MCP has a very high resistance, usually on the order of 100MΩ for one stage, and the strip current is the current normally flowing through the channel walls when the high voltage is applied. This current supplies the replenished charge in the channel wall due to secondary emissions. When the anode current is above 5–6% of the strip current, the gain of the MCP starts to saturate. In the pulse counting mode, this will affect the linearity of pulse height, but as long as the noise is small compared to pulse height and pulse height information is not needed other than height discrimination, this nonlinearity is not critical.

The three stage MCP used in this experiment has a resistance of 524MΩ, thus it has a strip current of $3.8\mu A$ with a $2KV$ voltage. Its gain at this voltage is about $1\text{–}2 \times 10^6$. 10% of the strip current corresponds to a rate of 10^6 singly-charged ions per second. This is enough to cover the event rate throughout our experiments. So, the limit in count rate in our system is determined by the amplifier bandwidth, which has to operate in the very noisy environment in the Accumulator tunnel.

The angular scan is controlled through the Fermilab ACNET control system using existing step motor control hardware and software. The photon counter is originally manually controlled and counting data is collected manually as well. Later on the control and acquisition of data from the photon counter is done through a Macintosh running a commercial software, Labview®[49], by National Instruments® using the GPIB interface.

Chapter 6

Experimental Results

Many measurements have been made with the IDEA system, for different machine and beam conditions. In this section we will present the measurement results and present a model to explain these results in parallel.

6.1 Energy distribution

The first measurements made with the IDEA were with proton beams. With proton beams, ions generated by the collision of beam particles and residual gas molecules are driven out by the electrostatic field of the beam and so they should have a mean velocity arriving at locations which are at ground potential. An example of the direct measurement of the integrated ion energy distribution is shown in Fig. 6.1. The measurements are made with both the front and the gate plate biased. The ion energy distribution from the proton beam as obtained from the derivative of the data in Fig. 6.1, is presented in Fig. 6.2. The differentiation is done after smoothing of the raw data to avoid amplifying the noise in the data. There is, however, a non-negligible difference between the two distributions measured under different bias conditions. Most significant is the difference of about 4.5eV in the peaks of the differentiated distributions. This difference has been persistent throughout all the

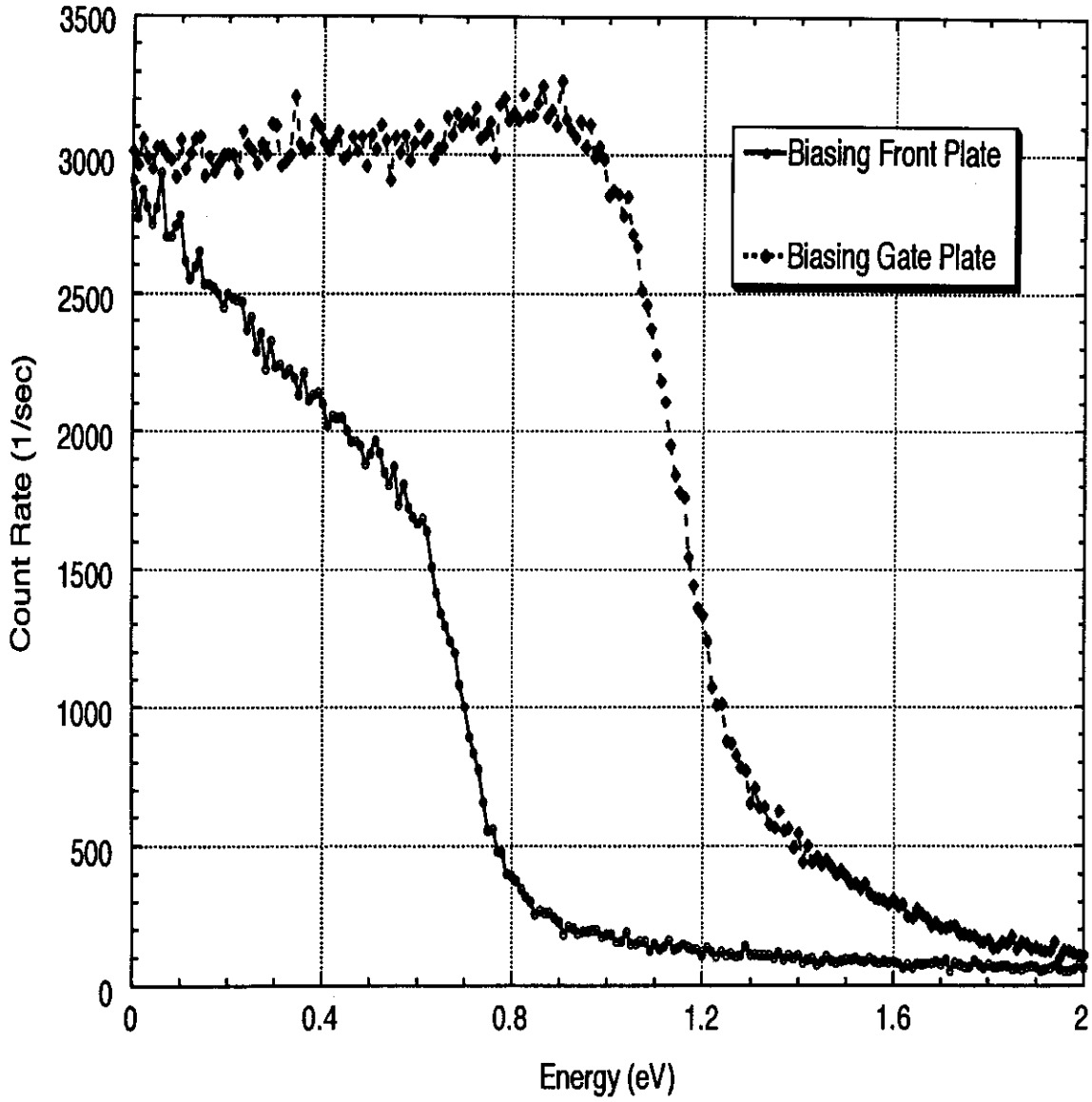

Figure 6.1: Integrated ion energy distribution from a 3.8mA proton beam

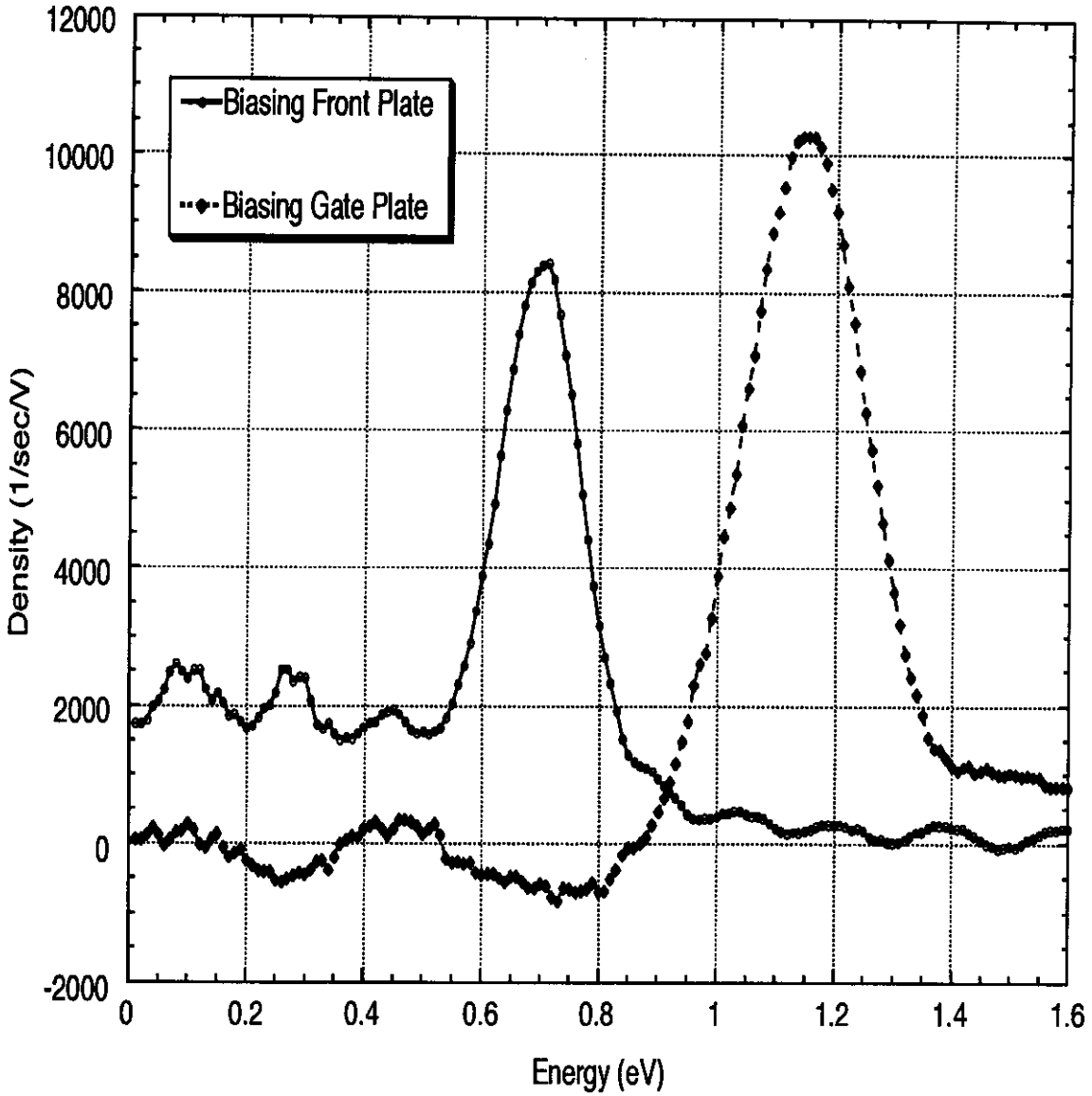

Figure 6.2: Ion energy distribution from a 3.8mA proton beam

energy scans, and the magnitude of the shift does not seem to depend on beam and machine conditions. The distortion of the shape of the distribution, other than the shift, can be partially attributed to the effect of the front plate voltage on ions before they enter the probe.

Ions in general have a wide spread in their entrance angle with respect to the probe axis. Biasing the front plate with a positive potential will repel ions with kinetic energy in the direction of the probe axis less than that potential. It will also deflect some of the ions with enough energy out of the collecting aperture of the probe. In other words putting voltage on the front plate will unavoidably introduce either focusing or defocusing effects depending on the polarity of the voltage. Therefore the energy distribution measurement made with a biased front plate will have the ion spatial distribution information embedded in it. Given the aperture of the plates and the MCP effective area within the probe, the same effect with the gate plate is expected to be much less.

The ion energy distribution for ions exiting a proton beam can be estimated by calculating the local beam potential, see section 2.3.1, and the potential well depth is proportional to the beam current. Fig. 6.3 shows this linear dependence together with the peak density energies from Fig. 6.2. Clearly the distribution measured with the front plate is closer to the estimation. Fig. 6.4 gives the calculation result for the energy distribution of ions coming out of a proton beam with a round Gaussian cross-section and compares that to the front plate energy scan measurement result. The ions are assumed to have the same transverse distribution as the beam. Reasonable agreement exists between the two.

The distortion caused by the front plate defocusing effect on the measured ion energy distribution can be estimated given the ion entrance angle distribution. Although we do not know this distribution, we can use an estimated distribution and compare the calculation with the experimental result. For the case shown in Fig. 6.5, the ions are assumed to enter the probe with a central angle of 100° and a Gaussian angular distribution with an rms spread of 25°. The original energy distribution is modeled after the calculated distribution we have just used. Both the integrated distribution and the real energy spectrum are presented.

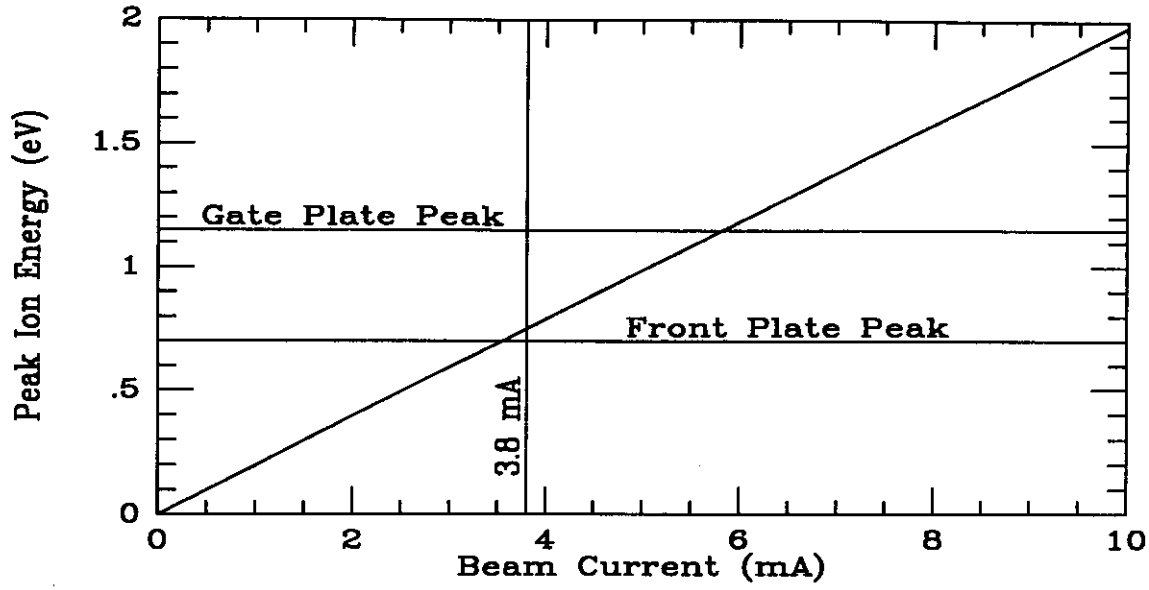

Figure 6.3: Ion Energy distribution peaks vs. beam current.

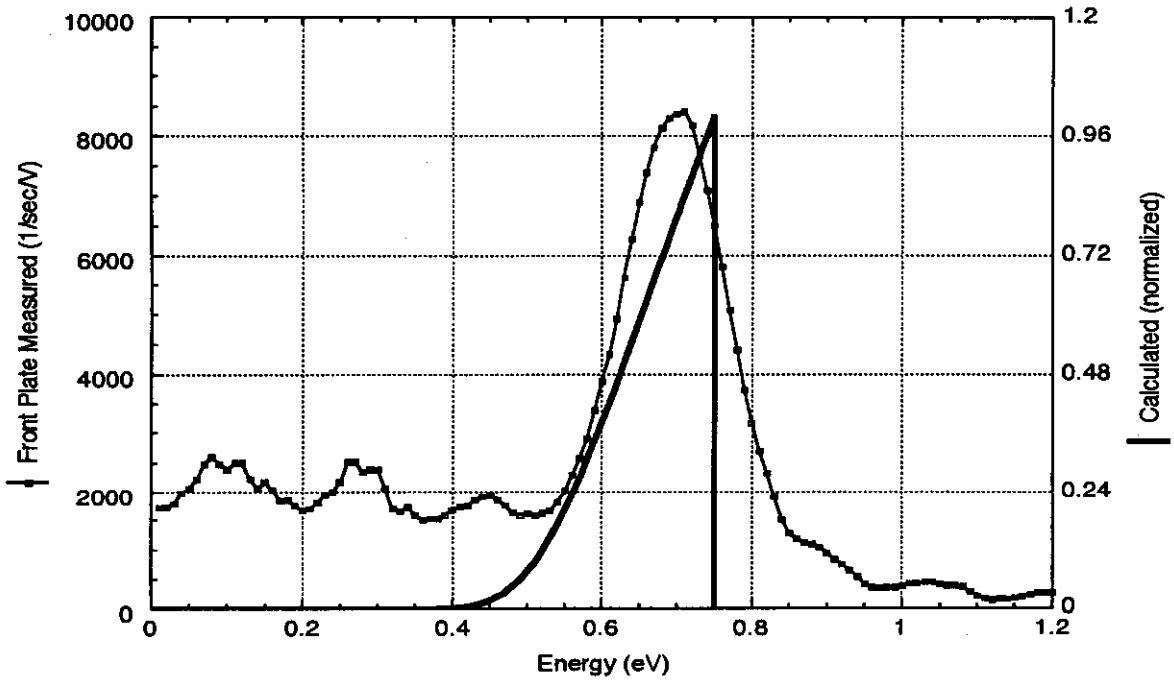

Figure 6.4: Comparison of calculated and measured ion energy distribution for a 3.8mA proton beam

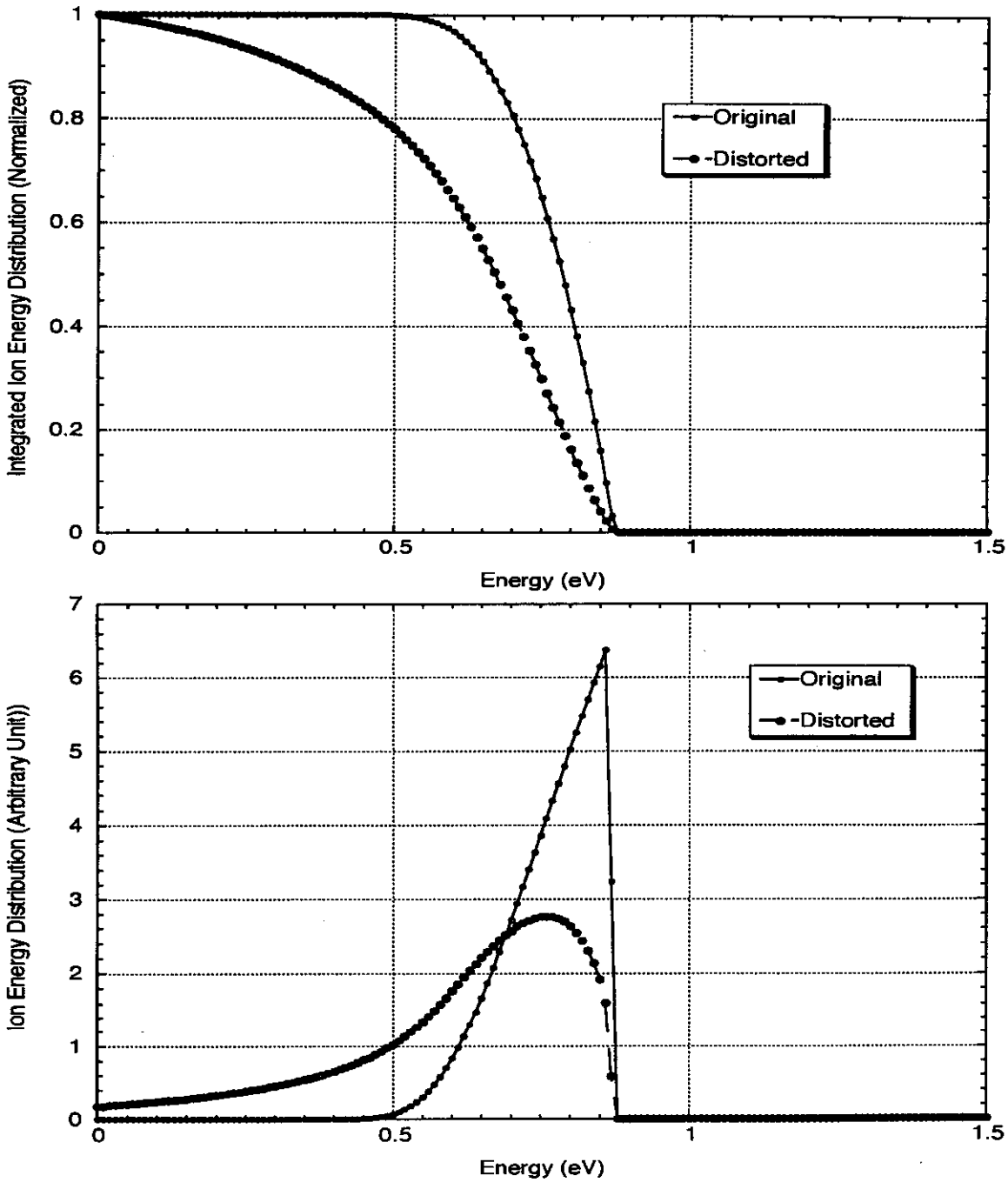

Figure 6.5: Energy distribution distortion due to the defocusing effect

The calculation above shows that there is a certain degree of distortion, but its effect on the ion energy distribution is small. We will ignore this correction from now on since a small error in the energy distribution is not crucial and it is difficult to make the correction without detailed information on the distributions. Since the front plate measurement yields reasonable agreement with the expected distribution from the calculation, we believe the measurement result with the gate plate is shifted. The reason for the shift, however, has not been understood by the author. The gate plate has been checked to have good electrical connection with the power source and is well-insulated from the front plate and ground.

For pbar beams, most ions are trapped by the potential well, so we expect escaping ions to have a Maxwellian-like energy distribution. Fig. 6.6 shows both the integrated distribution from the direct measurement and the energy distribution after differentiation. The general feature is as we have expected, however, the results show a surprisingly high temperature given the potential well depth and the scale of energy transfer in a typical Coulomb collision with beam particles.

6.2 Angular Distribution

Ion angular distributions are also measured with both proton and pbar beams. Fig. 6.7 shows an example of both for comparison.

The Accumulator runs proton beams in both circulating directions for purposes of machine study and tune up, by reversing the polarities of the magnet power supplies. Pbar beams, however, always circulate in the same direction which is defined as zero for the probe angular scan measurement, see Fig. 5.2. The angular distributions measured with the proton beam show no difference with regard to the beam direction.

The difference in the two distributions may contain some information on the longitudinal beam potential distribution, but it is complicated by the following, see Fig. 6.8. Proton beams are usually on the extraction orbit and have a different momentum from the pbar beam on core orbit. The nominal revolution frequency is $f_{0\bar{p}} = 628.955kHz$ for the pbar beam and $f_{0p} = 628.720kHz$ for the proton beam

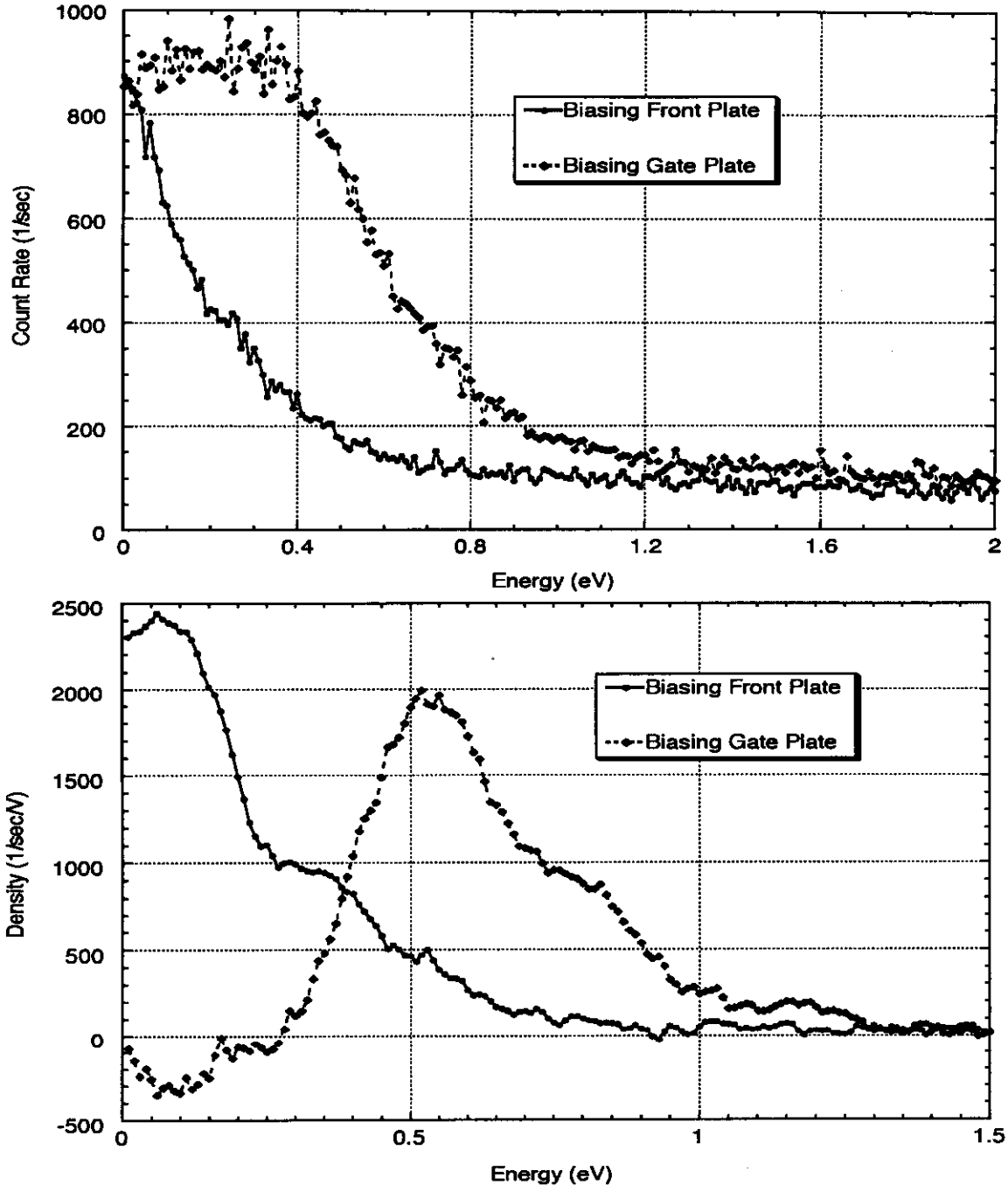

Figure 6.6: Ion energy distribution from a 20mA pbar beam. Top: Integrated distribution from direct measurement. Bottom: Distribution after differentiation.

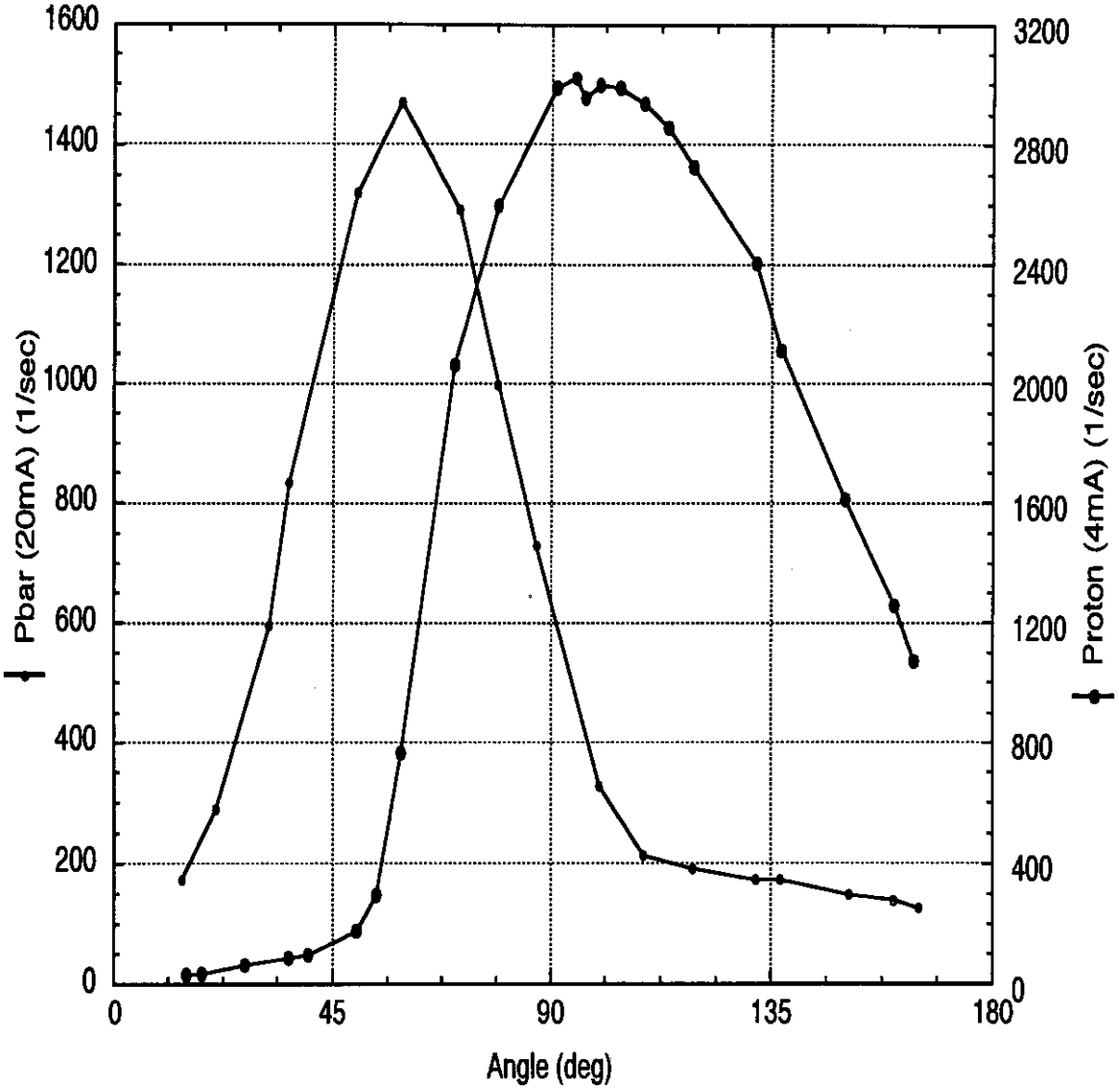

Figure 6.7: Angular distribution measured with IDEA

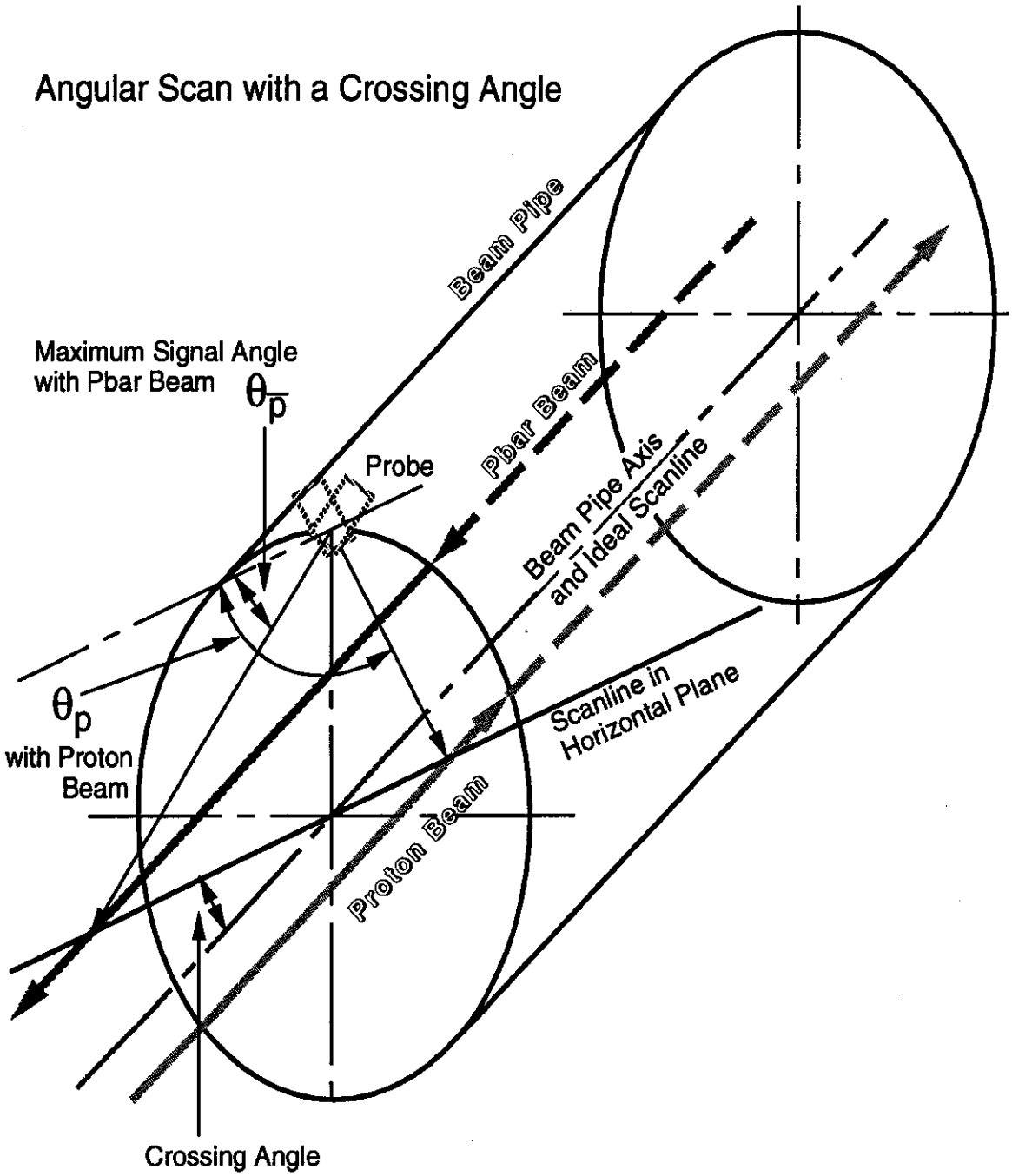

Figure 6.8: Effect of dispersion and crossing angle on angular distribution measurement

which translates into a relative momentum difference of

$$\begin{aligned} \frac{\delta p}{p} &= \frac{1}{\eta}\frac{f_{0\bar{p}} - f_{0p}}{f_{0\bar{p}}} \\ &= 1.6\% \end{aligned}$$

The dispersion at the place of the detector is $D = 1.3m$, so the difference in the horizontal position of the two closed orbits at the probe is

$$\Delta x = D\frac{\delta p}{p} = 2cm$$

Furthermore, because of probe installation errors in its rotational angle, the proton and pbar beams may have a small crossing angle with respect to the probe, which is estimated at a few degrees. The scan line of the probe in the horizontal plane, in which the proton and pbar beams are, will have the same crossing angle with the beam orbit. As a result, the angular distribution measured by the probe may be a superposition of the longitudinal scan and transverse scan across the beam. The angles where the probe directly faces the proton and pbar beams and therefore at the peak in the distribution, θ_p and $\theta_{\bar{p}}$ respectively, are different for the two beams. A 5° crossing angle will lead to a difference of about 80° between θ_p and $\theta_{\bar{p}}$. The observed difference in peak angles shown in Fig. 6.7 is about 35°. This seems to suggest that the crossing angle alone cannot explain the difference observed between the distributions with proton and pbar beams.

The same comparison has been done with pbar beams at different momenta, therefore on different orbits. In Fig. 6.9, a distribution measured with a $0.38mA$ pbar beam with revolution frequency of $628.828kHz$ is added to Fig. 6.7. The peak shift between the two pbar distributions is very close to the scenario above with a 5° crossing angle. The momentum of the $0.38mA$ pbar beam is in between that of the beams on the injection and core orbits. Therefore if the crossing angle effect is the only dominant mechanism affecting the IDEA angular distribution, the peak of the distribution for the $0.38mA$ beam should be in between those of the other two beams.

The discrepancy can be explained together with the energy distribution information presented earlier. For proton beams, ions coming out of the beam have the

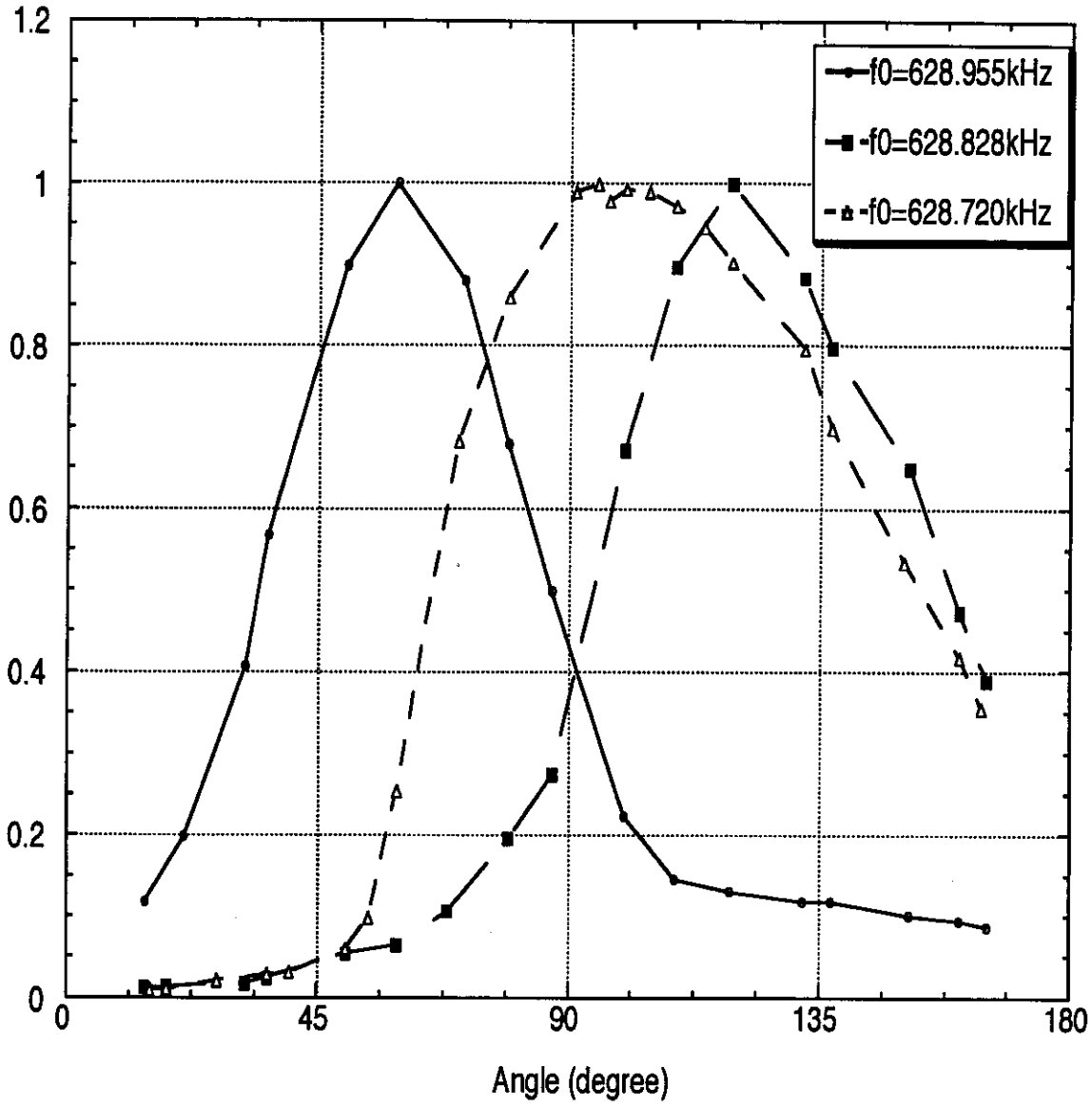

Figure 6.9: Normalized IDEA angular distributions

transverse kinetic energy of the beam potential energy. Even with a small beam current, $1.7mA$ in the case above, this potential energy is much larger than the scale of the longitudinal potential variation. The longitudinal kinetic energy due to the collision process itself is the same as that for the pbar beam case, which is on the order of $0.1eV$. Therefore ions out of the proton beam have much larger transverse kinetic energy than longitudinal energy, which means that they are concentrated in the plane perpendicular to the beam orbit, much like the electric field of the beam. When the IDEA probe angle is changed, the volume where ions can be collected stays much the same while the effective solid angle of the probe that covers this volume is varied. We thus would expect this distribution to be dominated by the solid angle effect, and as a consequence the distribution is centered around the 90° angle. Since the injection orbit is on the outer side of the probe the flat, vanishing tail is naturally on the small angle end of the distribution.

In the case with pbar beams, the situation is quite different. The transverse kinetic energies of the escaping ions are comparable with their longitudinal kinetic energy variation. Therefore their out-coming angle distribution is much broader. When the probe angle is varied it collects ions coming from different parts of the beam. The crossing angle effect will be more important here.

6.3 Coupling to Beam Coherent Oscillation

One important initial motivation of making the detector was to establish the positive link of beam coherent oscillations and emittance growths with the activity of ions. This is best illustrated when the beam becomes unstable and the coherent oscillation amplitude is large. Beam emittance undergoes explosive growth when this happens. Many cases of unstable beam and emittance blowup have been observed and recorded with the IDEA probe. In most cases observed, accompanying the emittance growth there are bursts of coherent oscillation observed on the coherent pickup. The corresponding data measured with IDEA usually shows a few short bursts of ions much higher than the normal counting rate. A few examples are shown in Fig. 6.10. As one special example shown in Fig. 6.11 the ion count rate pattern matches closely

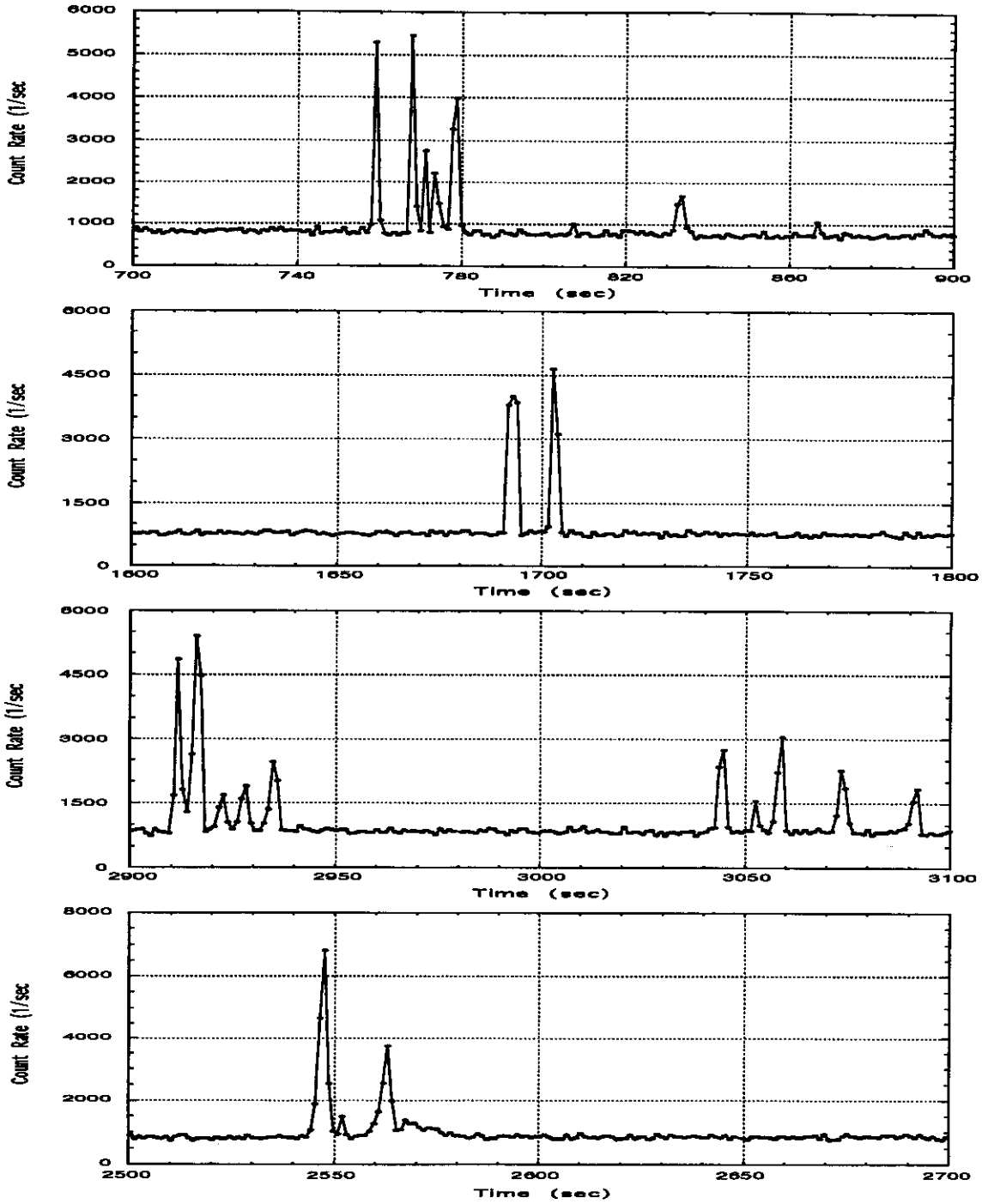

Figure 6.10: Examples of ion bursts acompanying emittance blowups

the coherent oscillation amplitude measured with the Accumulator's damper pickup. The accompanying emittance plot shows clearly that the time of emittance growth coincides well with the time of large beam coherent oscillations, and it illustrates the cause of that emittance growth.

6.4 Ion Escaping Mechanism

The time for the beam to neutralize itself, if no clearing mechanism is present, is about 2–5 seconds for the normal conditions of the Accumulator. Once an ion is created, there are many competing sources of interaction with the beam and the residual gas environment that determine the motion and final destination of the ion. The interactions with the environment include elastic and inelastic collisions, charge exchange interaction and recombinations with electrons. There are also the well known transverse oscillation and longitudinal drift under the beam electric field and the influence of the clearing electrodes. The potential well depth and therefore the ion kinetic energy in the well are on the order of $10eV$. Since residual gas is at "room" temperature, the collisions with gas molecules are mostly energy-losing interactions. The recombination with electrons removes ions so far as ion trapping is concerned. The cross section for recombination, however, is very small[50]($\sim 10^{-20}cm^2$). The residual gas molecule density at the average pressure of 5×10^{-10} is $2\times10^7/cm^3$. Even if we take the electron density as being equal to that of the residual gas molecules, the electron capture lifetime of $10eV$ ions is still on the order of 10^6sec. This makes the recombination effect negligible. The charge exchange cross-section for $10eV$ hydrogen atoms and molecules is on the order of $10^{-15}cm^2$ and the corresponding lifetime is thus a few seconds. The charge exchange process equivalently reduces the ion to thermal energies, so this is a cooling process.

The heating from that of short range Coulomb collisions presented in section 1.3.1 is obviously not enough to counter the cooling process and drive ions out of the beam at an observable rate. Observations with the IDEA probe have seen the ion count rates with pbar beams on the order of $1000/sec$ and this rate does not have a clear dependence on the beam current. To estimate the ion escaping rate in the whole

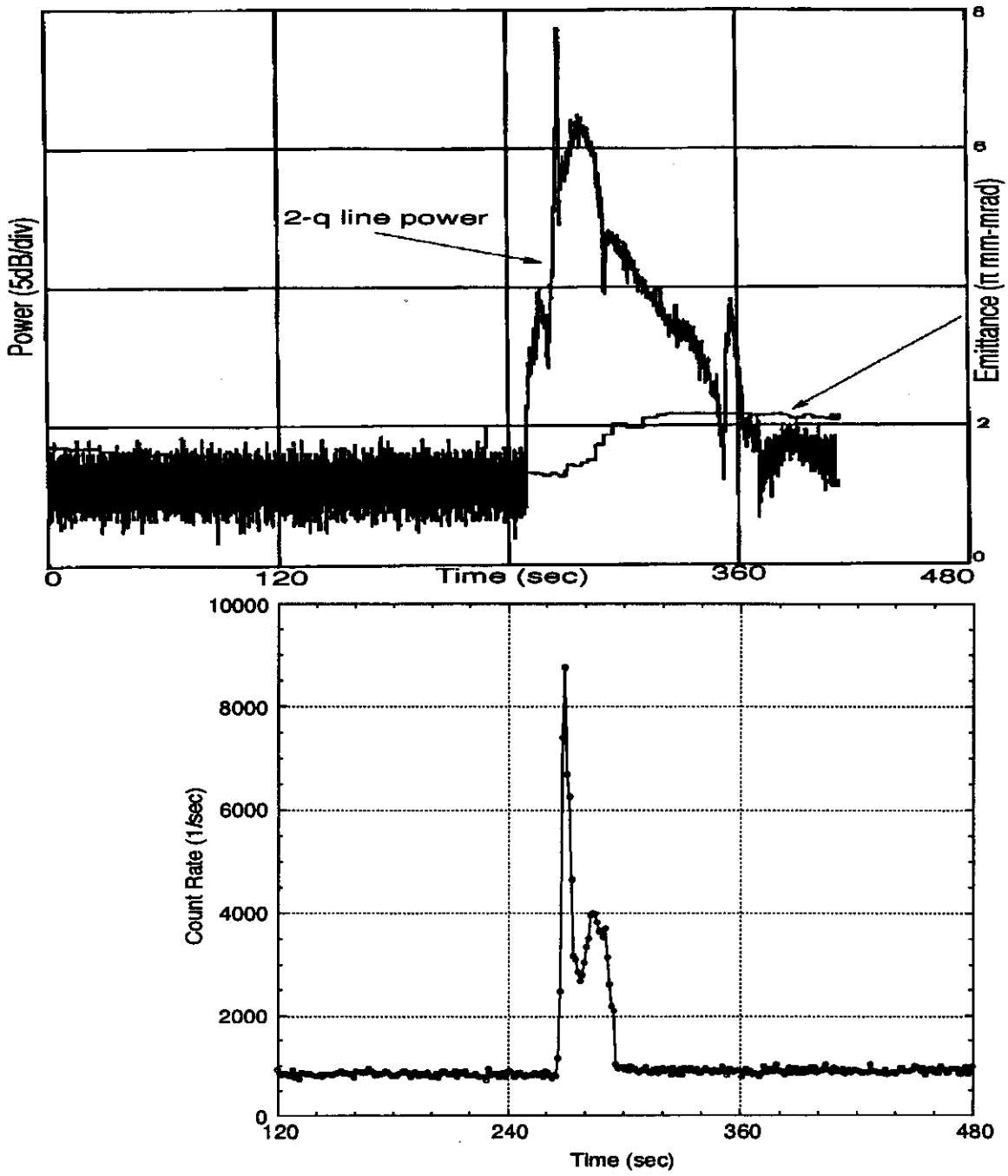

Figure 6.11: Coherent 2-q line power and ion count rate at emittance blowup

machine, let us assume uniformity around the machine. The probe face is about flush to the beam pipe wall and has a quite large accepting angle, see Fig. 5.3. To the first order, we will assume the probe collects all the ions arriving at the opening hole. Therefore the ratio of ion flux to the probe and the total escaping flux is simply the ratio of the probe opening area and the whole beam pipe wall area provided the cross-section is the same as that at the probe. The ratio thus calculated is about 10^{-7}, i.e. for every ion detected by the probe there are about 10^7 ions escaping the beam. Since the beam potential well depth in eV is about 0.1 times the beam current in mA, with $100mA$ of beam, the observed ion count rate corresponds to a total energy flow of about $100GeV/sec$. Therefore the minimum heating rate needed is about $100GeV/sec$. This represents a tiny fraction of the total kinetic energy in the beam. The corresponding lifetime of the beam energy drain is about three thousand years. Although the exact source of this heating is not understood completely, this suggests that stochastic fluctuations in the beam field because of the particle nature of the beam might be the answer. Indeed, preliminary theory has shown that the enormous number of small-angle Coulomb interactions, i.e. the Schottky noise, does present a significant heating source and will transfer energy to trapped ions constantly[51]. Since both the beam potential and the beam Schottky noise are proportional to the beam current, this might explain the fact that the observed rate of escaping ions is not a clear function of beam current. More theoretical and experimental study is needed to better understand the mechanism and some way of more efficient clearing of ions may be derived of the mechanism.

6.5 Clearing Electrodes

Clearing electrodes serve the purpose of extracting the majority of the ions created by the beam. So by turning off part or all of the clearing electrodes we can alter the potential distribution, and the ion escaping rate should reflect the local neutralization level change. Fig. 6.12 shows one such measurement. The clearing electrodes are turned off sector by sector, starting from sector 60 where our detector resides. After all electrodes are off, they are turned on sector by sector consecutively. The ion count

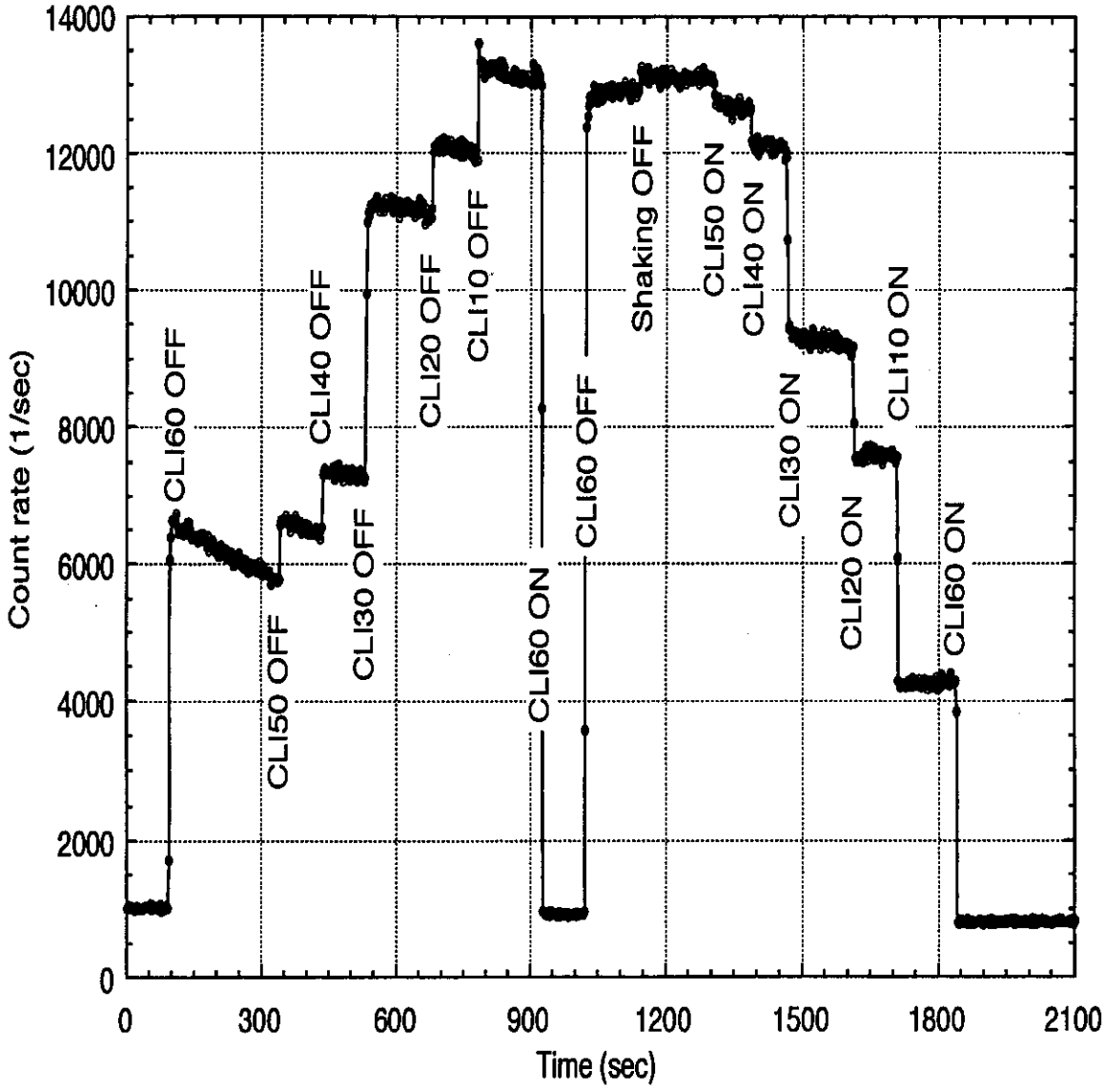

Figure 6.12: Ion count rate monitoring with clearing condition change

rate clearly tracks this change. When the clearing electrodes in sector 60 are turned off, the local neutralization increases. The beam potential well will become shallower due to the increase of the local neutralization. After a short amount of time, less than the neutralization time, the beam potential well rises to a level so that ions are moving into the adjacent sectors being cleared by the clearing electrodes there. The continuing increase in the local ion escaping rate as the clearing electrodes in non-local sectors are turned off demonstrates that ions can travel over sectors, through dipole and quadrupole magnets. Since the only longitudinal motions possible in dipole magnets are through $\vec{E} \times \vec{B}$ and $\nabla \vec{B}$ drift, more study with extra diagnostic equipment near dipole magnets would be very interesting and valuable.

Turning clearing electrodes off not only increases the escaping ion flux, it also changes the energy distribution of the escaping ions. Fig. 6.13 shows both the integrated and the true energy distribution measured by biasing the front plate with the sector 60 clearing voltage on and off. Almost all of the increased ion flux comes from ions with kinetic energy less than $0.1eV$, which suggests two different mechanisms of escape for the ions.

6.6 Bunching the Beam

In the past and present operations of the Accumulator, it has been discovered that slightly bunching the beam, $\lesssim 10\%$, improves the stability of the beam. Greater bunching of the beam will be in conflict with the operation of the stochastic cooling system. The reason for the improvement, however, is not clear. In a DC beam the equation that describes the motion of ions is

$$\frac{d^2\vec{r}}{dt^2} = F(\vec{r}) \tag{6.1}$$

If the beam is slightly bunched, the equation becomes

$$\frac{d^2\vec{r}}{dt^2} = F(\vec{r})(1 + \alpha \sin(2\omega_0 t)) \tag{6.2}$$

where we have taken into account the fact that the RF frequency is twice the revolution frequency ω_0. α is the fraction of the beam that is bunched. In the limit that

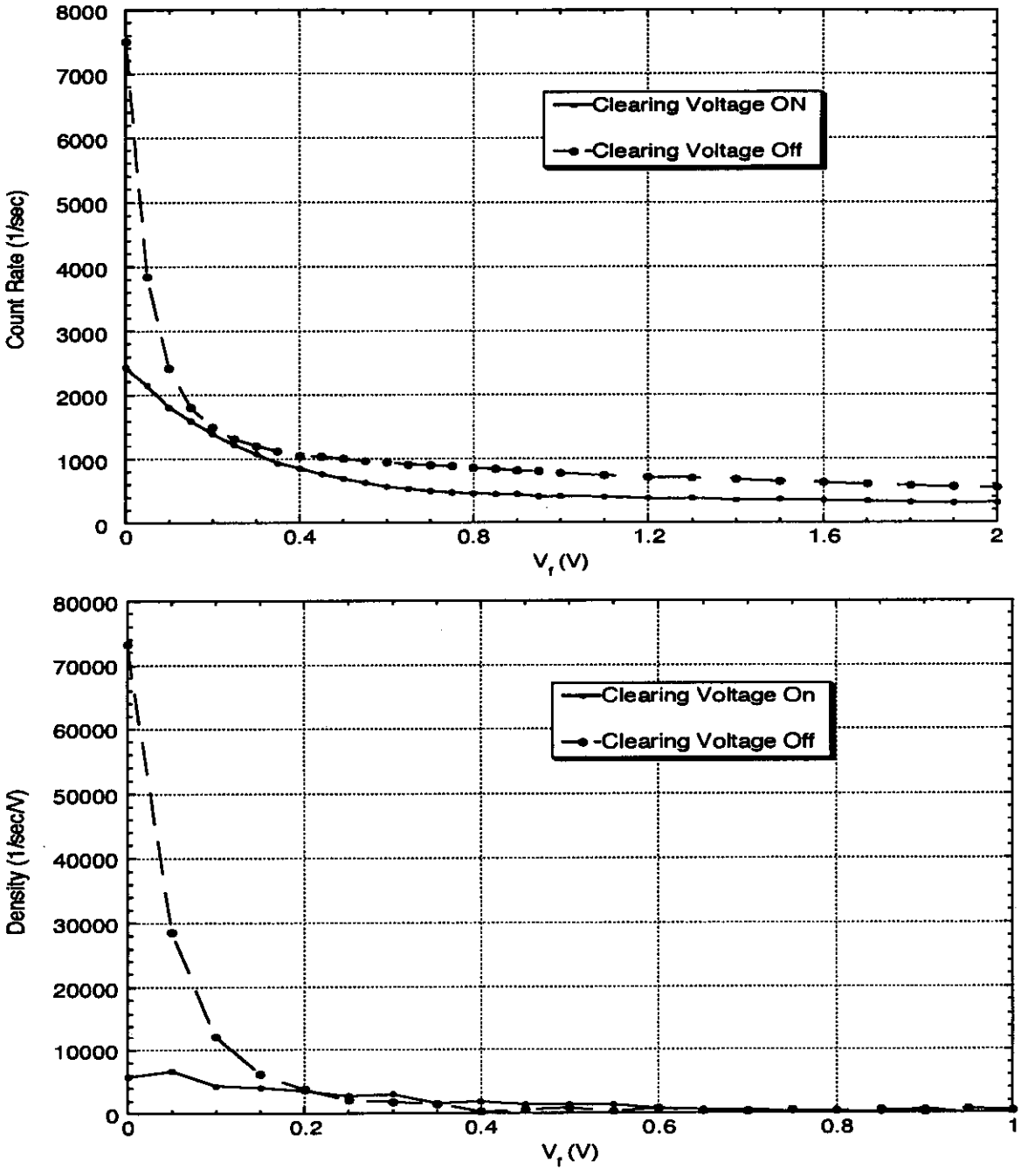

Figure 6.13: Ion energy distribution with clearing voltage on and off. Top: Integrated distribution from direct measurement. Bottom: Distribution after differentiation.

$\vec{F}(\vec{r})$ is linear, Eq. 6.2 becomes Mathieu's equation[52]. The first unstable band occurs when the ion bounce frequency is near resonance with the beam current modulation frequency. The width of this unstable band is proportional to the degree of bunching factor α and is thus very small. When non-linearity is considered, one would expect the stability of ions to improve, since after resonant ions gain energy and increase their oscillation amplitudes, the resonance condition would be lost. In addition, the ion bounce frequency is dependent on the beam current, so any satisfaction of such a resonance condition would be accidental.

To provide more direct observation and to see whether the improvement is related to improved clearing of ions, IDEA was used to monitor the ion flux with varying degrees of bunching of the beam. The result with a 22mA beam is plotted in Fig. 6.14. The measurement was made with the gate plate fixed at $0.5V$ and the front plate was scanning a few different voltages so we could get a rough energy distribution at each RF bunching voltage. There does seem to be some rapid increase of ion flux at the beginning with low RF bunching voltages. The stability of ions in partially bunched beams can be studied by computer simulation. In the case shown in Fig. 6.15, a 50mA of beam is used. Ions are assumed to have the same initial spatial distribution as the beam which is round Gaussian and then tracked to determine their stability under the varying trapping field of the partially bunched beam. The result of simulation clearly resembles that of the measurement, except for the part at very low bunching voltage. The difference in count rate is consistent with the level of the operational improvements observed in the Accumulator, and if so it is likely related to the ion escaping mechanism discussed in section 6.4.

The bunching of the beam also affects the energy distribution of the ions. It can be seen in Fig. 6.14 that the low voltage ion flux increase is really due to the increase in the flux of low energy ions. To better look at the energy distribution change, the same information in Fig. 6.14 is rearranged to give Fig. 6.16. In it the rough integrated energy scan is plotted at various bunching RF voltages. As the bunching voltage increases the fraction of the higher energy escaping ions goes up. This is to be expected because when the bunching voltages increases the gap between consecutive bunches and the maximum focusing field for the ions also increases. The increase in

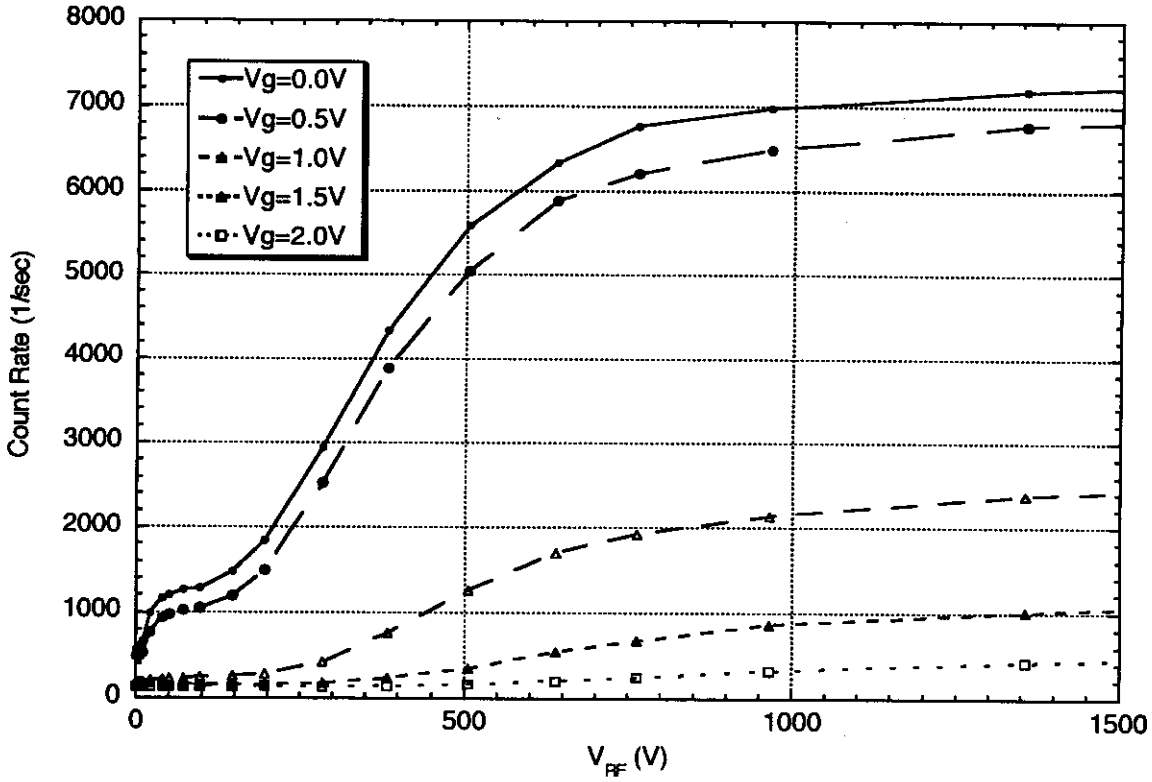

Figure 6.14: Ion count rate monitoring with increasing RF voltage

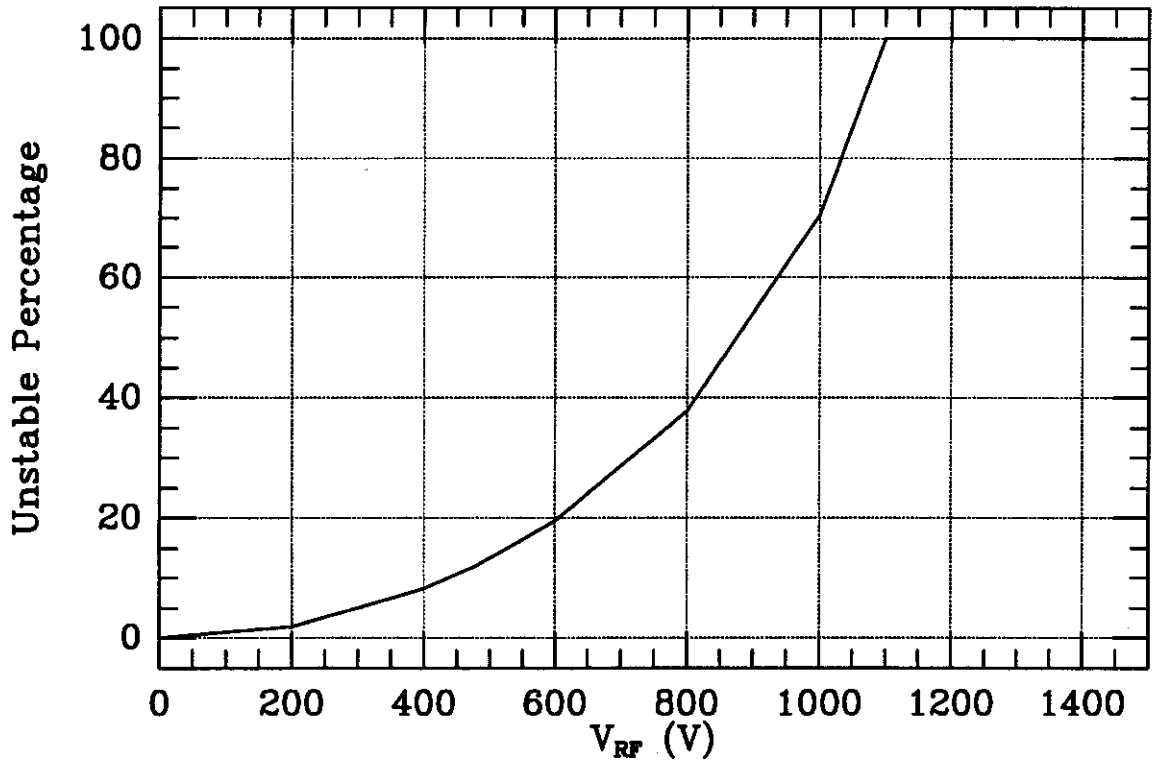

Figure 6.15: Simulation of ion stability in partially bunched beams

maximum focusing field means ions may have bigger momenta and longer gaps give ions better chances to escape. The latter is responsible for the increase in ion flux and the former is responsible for the energy spectrum extension.

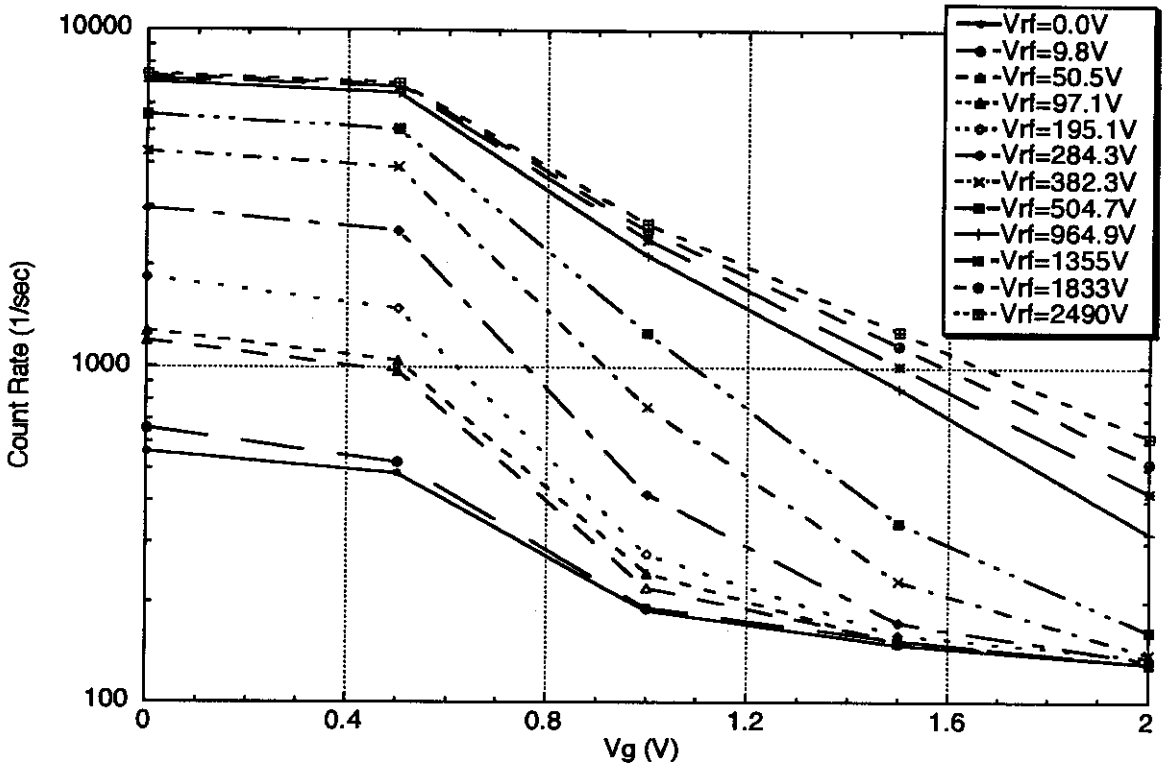

Figure 6.16: Ion energy distributions at various RF voltages

Chapter 7

Conclusions

We conclude the thesis with a summary and a few possibilities for future theoretical and experimental research projects.

The ion trapping problem has been well known in recent years for electron and antiproton machines. The work done here at the Fermilab Antiproton Accumulator in terms of beam potential and trapping field calculation showed that the old clearing electrode system was inadequate for current as well as future operations. The subsequent improvement to the machine performance with the proposed clearing electrode system upgrade based on the study proves clearly that ion trapping has been the limiting factor to beam stability for the Accumulator. The experimental measurement results of the influence of the longitudinal variations of the beam potential well on ions' longitudinal movement are in agreement qualitatively with the beam potential calculation.

A new proposal and measurement equipment are in development to take advantage of the new clearing electrode system to directly measure the ion longitudinal speed.

The coherent beam-ion instability has been studied before by many people. The theoretical treatment we presented in section 3.4 puts the effect of trapped ions in a new perspective. It is found that the effect of trapped ions can be described by a form of impedance, i.e. ion impedance, to the beam. This enables the unification of

the beam-ion instability into the normal frame of theories on beam coherent instabilities. The theory can be applied, qualitatively, to explain the observed behavior of coherent instabilities in the Accumulator. However, because of the uniqueness of ion impedance, a self-consistent theory is needed to fully describe the long time scale interaction between the beam and ions, and to quantitatively explain the experimental observations.

Calculations in Chapter 4 have shown that there will be no ion trapping problems associated with the proposed Tevatron operating scenarios with separated proton and antiproton orbits.

We have developed a direct ion detection system that is capable of measuring the ions escaping the beam potential well and their energy spectrum as well as distribution of the ions' incoming angle. The measurement results with proton beams agree quite well with theoretical estimations and shows that the system works as we expected. In section 6.2 we discussed the angular distribution measurements with both proton and antiproton beams with the IDEA system and we conclude that the observed difference in the angular distributions with the two kinds of beams are influenced by the possible installation errors, the horizontal orbit shift due to the different momenta, and the different characteristic longitudinal and transverse energies associated with the respective beam.

In section 6.3, the ion flux measurement results at times of beam coherent instability and emittance blowup were presented. It was found that ions participate in the instability growing and emittance blowup process coherently and usually several short bursts of ions occur during the blowup process. The time structure of the burst, however, can be very different.

We discussed the various ways that trapped ions interact with the residual gas environment and the beam particles in section 6.4 and their impact on the escape of ions from the beam potential well. Although the ion escape mechanism from the beam potential well is not completely understood we think it is likely to be the energy transfer from the Schottky noise of the beam. More theoretical work in needed, and is ongoing.

The ion energy spectrum out of antiproton beams, presented in section 6.1, extends

to unexpected high energy ranges ($\gtrsim 0.5eV$). The cause is not understood.

The ion flux monitoring measurement result with the IDEA probe while turning clearing electrodes in various sectors off is shown in section 6.5, and we conclude that ions do move over a long range and through dipole and quadrupole magnets.

We also did measurements with the beam partially or completely bunched. The result shows that bunching the beam destabilizes ions and it also increases the average ion energy. The general characteristics of the escaping ion flux agree with the simulation except at very low RF voltages where the measurement showed much more ions at low energies. This ion flux at low RF voltages is consistent with the improvements to beam stability, but lacks an explanation at the moment.

There are still a great deal to be learned regarding the ion trapping phenomenon. The antiproton accumulator is one of the most ideal machines to study it.

Bibliography

[1] Fermi National Accelerator Laboratory, Batavia, Illinois. *Design Report, Tevatron 1 Project*, September 1984.

[2] D.A. Edwards and M.J. Syphers. Introduction to the physics of particle accelerators. In Melvin Month and Margaret Dienes, editors, *AIP Conference Proceedings*, volume 184, pages 2–189, New York, 1989. American Institute of Physics.

[3] John David Jackson. *Classical Electrodynamics*. John Wiley & Sons, Inc., 1975.

[4] S. Chandrasekhar. *Selected Papers on Noise and Stochastic Processes*, pages 3–91. Dover Publications, Inc., 1954.

[5] Ednor M. Rowe. Synchrotron light source experiments: Bringing Alladin on line. *Nuclear Instruments and Methods*, B24/25:414, 1987.

[6] G. Carron, *et al.* Observation of transverse quadrupole mode instabilities in intense cooled antiproton beams in the AA. In *Proceedings of the 1989 IEEE Particle Accelerator Conference*, page 803, Chicago, March 1989.

[7] A. Poncet. Ion trapping and clearing. In *CERN Accelerator School – Third advanced accelerator physics course*, pages 74–98, Uppsala University, Sweden, September 1989. CERN.

[8] P. Zhou and J.B. Rosenzweig. Ion trapping in tevatron with separated orbits. In *Proceeding of the Fermilab III Instability Workshop*. Fermilab, 1990.

[9] Yuri Orlov. The suppression of transverse instabilities in the CERN AA by shaking the $\bar{p}$ beam. Internal Publication CERN PS/89-01(AR), CERN, 1989.

[10] A. Alves-Pires and R. Dilão. Elimination of transverse beam instabilities in accumulation rings by application of an external periodic force. *Physical Review A*, 45(4):2567–2571, 15 Februray 1992.

[11] J. Marriner and A. Poncet. Neutralisation experiments with proton and antiproton stacks – ion shaking. Pbar Note 481, Fermilab, March 1989.

[12] John Marriner, *et al.* Experiments and practise in beam shaking. *Particle Accelerators*, 30:13–20, 1990.

[13] A. Dainell and M. Pusterla. An analytic simulation of the ion-antiproton instability in the cern antiproton accumulator. *Particle Accelerators*, 23:151–165, 1988.

[14] C.J. Bocchetta and A. Wrulich. The trapping and clearing of ions in Elettra. Internal Publication ST/M-88/26, Sincrotrone Trieste, November 1988.

[15] R. Alves Pires, *et al.* On the theory of coherent instabilities due to coupling between a dense cooled beam and charged particles from the residual gas. In *Proceedings of the 1989 Particle Accelerator Conference*, pages 800–802, Chicago, IL, March 1989.

[16] Y. Baconnier and G.B. Brianti. The stability of ions in bunched beam machines. Internal Publication CERN/SPS/80-2(DI), CERN, 1980.

[17] Yuri Orlov. The suppression of transverse instabilities caused by trapped ions in the AA by shaking of $\overline{P}$ beam. Internal Publication CERN/PS/89-01, CERN, Genever, Switzerland, 1989.

[18] Yoshio Gomei, Koichi Nakayama, Kimichika Fukushima and Satoru Sukenobu. Ion trapping in a superconducting circular electron storage ring. *Nuclear Instruments and Methods in Physics Research*, A278:389–393, 1989.

[19] D. Möhl. Stochastic cooling. In *CERN Accelerator School – Advanced Accelerator Physics*, volume II, pages 453–533, The Queen's College, Oxford, England, September 1985. CERN.

[20] Foster F. Rieke and William Prepejchal. Ionization cross sections of gaseous atoms and molecules for high-energy electrons and positrons. *Physical Review A*, 6(4):1507, October 1972.

[21] Mitio Inokuti. Inelastic collisions of fast charged particles with atoms and molecules – the bethe theory revisited. *Review of Modern Physics*, 43(3):297–347, July 1971.

[22] Robert D. Oberholtzer. Private communication.

[23] Rui Alves-Pires. Private communication.

[24] A. Poncet. Some consideration in connection with ion trapping in the accumulator. Pbar Note 309, Fermilab, June 1983.

[25] John Marriner. Ion trapping in the accumulator. Pbar Note 425, Fermilab, February 1985.

[26] M. Bassetti and G. Erskine. Internal Publication CERN-ISR-TH/80-06, CERN, 1980.

[27] Steven J. Werkema, David W. Peterson, and Ping Zhou. Transverse emittance growth in the fermilab antiproton accumulator with high-current antiproton stacks. In *Proceedings of the 1993 IEEE Particle Accelerator Conference*, Washington, D.C., March 1993.

[28] D. Boussard. Schottky noise and beam trasnfer function diagnostics. In *CERN Accelerator School – Advanced Accelerator Physics*, volume II, pages 416–452, The Queen's College, Oxford, England, September 1985. CERN.

[29] D. W. Peterson. Scottky signal monitoring at fermilab. In Elliott S. McCrory, editor, *Conference Proceedings No. 229, Accelerator Instrumentation*, Particles

and Fields Series 44, pages 108–130, New York, October 1990. American Institute of Physics.

[30] J. Petter, J. Marriner, J. McCarthy. Transverse beam dampers for the fnal antiproton rings. In *Proceedings of the 1987 IEEE Particle Accelerator Conference*, 1987.

[31] A.W. Chao. Coherent instabilities of a relativistic bunched beam. Internal Publication SLAC-PUB-2946, SLAC, June 1982.

[32] W.K.H. Panofsky and W.A. Wenzel. *Rev. Sci. Inst.*, 27:967, 1956.

[33] Dieter Möhl and Andrew M. Sessler. The use of rf-knockout for determination of the characteristics of the transverse coherent instability of an intense beam. Internal Publication LBL-42 ERAN-161, LBL, August 1971.

[34] B. Zotter A. Hofman. Measurement of beam stability and coupling impedance by rf excitation. *IEEE Transactions on Nuclear Science*, NS-24(3):1487–1489, June 1977.

[35] H. Hahn and F. Pedersen. On coaxial wire measurements of the longitudinal coupling impedance. Internal Publication BNL 50870, Brookhaven National Laboratory, April 1978.

[36] G. Nassibian and F. Sacherer. Methods for measuring transverse coupling impedances in circular accelerators. *Nuclear Instruments and Methods*, 157:21–27, 1979.

[37] Emanuel Karantzoulis. An overview on impedance and impedance measuring methods for accelerators. Internal Publication ST/M-91/1, Sincrotrone Trieste, January 91.

[38] F. Caspers. Bench methods for beam coupling impedance measurements. Internal Publication CERN/PS 91-36 (AR), CERN, 1991.

[39] Francis F. Chen. *Introduction to Plasma Physics.* Plenum Press, New York, 1977.

[40] H. G. Hereward. Landau damping by non-linearity. Internal Publication CERN/MPS/DL 69-11, CERN, July 1969.

[41] Eugene Butkov. *Mathematical Physics.* Addison-Wesley, 1968.

[42] J. Marriner, *et al.* Stability criterion and wall impedance for the antiproton accumulator. Pbar Note 422, Fermilab, 1985.

[43] H.G. Hereward. The elementary theory of landau damping. Internal Publication CERN 65-20, CERN, 1965.

[44] A. Poncet and Y. Orlov. EPA machine experiment note - ion shaking tests. Technical Report PS/ML/Note 89-1, CERN, 1989.

[45] P. Zhou and J.B. Rosenzweig. Ion clearing by cyclotron resonance shaking. In *Proceedings of the 1991 IEEE Particle Accelerator Conference*, page 1776, 1991.

[46] W. Marsh. Ion trapping. In E. Malamud and G. Dugan, editors, *Physics at Fermilab in the 1990's – Collected Reports of the Accelerator and Beam Line Working Groups.* Fermilab, 1990.

[47] A.D. Russell. Assignment of separator locations. Internal note, Fermilab, July 1989.

[48] Hamamatsu Corporation. *Technical Information: MCP Assembly*, September 1991.

[49] Labview® is a commercial product and a trademark of National Instruments Corporation.

[50] H.S.W. Massey, E.H.S. Burhop and H.B. Gilbody. *Electronic and Ionic Impact Phenomena*, volume II. Oxford, second edition, 1969.

[51] S.Y. Hsueh. Study of stochastic parametric resonance with application to ions trapped in a particle beam. Internal Publication FERMILAB-Pub-93/115, Fermilab, 1993.

[52] Milton Abramowitz and Irene A. Stegun, editors. ***Handbook of Mathematical Functions.*** Dover Publications, Inc., New York, 1973.

[53] Rui Alves-Pires. Conformal mapping for two dimensional electrostatic beam potential calculations. Internal Publication CERN PS/87-66 (AA), CERN, 1987.

[54] Zeev Nahari. ***Conformal Mapping.*** Dover Publication, New York, 1975.

Appendix A

Calculation of Beam Potential

A.1 Electrostatic Potential of Bi-Gaussian Beams

First we briefly summarize the theory presented in [53]. The approach is based on conformal mapping and with the assumption that an analytical expression for the charge distribution in free space is known, which is true for many distributions, including bi-Gaussian. Suppose the charge distribution $\rho(z)$ generates a free space potential $\Phi(z)$ i.e.

$$\Delta_z \Phi = -\frac{1}{\epsilon_0}\rho(z) \tag{A.1}$$

Mapping the region inside the vacuum pipe (on z-plane) to the the upper half of w-plane by $w = f(z)$ the Poisson equation becomes

$$\Delta_w \Psi = -\frac{1}{\epsilon_0}\sigma(w)|\frac{dg}{dw}(w)|^2 \tag{A.2}$$

where $\Psi(w) = \Phi(g(w))$, $\sigma(w) = \rho(g(w))$ and $g(w) = f^{-1}(w)$. The effect of the boundary can be included by introducing an additional term:

$$\Delta_w \Psi = -\frac{1}{\epsilon_0}\{\sigma(w)|\frac{dg}{dw}(w)|^2 - \sigma(\bar{w})|\frac{dg}{dw}(\bar{w})|^2\} \tag{A.3}$$

If the potential due to the first term is $\Psi_f(w)$ then the potential due to the second term will be $\Psi_i(w) = -\Psi_f(\bar{w})$. The total potential, satisfying both the equation and

the boundary condition, after transformation back to the original plane is then

$$\Phi(z) = \Phi_f(z) - \Phi_f(z_i) \tag{A.4}$$

where $z_i = g(\bar{w})$ denotes the image of z. In other words, the potential at the point z is equal to the free space potential at z minus the free space potential at the image of z, z_1.

The above conclusion is not true in general, however. The potential is guaranteed to satisfy the boundary condition, since on the boundary $z = z_i$, but in general does not satisfy the Poisson equation. To support this claim, we consider the same problem and write down the free space potential on the original z-plane.

$$\Phi_f(z_p) = \int G_z(z_p - z)\rho(z)dx\,dy \tag{A.5}$$

where $G_z(z_p - z)$ is the potential at point z_p due to the unit charge at point z, i.e. the Green's function on the z-plane. On the w-plane Eq. A.6 becomes

$$\Psi(w_p) = \int G_w(w_p, w)\rho(g(w))|g'(w)|^2 du\,dv \tag{A.6}$$

where $G_w(w_p, w) = G_z(g(w_p) - g(w))$ is the direct mapping of the Green's function on the z-plane and for conformal mapping $dxdy = |g'(w)|^2 dudv$. We have not used the normal Green's function on the w-plane because we want to get the known free space potential on z-plane after we map the complete potential back to z-plane. The difference is of course a solution to Laplace equation, but without boundary conditions it is in general non-trivial. In this way, while $G_w(w_p, w) = G_w(w, w_p)$ is always true, $G_w(w_p, w)$ in general cannot be written in the form of $F(|w_p - w|)$, where F is some other function.

The complete potential which includes the contribution from the image charge distribution is therefore

$$\Psi(w_p) = \int G_w(w_p, w)\rho(g(w))|g'(w)|^2 du\,dv - \int G_w(w_p, \bar{w})\rho(g(w))|g'(w)|^2 du\,dv \tag{A.7}$$

and on $z - plane$

$$\Phi(z_p) = \Phi_f(z_p) - \int G_z(z_p - z_i)\rho(z)dx\,dy. \tag{A.8}$$

When $G_w(w_p, \bar{w}) = G_w(\bar{w}_p, w)$, which implies $|g'(w)| = |g'(\bar{w})|$, we can reach the conclusion in ref. [53], i.e. $\Phi(z) = \Phi_f(z) - \Phi_f(z_i)$. The condition $|g'(w)| = |g'(\bar{w})|$ means at point z and its image point z_i the local metrics are the same, so the charge distributions are not distorted. This condition is rather strict and most transformations do not satisfy it, and as a result it greatly limits the application of this approach. Of the geometries concerned here, only the rectangular case falls completely into this category. In this case the transformation function involves the Jacobian elliptical function $sn(z)$[54]. It can be shown $|g'(w)| = |cn(w)dn(w)| = |g'(\bar{w})|$ is indeed satisfied and the final result is that the total potential is from the contribution of a series of infinite number of image charge distributions reflected with respect to the four boundaries[53].

Another hidden problem with this approach is the pole of the transformation function g. For a point charge in the z-plane $\rho(z) = \delta(z - z_0)$, it is also a point charge at $g^{-1}(z)$ since

$$\delta(g(w) - g(w_0))|g'(w)|^2 = \delta(w - w_0)|g'(w_0)|^{-2}|g'(w)|^2 \tag{A.9}$$

but if w_0 is not a regular point of function g an unexpected effect can occur. The pole of g corresponds to infinity on the z-plane and therefore any charge at that point disappears on z-plane. An example is the case of a circular boundary which was discussed later in the paper. The transformation function is

$$g(w) = k\frac{w - a}{w - \bar{a}} \tag{A.10}$$

where $|k| = R$, the radius, $w = a$ corresponds to the origin on the z-plane and its image $w = \bar{a}$ the infinity. Transforming the potential on z-plane $\Phi = \log(z - z_0)$ introduces another charge on the w-plane

$$\Psi(w) = \log(\frac{w - w_0}{w - \bar{a}}) + \log(k\frac{a - \bar{a}}{w_0 - \bar{a}}). \tag{A.11}$$

Notice that this Green's function on w-plane satisfies the following relation:

$$G_w(w, \bar{w_0}) = G_w(\bar{w}, w_0) + G_z(z, 0) + const. \tag{A.12}$$

which means we can apply the potential superposition provided that we compensate for the extra term. The physical picture of this is quite clear. The transformation

onto the w-plane brings the hidden charge originally at infinity into clear existence. Undoing the transformation of the image therefore will unavoidably introduce an equal amount of charge at the origin. The integration over the whole charge distribution will lead to an extra point charge, which equals the total charge contained in the distribution, at the origin. We then can conclude that the total potential generated by a bi-Gaussian distribution inside a circular conducting boundary is

$$\Phi(z) = \Phi_f(z) - \Phi_f(z_i) + \log(\frac{|z|^2}{R^2}). \tag{A.13}$$

Which agrees completely with a direct calculation (see A.2).

For general situations, the direct calculation will be needed. However, if the original charge distribution is symmetric, then outside the distribution the potential behaves just like a point charge. From equation A.8 above, with $\rho z = \delta z - z_0$, the total potential is then

$$\Phi(z) = \Phi_f(z - z_0) - \Phi_f(z - z_i) \tag{A.14}$$

to within a constant, which is the potential on the boundary. Where z_i is the image point of z_0 and this is true for any boundary geometry. In practice, as long as the beam size is small compared to its distance to the nearest boundary point, we expect the deviation from the above due to the asymmetry of the distribution to be small. This is especially useful in our particular application where the beam is close to round and the beam size is relatively small compared to the vacuum pipe size. To avoid intensive numerical calculation of the integrals and summations, this approximated approach is used in cases like elliptical boundaries where analytical expressions are not found. Calculation done for the elliptical boundary case shows that with the beam center being more than 5 times the rms beam size away from the wall the error introduced to the potential at near the beam center by such approximation is less or about one percent.

A.2 Direct Calculation in Circular Boundaries

The electrostatic potential of a bi-Gaussian beam in circular boundaries can be calculated by direct integration.

The potential at (x_p, y_p) due to a unit line charge at (x_0, y_0) inside a circular boundary of radius R is

$$\phi = -\ln \frac{(x_p - x_0)^2 + (y_p - y_0)^2}{(x_p - x_0\frac{R^2}{r_0^2})^2 + (y_p - y_0\frac{R^2}{r_0^2})^2} \frac{R}{r_0} \tag{A.15}$$

where $r_0 = \sqrt{x_0^2 + y_0^2}$. Consider now a charged beam with the transverse distribution

$$\lambda(x,y) = \frac{1}{4\pi\epsilon_0} \frac{\lambda_0}{2\pi\sigma_x\sigma_y} e^{-\frac{(x-x_0)^2}{2\sigma_x^2} - \frac{(y-x_0)^2}{2\sigma_y^2}} \tag{A.16}$$

where σ_x and σ_y are beam's rms horizontal and vertical size respectively, and λ_0 is the total charge per unit length. Its potential at point (x_p, y_p) is then

$$\Phi(x_p, y_p) = -\alpha \int \ln \frac{R^2 r^2 [(x_p - x)^2 + (y_p - y)^2]}{(x_p r^2 - x R^2)^2 + (y_p r^2 - y R^2)^2} e^{-\frac{(x-x_0)^2}{2\sigma_x^2} - \frac{(y-x_0)^2}{2\sigma_y}} dx\, dy \tag{A.17}$$

$$= -\alpha \int_0^\infty \rho e^{-\frac{\rho^2}{2}} d\rho \int_0^{2\pi} d\theta \cdot \tag{A.18}$$

$$\ln \frac{R^2[(x_p - x_0 - \rho\sigma_x\cos\theta)^2 + (y_p - y_0 - \rho\sigma_y\sin\theta)^2]}{r_p^2 r^2 + R^4 - 2[x_p(x_0 + \rho\sigma_x\cos\theta) + y_p(y_0 + \rho\sigma_y\sin\theta)]R^2} \tag{A.19}$$

where $\alpha = \frac{1}{4\pi\epsilon_0}\frac{\lambda_0}{2\pi\sigma_x\sigma_y}$, $r = \sqrt{x^2 + y^2}$ and

$$x - x_0 = \rho\sigma_x\cos\theta \tag{A.20}$$

$$y - y_0 = \rho\sigma_y\sin\theta \tag{A.21}$$

For our particular application, we are only interested in the potential at the beam center and beam center only has displacement in the horizontal direction, thus we have $x_p = x_0, y_p = y_0$ and $y_0 = 0$. The last equation above reduces to

$$\Phi_0 = -\alpha \int_0^\infty \rho e^{-\frac{\rho^2}{2}} d\rho \int_0^{2\pi} d\theta \cdot \ln \frac{\frac{1}{2}R^2\rho^2[(\sigma_x^2 + \sigma_y^2) + (\sigma_x^2 - \sigma_y^2)\cos(2\theta)]}{x_0^2(\sigma_x^2 - \sigma_y^2) - 2x_0\delta^2\rho\sigma_x\cos\theta + \delta^4 + x_0^2\sigma_y^2\rho^2} \tag{A.22}$$

where $\delta = \sqrt{R^2 - x_0^2}$. The integration over θ can be carried out and leads to

$$\Phi_0 = -\frac{\lambda_0}{8\pi\epsilon_0} \int_0^T \ln \frac{R^2(\sigma_x + \sigma_y)^2 t}{[\delta^2 + \sqrt{\delta^4 - x_0^2(\sigma_x^2 - \sigma_y^2)t}]^2} e^{-\frac{t}{2}} dt \tag{A.23}$$

where a finite upper integration limit T is introduced, which has to be large enough to include the whole beam. Theoretically T cannot really be infinity because it makes

no sense to integrate outside the boundary, but practically it makes no difference because the whole beam is always inside the boundary. Therefore we can make a convenient choice to suit our needs in the actual numerical calculation e.g.

$$T = \frac{\delta^4}{x_0^2(\sigma_x^2 - \sigma_y^2)} \tag{A.24}$$

in the case of $\sigma_x > \sigma_y$. With the substitution of

$$s = 1 - \sqrt{1 - x_0^2(\sigma_x^2 - \sigma_y^2)t/d^4} \tag{A.25}$$

we get finally

$$\Phi_0 = \frac{\lambda_0}{4\pi\epsilon_0}\{\gamma + \ln\frac{2(R^2 - x_0^2)^2}{R^2(\sigma_x + \sigma_y)^2} - 2\int_0^{\mp 1} e^{-\frac{(R^2-x_0^2)^2}{2x_0^2(\sigma_x^2-\sigma_y^2)}s(2-s)}\frac{ds}{2-s}\} \tag{A.26}$$

where $\gamma \approx 0.577$ is the Euler constant and the minus sign is for the case of $\sigma_x < \sigma_y$. The last term in the equation above vanishes when the beam is at the center of the boundary ($x_0 = 0$) or the beam is round ($\sigma_x = \sigma_y$).

Vita

Ping Zhou, born on July 2, 1961 in Quanjiao County, Anhui Province of China, is the elder of the two sons in the family. His father, Sijun Zhou, and his mother Guoyan Li are both school teachers. Ping was shielded from much of the turmoil of the infamous "Great Proletarian Cultural Revolution" and taught the importance of education and discipline by his parents.

Growing up during the Cultural Revolution, he was very fortunate to be able to graduate a year earlier and accepted into the Department of Modern Physics at the University of Science and Technology of China in Hefei, Anhui in 1978. He graduated with a Bachelor of Science degree in Physics one year in advance in 1982. He continued his graduate study in accelerator physics in the same department and the National Synchrotron Radiation Laboratory at the university. The days at the university have not only given him the academic training, but also helped shaping his personality. After getting the degree of Master of Science in accelerator physics, he stayed at the laboratory as a scientist for a few months.

He married his wife Jianmei Zheng shortly before coming to Northwestern University at Evanston, IL to pursue his PhD study. He was joined by his wife at Fermilab after he finished the two years of course study and joined the accelerator physics PhD program of Fermilab. He will start his postdoctoral work in the RHIC project at the Brookhaven National Laboratory at Long Island, New York in the August of 1993.